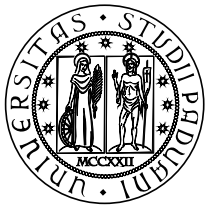

UNIVERSITÀ
DEGLI STUDI
DI PADOVA

DIPARTIMENTO DI METODI E MODELLI MATEMATICI
PER LE SCIENZE APPLICATE

SCUOLA DI DOTTORATO DI RICERCA IN SCIENZE
DELL'INGEGNERIA CIVILE E AMBIENTALE - CICLO XXII
Sede Amministrativa: Università degli Studi di Padova

THERMOPOROELASTIC MODELLING OF DEEP AQUIFER INJECTION AND PUMPING BY MIXED FINITE ELEMENTS AND FINITE VOLUMES

Direttore della Scuola: Ch.mo Prof. Stefano Lanzoni
Supervisore: Ch.mo Prof. Giuseppe Gambolati
Correlatore: Dott. Ing. Massimiliano Ferronato

Dottorando: Nicola Castelletto

Gennaio 2010

Ai miei genitori

Summary

The present work concerns the mechanics of porous media and focuses on the development of a thermo-poro-elastic model, with particular emphasis on the simulation of fluid injection/pumping operations into geological formations. A non-linear model for coupled fluid flow and heat transfer in saturated porous media has been developed based on Mixed Hybrid Finite Elements (MHFEs) and Finite Volumes (FV). In particular, the MHFE discretization for the flow equation leads to an element-wise mass-conservative scheme, providing an accurate discrete velocity field. In the heat transfer equation, a time-splitting tecnique has been used solving separately the convective term by means of a FV scheme, and the conductive term by the MHFE method. The model can simulate problems characterized by very sharp temperature fronts, introducing no spurious oscillation in the numerical solution and negligible numerical diffusion, and does not required an excessive mesh resolution in order to ensure accuracy and stability. A fully coupled 3-D Mixed Finite Element model has also been developed for the numerical solution to the Biot equations of 3-D consolidation, combining Mixed Finite Elements (MFEs) and traditional Finite Elements (FEs) to discretize the fluid flow and the structural equilibrium equations, respectively. MFEs are used in order to alleviate the pore pressure numerical oscillations at the interface between materials with different permeabilities. An ad hoc solution algorithm based on conjugate gradients is implemented that takes advantage of the block structure of the discretized problem. The proposed models have been validated against well-known analytical solutions, and successfully experimented with in engineering applications.

Sommario

Il presente lavoro di tesi si inserisce nell'ambito dello studio della meccanica dei mezzi porosi ed ha avuto come oggetto principale lo sviluppo di un modello termo-poro-elastico per la simulazione di processi di iniezione/pompaggio in formazioni geologiche. E' stato implementato un modello non-lineare per lo studio del flusso di massa accoppiato al trasferimento di calore utilizzando Elementi Finiti Misti Ibridi (MHFE) e Volumi Finiti (FV). In particolare, nel caso dell'equazione di flusso del fluido, l'uso degli Elementi Finiti Misti Ibridi garantisce la proprietà di conservazione della massa, assicurando così un campo di velocità accurato. Nel caso dell'equazione di trasporto è stata adottata una tecnica time-splitting andando a risolvere separatamente il termine convettivo con uno schema ai FV, e quello diffusivo con il metodo degli MHFE. Il codice sviluppato è in grado di riprodurre fenomeni caratterizzati da fronti di temperatura molto marcati, senza introdurre oscillazioni spurie nella soluzione numerica, e non richiede l'impiego di griglie di calcolo estremamente raffinate al fine di assicurare un'adeguata accuratezza. E' stato sviluppato inoltre un modello 3D per lo studio accoppiato di problemi di flusso e deformazione sfruttando l'uso combinato di Elementi Finiti Misti (MFE) e di Elementi Finiti (FE) nella discretizzazione, rispettivamente, dell'equazione di flusso e di equilibrio strutturale. L'impiego di MFE è stato scelto in modo da limitare le oscillazioni numeriche della soluzione che caratterizzano il problema di flusso-deformazione in regioni con forti contrasti di permeabilità. Il sistema lineare che scaturisce dalla discretizzazione delle equazioni di bilancio è stato risolto implementando una tecnica iterativa ad hoc basata sui gradienti coniugati precondizionati. I modelli proposti sono stati testati su alcuni problemi di letteratura e applicati, con successo, a casi di interesse ingegneristico.

Contents

List of Figures

List of Tables

Introduction

Predicting the response of fluid saturated porous media to thermal, pressure and/or mechanical loadings is of paramount importance in many engineering problems. Significant examples deal with groundwater processes, such as flow circulation or water-table fluctuations, heat and fluid transfer in geothermal explorations, heat and moisture flow and stress around buried pipelines, underground waste containment projects, or nuclear waste storage in deep geological formations. Other applications are the study of pavements under freezing-thawing cycles, the transport of pollutants due to heat and fluid diffusion, landfill design, etc. Recently, considerable interest has been devoted to the study of coupled hydro-thermo-mechanical models in porous media, especially connected to fluid injection operations into geological formations. Injection of fluids into the subsurface started with the petroleum industry more than 50 years ago, and nowadays is increasingly used for a variety of purposes such enhanceing oil production (EOR), storing gas in depleted gas/oil fields (UGS), recharging overdrafted aquifer systems (ASR), and mitigate anthropogenic land subsidence.

Although the mechanical coupling between fluids and porous solids has been recognized since the end of the 19th century [e.g., Reynolds, 1886; King, 1892], the first significant advances date back to the 1920s by Terzaghi [1925], who developed the one-dimensional consolidation theory under constant loading. Two crucial ideas are connected with the work of Terzaghi: the notions of effective stress and the diffusion of pressure by flow, linking consolidation directly to the dissipation of excess fluid pressure. These ideas still lie at the core of current understanding of hydromechanical coupling and fluid flow through porous media. However, the conceptual breakthrough occurred when Biot published the theory of three-dimensional consolidation [Biot, 1941], also known as poroelasticity theory, developing the mathematical framework governing the coupled fluid flow and deformation. This is the basis of a more general description of hydromechanics in porous media. Several other issues were addressed and clarified in the following decades [e.g., Geertsma, 1966; Verruijt, 1969; Rice & Cleary, 1976], incorporating also thermal effects

[e.g., McTigue, 1986; Kurashige, 1989] in a thermoporoelastic theory. The solution to the partial differential equations governing the thermoporoelastic behaviour of real fluid saturated heterogeneous porous media are typically addressed by numerical strategies. Despite the intensive research carried out in recent years, numerical solution to thermo-poro-elasticity still represents a demanding task.

The main goal of this Ph.D. dissertation is to propose a robust, efficient and accurate numerical approach to address thermoporoelastic problems, with particular emphasis on the simulation of fluid injection/pumping operations into geological formations. In this respect, two models based on traditional Finite Elements (FEs), Mixed Finite Element (MFEs) and Finite Volumes (FVs) have been developed and implemented, addressing at first the coupled fluid flow and heat transfer in deformable porous media, then the fully coupled consolidation under isothermal conditions. The thesis is organized as follows:

chapter 1: the mathematical model describing the behaviour of a deformable fluid-saturated porous medium is discussed. The constitutive relationships and the governing balance laws are reviewed, assuming a linear thermoporoelastic framework;

chapter 2: a numerical model for heat transfer in saturated porous media is discussed. The model, consisting of a nonlinear system of coupled flow and heat transfer partial differential equations, is solved using Godunov-Mixed Methods (GMMs), where an explicit Finite-Volume Godunov technique is used for the convective flux with an implicit Mixed Finite Element technique for heat conduction. An implicit Mixed Finite Element discretization is also used to solve the flow equation. The model is tested on Elder's problem, in both the classical two- and extended three-dimensional configurations. The simulation of seawater injection into a faulted aquifer is also presented to emphasize the benefits of the proposed approach;

chapter 3: a fully coupled 3-D Mixed Finite Element model is developed for the numerical solution to the Biot equations of 3-D consolidation, a still challenging issue because of the ill-conditioning of the resulting algebraic system and the instabilities that may affect the pore pressure solution. In particular, the main purpouse of proposed approach is alleviating the pore pressure numerical oscillations at the interface between materials with different permeabilities. An ad hoc solution algorithm is implemented that takes advantage of the block structure of the discretized problem. The proposed model is then validated against well-known analytical solutions;

chapter 4: the proposed numerical models are applied to several large-size realistic and computationally challenging applications set in the Venice lagoon. In all simulations, the most recent available hydrogeological, geothermal and geomechanical data from the Northern Adriatic basin are used. The consolidation of a shallow formation is also addressed because of the construction of a trial embankment and a groundwater withdrawal. Afterwards, the pilot project of anthropogenic uplift of Venice by deep seawater injection, which has been recently advanced by Castelletto *et al.* [2008], is discussed. The proposal, aiming at mitigating the floods that periodically plague the city, is supplemented with the investigation of the role played by a temperature variation should the injection take place in non-isothermal conditions.

Chapter 1

Mathematical model of single-phase flow in deformable porous media

1.1 Introduction

A porous medium is defined as a multiphase body consisting of a solid matrix with the voids filled either by a single- or a multi-phase fluid (e.g., gas, water and oil). The matrix consists of solid grains through which no filtration is possible. The connected pores are the volume where fluid flow may occur.

The thermomechanical behaviour of fluid saturated porous rock is important in a number of different areas, such as the enhanced oil recovery by hot fluid injection, the extraction of geothermal energy, or the design of underground nuclear waste storage site. Moreover, non-isothermal porous media can be encountered in several engineering applications. Under certain circumstances these problems may involve significant coupling between heat transfer, pore pressure and flow of the interstitial fluid, and deformation of the porous matrix. For example, a pore fluid pressure change or a temperature variation can alter the bulk equilibrium and involve either a volumetric expansion or contraction. Such a deformation of the porous matrix in its turn impacts on both the storage capacity and hydraulic trasmissivity properties, affecting the fluid flow and the temperature field evolution.

The earliest studies on coupled phenomena between mechanics and flow in porous media date back to Terzaghi [1925], who developed a one-dimensional consolidation theory for saturated soils undergoing constant loading. A generalized formulation for the coupling between pore pressure and stresses in porous media was later established by Biot [1941,

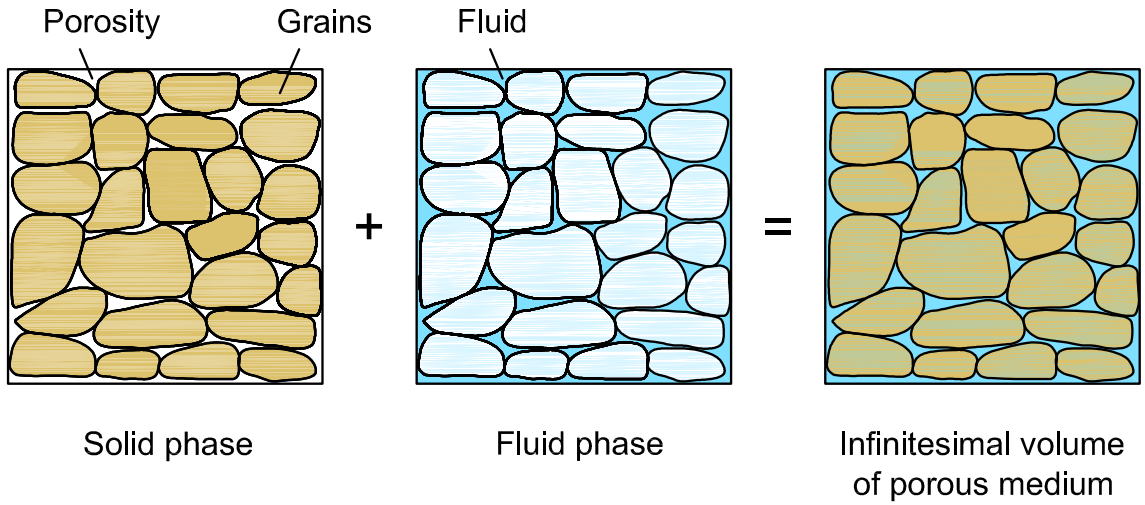

Figure 1.1: Schematic representation of a saturated porous medium: the solid phase and the fluid phase are interpreted as overlapping continua.

1956]. Biot's three-dimensional consolidation theory was recasted by Rice & Cleary [1976], and extented to non-isothermal conditions [e.g., McTigue, 1986; Kurashige, 1989].

Macroscopic models of porous media use a continuum representation. In the present work a single fluid phase is considered with the porous medium treated as two overlapping continuous media, the solid matrix and the fluid, respectively. Such an approach assumes the existence of a representative elementary volume (REV) with well defined average properties (Fig. 1.1). In particular, a REV is defined when the porosity ϕ, i.e. the ratio of the volume of voids to the total volume (solid + voids), approaches a stable limit.

In the present chapter the constitutive relationships and balance laws governing the behaviour of deformable fluid-saturated porous media are reviewed. A linear thermoporoelastic framework is selected with the following assumptions [Verruijt, 1969; Detournay & Cheng, 1993; Coussy, 2004]:

- isotropic linear thermoporoelastic solid matrix;
- single-phase flow;
- small deformation;
- instantaneous thermal equilibrium between the solid and the fluid phases.

1.2 Equations of state and constitutive equations

The equations of state for solid and fluid phase along with a set of constitutive equations are necessary to describe the non-isothermal response of a saturated porous medium to external loading. They provide the auxiliary relatioships needed to solve the balance laws. In this pararagraph, the equations of state for solid and fluid densities and fluid viscosity are described as well as the selected constitutive relationships, consisting of the thermoporoelasticity equations, Darcy's law and Fourier's law.

1.2.1 Density and viscosity

The fluid phase (f) and the solid grain (s) densities are generally regarded as a function of the state variables pressure p and temperature θ, in the form:

$$\rho_i = \rho_i(p, \theta) \qquad i = f, s \tag{1.1}$$

The total differential of (1.1) yields:

$$\begin{aligned} d\rho_i &= \frac{\partial \rho_i}{\partial p} dp + \frac{\partial \rho_i}{\partial \theta} d\theta \\ &= \underbrace{\left(\frac{1}{\rho_i} \frac{\partial \rho_i}{\partial p} \right)}_{\beta_i} \rho_i dp + \underbrace{\left(\frac{1}{\rho_i} \frac{\partial \rho_i}{\partial \theta} \right)}_{-3\beta_i'} \rho_i d\theta \\ &= \beta_i \rho_i dp - 3\beta_i' \rho_i d\theta \end{aligned} \tag{1.2}$$

where

- β_i is the the compressibility of phase i;
- $3\beta_i'$ is the volumetric thermal expansion coefficient of phase i, i.e. three times the linear one under the hypothesis of isotropic behaviour.

If β_f, β_s, β_f', and β_s' are assumed to be constant, integration of Equation (1.2) leads to the state equation for each phase in the form [Fernandez, 1972]:

$$\begin{aligned} \rho_i &= \rho_{i,0} e^{\beta_i (p - p_0) - 3\beta_i' (\theta - \theta_0)} \\ &\approx \rho_{i,0} \left[1 + \beta_i (p - p_0) - 3\beta_i' (\theta - \theta_0) \right] \end{aligned} \tag{1.3}$$

where $\rho_{i,0}$ is the reference value at pressure p_0 and reference temperature θ_0.

Although the dynamic viscosity of the fluid μ_f is also a function of both pressure and temperature, it exhibits a strong dependence on temperature and little on pressure.

Several empirical formulas can be found in the literature. For example, a relationship proposed by Mercer & Pinder [1974] for water is:

$$\frac{1}{\mu_f(\theta)} = \frac{1 + 0.7063\zeta - 0.04832\zeta^3}{\mu_{f,0}} \tag{1.4}$$

with $\zeta = \dfrac{\theta - 150}{100}$ expressing θ in °C and the reference viscosity $\mu_{f,0}$ evaluated at 150 °C. If the range of temperature is not too large, the dynamic viscosity can be written as a linear function of θ and $\mu_{f,0}$ as:

$$\mu_f = \mu_{f,0}\left[1 + \alpha(\theta - \theta_0)\right] \tag{1.5}$$

where $\alpha = (\mu_{f,1} - \mu_{f,0})/(\theta_1 - \theta_0)$ and $\mu_{f,1}$ is the viscosity at a convenient temperature θ_1.

1.2.2 Thermoporoelastic constitutive equations

A thermoporoelastic system depends on six variables grouped in conjugate pairs:

- total stress $\boldsymbol{\sigma}$ and linearized strain $\boldsymbol{\epsilon}$;
- pore pressure p and fluid mass content m;
- temperature θ and specific entropy s.

The fluid mass content is the fluid mass per unit volume of porous medium [Rice & Cleary, 1976]. The specific entropy is similarly defined as the entropy of the satutared porous medium per unit volume [McTigue, 1986]. Pore pressure, fluid mass content, temperature and specific entropy are scalar variables while the total stress and strain are both rank-2 symmetric tensors with six components each. The total tensor components σ_{ij} of the applied stress on a unit reference volume are shown in Figure 1.2: the first and second indeces denote the lying plane and the direction of the stresses, respectively. The classical continuum mechanics stress sign convention for the stresses is adopted, namely tensile stresses are positive and compressive stresses are negative. The strain tensor components ϵ_{ij} (Figure 1.3) for a fluid-filled porous medium are the same as in an elastic

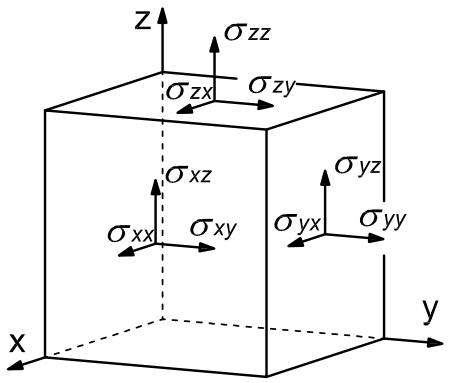

Figure 1.2: Total stress tensor components on an REV.

continuum [Means, 1976]:

$$\epsilon_{xx} = \frac{\partial u}{\partial x} \tag{1.6a}$$

$$\epsilon_{yy} = \frac{\partial v}{\partial y} \tag{1.6b}$$

$$\epsilon_{zz} = \frac{\partial w}{\partial z} \tag{1.6c}$$

$$\epsilon_{xy} = \epsilon_{yx} = \frac{1}{2}\left(\frac{\partial u}{\partial y} + \frac{\partial v}{\partial x}\right) \tag{1.6d}$$

$$\epsilon_{xz} = \epsilon_{zx} = \frac{1}{2}\left(\frac{\partial u}{\partial z} + \frac{\partial w}{\partial x}\right) \tag{1.6e}$$

$$\epsilon_{yz} = \epsilon_{zy} = \frac{1}{2}\left(\frac{\partial v}{\partial z} + \frac{\partial w}{\partial y}\right) \tag{1.6f}$$

where u, v and w are the displacement components in a cartesian coordinate system.

A set of independent variables consists of one variable for each pair. The possible permutations of independent and dependent variables are eight, each one leading to a peculiar form of the constitutive relationships based on different physical properties, assumed constant in linear thermoporoelasticity, of the saturated porous medium [Wang, 2001; Coussy, 2004]. In the following, the changes in total stress, fluid mass content and specific entropy (dependent variables) are linked to changes in strain, fluid pressure and temperature (independent variables).

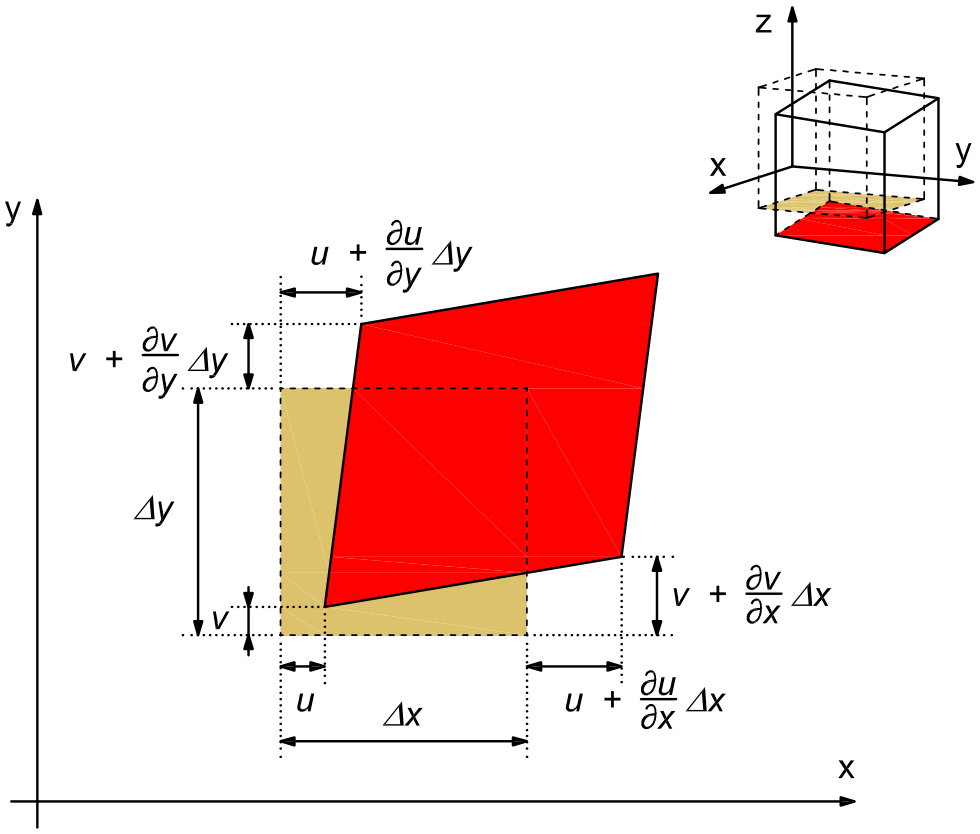

Figure 1.3: Strain tensor components on an REV.

Denoting with the subscript 0 the reference state, the thermoporoelastic constitutive equations can be expressed as [Coussy, 2004]:

$$\boldsymbol{\sigma} - \boldsymbol{\sigma}_0 = \mathbf{C}_{dr} : \boldsymbol{\epsilon} - b\,(p - p_0)\,\mathbf{1} - 3\beta'_s K\,(\theta - \theta_0)\,\mathbf{1} \tag{1.7a}$$

$$\frac{1}{\rho_{0,f}}(m - m_0) = b\epsilon_v + \frac{1}{M}\,(p - p_0) - 3\beta'_M\,(\theta - \theta_0) \tag{1.7b}$$

$$s - s_0 = 3\beta'_s K\epsilon_v - 3\beta'_M\,(p - p_0) + \frac{c_{v,M}}{\theta_0}\,(\theta - \theta_0) \tag{1.7c}$$

where:

- $\mathbf{C}_{dr}$ is the drained rank-4 elasticity tensor. For an isotropic medium it depends on two coefficients only;
- $b = 1 - \dfrac{K}{K_s}$ is the Biot coefficient, $K = \dfrac{E}{3(1-2\nu)}$ is the bulk modulus of the drained skeleton and K_s is the bulk modulus of the solid phase. E and ν are the elastic modulus and the Poisson coefficient, respectively;
- $\mathbf{1}$ is the rank-2 identity tensor;
- $\epsilon_v = \mathrm{trace}(\boldsymbol{\epsilon}) = \epsilon_{xx} + \epsilon_{yy} + \epsilon_{zz}$ is the volumetric strain;
- $M = \left(\dfrac{b-\phi}{K_s} + \dfrac{\phi}{K_f}\right)^{-1}$ is the Biot modulus, with K_f the fluid bulk modulus;
- $\beta'_M = (b-\phi)\beta'_s + \phi\beta'_f$ is the equivalent thermal expansion coefficient of the porous medium;
- $c_{v,M} = (b-\phi)c_{v,s} + \phi c_{v,f}$ is the equivalent volumetric heat capacity of the porous medium.

The strain tensor $\boldsymbol{\epsilon}$ can be split into the sum of a volumetric component and a deviatoric component:

$$\boldsymbol{\epsilon} = \frac{1}{3}\epsilon_v\mathbf{1} + \mathbf{e} = \frac{1}{3}\epsilon_v \begin{bmatrix} 1 & 0 & 0 \\ 0 & 1 & 0 \\ 0 & 0 & 1 \end{bmatrix} + \begin{bmatrix} \epsilon_{xx} - \frac{\epsilon_v}{3} & \epsilon_{xy} & \epsilon_{xz} \\ \epsilon_{yx} & \epsilon_{yy} - \frac{\epsilon_v}{3} & \epsilon_{yz} \\ \epsilon_{zx} & \epsilon_{zy} & \epsilon_{zz} - \frac{\epsilon_v}{3} \end{bmatrix} \tag{1.8}$$

with $\mathbf{e}$ the deviatoric tensor. If the strain tensor decomposition (1.8) is used, and $\mathbf{C}_{dr}$ is expressed as a function of the bulk modulus K and the shear modulus $G = \dfrac{E}{2(1-2\nu)}$, equation (1.7a) reduces to:

$$\boldsymbol{\sigma} - \boldsymbol{\sigma}_0 = (K\epsilon_v\mathbf{1} + 2G\mathbf{e}) - b\,(p - p_0)\,\mathbf{1} - 3\beta'_s K\,(\theta - \theta_0)\,\mathbf{1} \tag{1.9}$$

1.2.3 Darcy's law

The fluid flow in a porous medium is governed by Darcy's law, stating that the specific fluid discharge, i.e. the fluid volume flow rate per unit area and time, is proportional to the piezometric head change. In vector notation, the specific fluid discharge $\mathbf{v}$, also known as Darcy's velocity, reads:

$$\mathbf{v} = -\mathbf{K}\nabla h \tag{1.10}$$

where:

- $\mathbf{K}$ is the rank-2 hydraulic conductivity tensor;
- ∇ is the gradient operator;
- h is the piezometric head.

Equation (1.10) is valid as long as the flow is laminar. A criterion to assess the flow regime is provided by the magnitude of Reynolds number Re (a pure number relating inertial to viscous forces), defined as:

$$Re = \frac{\rho_f \left|\mathbf{v}\right| d}{\mu_f} \tag{1.11}$$

where

- $|\mathbf{v}|$ is the magnitude of Darcy's velocity;
- d the average of diameter of the medium particles.

The threshold value of Re between laminar and turbulent regime ranges from 1 to 10 [Bear, 1988], thus the validity of Darcy's law is warranted whenever $Re \leq 1$.

The hydraulic conductivity reflects the resistance opposed by a porous matrix to the fluid flow and depends on both the fluid (density and viscosity) and the medium properties (grain-size distribution, shape of grains, tortuosity, specific surface and porosity) according to [Nutting, 1930]:

$$\mathbf{K} = \frac{\rho_f g}{\mu_f}\mathbf{k} \tag{1.12}$$

where

- $\mathbf{k}$ is the intrinsic permeability tensor of the porous matrix;
- g is the gravity acceleration.

For an isothermal incompressible fluid the hydraulic head is defined as:

$$h = \frac{p}{\rho_f g} + z \tag{1.13}$$

where:

- $\frac{p}{\rho_f g}$ is the pressure head;
- z is the elevation.

Using (1.12) and (1.13), Equation (1.10) reads:

$$\mathbf{v} = -\frac{\mathbf{k}}{\mu_f}\nabla\left(p - \rho_f g z\right) \tag{1.14}$$

In the form (1.14), Darcy's law, which was originally based on experimental evidence [Darcy, 1856], represents the momentum balance of the fluid phase ($-\mu_f \mathbf{k}^{-1}\mathbf{v}$ is a friction force) recasted in order to describe flow of fluid through porous media. Moreover, the (1.14) holds true also when fluid density and viscosity are not constant [De Smedt, 2007], i.e. when non-isothermal and compressible fluids are considered.

1.2.4 Fourier's law

Fourier's law of heat conduction states that heat transfer by molecular interaction at any point in a solid or a fluid is in magnitude proportional to and in direction coincident with the gradient of the temperature field. The heat flux $\mathbf{q}$ (heat flow rate per unit area and time) is defined as:

$$\mathbf{q} = -\mathbf{\Lambda}\nabla\theta \tag{1.15}$$

where:

- $\mathbf{\Lambda}$ is the rank-2 thermal conductivity tensor.

In case of a fluid-saturated porous medium, the conductive body consists of two phases, with the solid and the fluid phases at the same temperature and an equivalent thermal conductivity tensor defined for the whole medium. The equivalent tensor $\mathbf{\Lambda}_M$ combines the isotropic thermal conductivity of the porous medium $\lambda_M = (b-\phi)\lambda_s + \phi\lambda_f$ in the absence of fluid flow with a term accounting for the macroconductivity due to the heterogeneity of the fluid velocity. For groundwater problems, de Marsily [1986] suggests using Darcy's velocity $\mathbf{v}$ multiplied by the volumetric heat capacity of the fluid $c_{v,f}$ so that the proportionality

coefficient has the dimension of a length. In the longitudinal and trasverse axes relative to $\mathbf{v}$, $\mathbf{\Lambda}_M$ reads:

$$\mathbf{\Lambda}_M = \begin{bmatrix} \lambda_L & 0 & 0 \\ 0 & \lambda_T & 0 \\ 0 & 0 & \lambda_T \end{bmatrix} \quad \text{with} \quad \begin{cases} \lambda_L = \lambda_M + \alpha_L c_{v,f} \mid \mathbf{v} \mid \\ \\ \lambda_T = \lambda_M + \alpha_T c_{v,f} \mid \mathbf{v} \mid \end{cases} \tag{1.16}$$

where α_L, α_T are the longitudinal and transverse thermodispersivity coefficients, respectively.

1.3 Balance laws

The equations governing a coupled pore fluid-solid system in non-isothermal conditions are conservation laws expressing the linear momentum balance, the fluid mass and the energy balance for the mixture.

1.3.1 Linear momentum balance

Assuming a quasi-static condition, the inertia forces are neglected and the equation of mechanical equilibrium for an elemental porous volume is:

$$\nabla \cdot \boldsymbol{\sigma} + \rho \mathbf{g} \;\; = \;\; 0 \tag{1.17}$$

where

- $\nabla\cdot$ is the divergence operator;
- $\boldsymbol{\sigma}$ is the total stress tensor;
- $\rho = \phi\rho_f + (1 - \phi\rho_s)$ is the bulk density;
- $\mathbf{g}$ is the gravity acceleration vector.

Using the constitutive equation (1.9) into Equation (1.17) yields:

$$\nabla \cdot (K\epsilon_v \mathbf{1} + 2G\mathbf{e}) + \rho\mathbf{g} = b\nabla p + 3\beta_s' K \nabla\theta \tag{1.18}$$

i.e.:

$$\begin{aligned}
2G\left(\frac{\partial \epsilon_{xx}}{\partial x}+\frac{\partial \epsilon_{xy}}{\partial y}+\frac{\partial \epsilon_{xz}}{\partial z}\right)+\left(K-\frac{2G}{3}\right)\frac{\partial \epsilon_v}{\partial x}+\rho g_x &= b\frac{\partial p}{\partial x}+3\beta_s' K\frac{\partial \theta}{\partial x}\\
2G\left(\frac{\partial \epsilon_{yx}}{\partial x}+\frac{\partial \epsilon_{yy}}{\partial y}+\frac{\partial \epsilon_{yz}}{\partial z}\right)+\left(K-\frac{2G}{3}\right)\frac{\partial \epsilon_v}{\partial y}+\rho g_y &= b\frac{\partial p}{\partial y}+3\beta_s' K\frac{\partial \theta}{\partial y}\\
2G\left(\frac{\partial \epsilon_{zx}}{\partial x}+\frac{\partial \epsilon_{zy}}{\partial y}+\frac{\partial \epsilon_{zz}}{\partial z}\right)+\left(K-\frac{2G}{3}\right)\frac{\partial \epsilon_v}{\partial z}+\rho g_z &= b\frac{\partial p}{\partial z}+3\beta_s' K\frac{\partial \theta}{\partial z}
\end{aligned} \tag{1.19}$$

Finally, using equations (1.6a) through (1.6f), the classical equilibrium in terms of displacements is recovered [van der Knaap, 1959; Geertsma, 1966; Bai & Abousleiman, 1997]:

$$\begin{aligned}
G\nabla^2 u+\left(K+\frac{G}{3}\right)\frac{\partial \epsilon_v}{\partial x}+\rho g_x &= b\frac{\partial p}{\partial x}+3\beta_s' K\frac{\partial \theta}{\partial x}\\
G\nabla^2 v+\left(K+\frac{G}{3}\right)\frac{\partial \epsilon_v}{\partial y}+\rho g_y &= b\frac{\partial p}{\partial y}+3\beta_s' K\frac{\partial \theta}{\partial y}\\
G\nabla^2 w+\left(K+\frac{G}{3}\right)\frac{\partial \epsilon_v}{\partial z}+\rho g_z &= b\frac{\partial p}{\partial z}+3\beta_s' K\frac{\partial \theta}{\partial z}
\end{aligned} \tag{1.20}$$

with ∇^2 the Laplace operator.

1.3.2 Fluid mass balance

If no chemical reaction is considered, the conservation of mass for a control volume reads:

$$\frac{\partial m}{\partial t} = -\nabla\cdot(\rho_f \mathbf{v})+\rho_{f,*} f \tag{1.21}$$

where

- $\rho_{f,*} f$ is a source term with $\rho_{f,*}$ the source fluid density and f a volumetric source term.

Using Equation (1.7b), the mass balance equation (1.21) is written in terms of volumetric strain, pressure and temperature:

$$b\frac{\partial \epsilon_v}{\partial t}+\frac{1}{M}\frac{\partial p}{\partial t}-3\beta_M'\frac{\partial \theta}{\partial t} = -\nabla\cdot\left(\frac{\rho_f}{\rho_{f,0}}\mathbf{v}\right)+\frac{\rho_{f,*}}{\rho_{f,0}} f \tag{1.22}$$

1.3.3 Energy balance

The heat balance should be prescribed for each phase separately. However, the local thermal equilibrium assumption allows for imposing a single balance equation for the whole fluid-filled porous medium with a unique temperature θ. The equation reads:

$$\theta_0 \frac{\partial s}{\partial t} = -\nabla \cdot \mathbf{q} - \nabla \cdot (c_{v,f} \theta \mathbf{v}) + c_{v,f,*} \theta_* f \tag{1.23}$$

where

- $c_{v,f,*}\theta_* f$ is a source term, with c_{v,f_*} the source volumetric heat capacity and θ_* the fluid source fluid temperature.

In Equation (1.23) the first term on the right-hand side describes the conductive heat transport while the second one accounts for the convective heat transport.

Using the constitutive Equation (1.7c) in Equation (1.23) yields a balance relationship in terms of the selected independent thermoporoelastic variables:

$$3\beta_s' \theta_0 K \frac{\partial \epsilon_v}{\partial t} - 3\beta_M' \theta_0 \frac{\partial p}{\partial t} + c_{v,M} \frac{\partial \theta}{\partial t} = -\nabla \cdot \mathbf{q} - \nabla \cdot (c_{v,f} \theta \mathbf{v}) + c_{v,f,*} \theta_* f \tag{1.24}$$

The first and the second terms on the left-hand side of (1.24) account for the latent heat of the porous medium associated with the skeleton and the fluid volumetric expansion, respectively. As is tipically observed in linear thermoelasticity, such contributions are negligible for water saturated rock [McTigue, 1986] and for most porous materials in general [Coussy, 2004]. Hence, the final form for the energy balance reads:

$$c_{v,M} \frac{\partial \theta}{\partial t} = -\nabla \cdot \mathbf{q} - \nabla \cdot (c_{v,f} \theta \mathbf{v}) + c_{v,f,*} \theta_* f \tag{1.25}$$

1.4 Uncoupling equilibrium and flow-heat transfer equations

The set of coupled partial differential equations (1.14), (1.15), (1.20), (1.22) and (1.25) represent the non-isothermal form of the original Biot's equations [Biot, 1941]. In case of multi-aquifer systems, such equations can be extended to transversely isotropic media with the elasticity tensor $\mathbf{C}_{dr}$ depending on five independent mechanical parameters. Analytical solutions can be obtained only for a few realistic problems and numerical techniques are needed.

In some applications, the model complexity can be reduced. Differentiating the first equation of (1.20) with respect to x, the second with respect to y and the third with respect to z, and adding the results, yields:

$$\left(K + \frac{4G}{3}\right) \nabla^2 \varepsilon_v = b\nabla^2 p + 3\beta_s' K \nabla^2 \theta \tag{1.26}$$

By integrating (1.26), we obtain:

$$\left(K + \frac{4G}{3}\right) \varepsilon_v = bp + 3\beta_s' K\theta + h(x, y, z, t) \tag{1.27}$$

where h is a generic harmonic function, i.e. $\nabla^2 h = 0$ at any time t. An explicit expression for h was obtained by Verruijt [1969] in problems of flow in leaky aquifer. In particular, when $h = 0$ in equation (1.27), the following relationship for ε_v holds true:

$$\varepsilon_v = c_M \left(bp + 3\beta_s' K\theta\right) \tag{1.28}$$

where

$$c_M = \left(K + \frac{4G}{3}\right)^{-1}$$

is the vertical uniaxial compressibility of the porous matrix.

Substituting (1.27) into (1.22), yields:

$$\eta_p \frac{\partial p}{\partial t} - \eta_T \frac{\partial \theta}{\partial t} \;=\; -\nabla \cdot \left(\frac{\rho_f}{\rho_{f,0}} \mathbf{v}\right) + \frac{\rho_{f,*}}{\rho_{f,0}} f \tag{1.29}$$

where:

- $\eta_p = \frac{S_s}{\rho_0 g}$, $S_s = \rho_0 g(bc_M + M^{-1})$ is the elastic storage coefficient as defined in Gambolati [1973];
- $\eta_T = 3[(b - \phi - bc_M K)\beta_s' + \phi\beta_f']$.

The mass balance equation in the form (1.29) is decoupled from (1.20) and the medium structural behaviour is accounted for by into two lumped mechanical parameters, i.e. η_p and η_θ. Hence, the flow (1.14), (1.29) and the heat transfer (1.15), (1.25) models may be solved for the pressure p and the temperature θ with the p and θ solutions subsequently used in (1.20) to obtain the medium displacements.

The method described above was originally derived by Terzaghi [1925] for isothermal conditions and it is rigorous for one-dimensional consolidation problems. Depending on the characteristic temporal and spatial scales, two- and three-dimensional [Gambolati,

1992] deforming fields can also be treated by an uncoupled approach without losing accuracy of the pressure, the temperature and the displacements fields, respectively [Gambolati *et al.*, 2000]. In many realistic geomechanical applications, the uncoupled technique has been succesfully employed [e.g., Brutsaert & Corapcioglu, 1976; Martin & Serdengecti, 1984; Rivera *et al.*, 1991; Doornhof, 1992; Gambolati *et al.*, 2000; Teatini *et al.*, 2000; Comerlati *et al.*, 2005; Teatini *et al.*, 2006; Ferronato *et al.*, 2008], providing reliable predictions of the medium displacements along with a computationally cheaper algorithm. On the other hand, in the same field of applications, coupling needs to be taken into account at much smaller scales [Ferronato *et al.*, 2003b].

Chapter 2

Godunov-Mixed Methods for coupled fluid flow and heat transfer

2.1 Introduction

The main mechanisms of heat transfer into a geological formation are two: heat conduction and heat convection. Heat conduction is the transfer of heat by the activation of solid and fluid particles, without their bulk movement. Heat convection on the other hand is due to the bulk motion of the particles. As the motion of the solid particles is negligible relative to the fluid flow, the convective heat transfer basically depends on the latter. The heat conduction is governed by Fourier's law while the heat convection depends on the rate of fluid flow.

In low permeable formations, such as granitic rock masses, the rate of fluid flow is so slow that heat convection is negligible [e.g., McTigue, 1986; Wang & Papamichos, 1994; Nguyen & Selvadurai, 1995]. Hence, heat conduction is predominant and a pure conductive model can be used. Conversely, with a greater fluid velocity, such as in geothermal energy extraction, petroleum reservoir production or underground fluid injection operations, the convective heat transfer may also play an important role.

Several analytical and numerical strategies have been advanced for solving flow through porous media and heat transfer. Analytical methods exhibit several limitations, e.g. simple geometric configurations with ad hoc boundary and initial conditions, while numerical methods proved powerful tools to address realistic field problems. Numerical methods basically differ on the way the time-dependent terms of the heat transfer equation are discretized. A first class includes numerical schemes relying on finite difference (FD) or finite

element (FE) methods [e.g., Necati Özisik, 1994; Lewis & Schrefler, 1998; Zienkiewicz *et al.*, 1999] which typically handle the convective and conductive terms simultaneously using the same discretization. However, in convection-dominated problems such methods may lead to non-physical responses, such as spurious oscillations near sharp temperature fronts, requiring highly refined grids to obtain accurate numerical results. Other approaches, based on time-operator splitting techniques [Richtmyer & Morton, 1967; Yanenko, 1971], isolate the conductive from the convective contribution yielding two partial differential equations solved with independent discretizations. The main advantage of these methods is the great flexibility in selecting the most appropriate solution methods for the convection and the conduction processes. Among the splitting methods, the Godunov-Mixed Methods (GMMs) combine a Godunov-type method, i.e. a finite volume (FV) technique originally developed for purely hyperbolic non-dissipative systems [Godunov, 1959; van Leer, 1979], with a mixed finite element (MFE) method in the discretization of the convective and conductive terms, respectively [Dawson, 1990, 1991, 1993; Mazzia *et al.*, 2000; Mazzia & Putti, 2005].

In the present chapter a Mixed Hybrid Finite Element (MHFE) method for the discretization of both the flow and the heat transfer equation, in the latter combined with a High Resolution Finite Volume (HRFV) scheme via a time-splitting technique. The reasons of this choice are twofold. First, the MHFE scheme applied to the flow equation yields a conservative discrete velocity field with normal components that are continuous across inter-element boundaries. This property guarantees that no mass balance errors due to numerical inaccuracies in the flow problem are introduced in the heat transfer equation. Second, the HRFV method used for the convection term is able to simulate accurately very sharp fronts following their evolution in time. After recalling the governing equations, the spatial and temporal discretizations are presented along with the Picard linearization scheme. The model is then validated against a classical benchmark problem in the literature, i.e. the Elder problem [Elder, 1967b], in both the classical two- and extended three-dimensional configurations. The distinctive features of the proposed approach are emphasized in the simulation of seawater injection into a deep aquifer.

2.2 Mathematical model

In the uncoupled formulation of thermoporoelasticity, the fluid flow and heat transfer in saturated porous media are described by a set of coupled conservation laws expressing the fluid mass and energy balances. The fluid density and viscosity depend on p and θ

accordingly to suitable equations of state (equations (1.3) and (1.5)). The coupled system of saturated flow and heat transfer equations reads:

$$\mathbf{v} = -\overline{\boldsymbol{\kappa}}\nabla\left(p + \rho_f g z\right) \tag{2.1a}$$

$$\eta_p \frac{\partial p}{\partial t} - \eta_T \frac{\partial \theta}{\partial t} = -\nabla \cdot \left(\frac{\rho_f}{\rho_{f,0}}\mathbf{v}\right) + \frac{\rho_{f,*}}{\rho_{f,0}} f \tag{2.1b}$$

$$\mathbf{q} = -\boldsymbol{\Lambda}\nabla\theta \tag{2.1c}$$

$$c_{v,M}\frac{\partial \theta}{\partial t} = -\nabla \cdot \left(\mathbf{q} + c_{v,f}\theta\mathbf{v}\right) + c_{v,f}\theta_* f \tag{2.1d}$$

where $\overline{\boldsymbol{\kappa}} = \frac{\mu_{f,0}}{\mu_f}\frac{\mathbf{K}_0}{\rho_{f,0} g}$, and $\mathbf{K}_0$ is the saturated hydraulic conductivity tensor at the reference density and viscosity.

Appropriate initial and boundary conditions have to be added for the well-posedness of the mathematical model (2.1a) to (2.1d). As far as the fluid flow is concerned, these take the form:

$$p(\mathbf{x}, 0) = p_{in}(\mathbf{x}, 0) \tag{2.2a}$$

$$\mathbf{v}(\mathbf{x}, 0) = \mathbf{v}_{in}(\mathbf{x}, 0) \tag{2.2b}$$

$$p(\mathbf{x}, t) = p_p(\mathbf{x}, t) \quad \text{over } \Gamma_p \tag{2.2c}$$

$$\mathbf{v}(\mathbf{x}, t) \cdot \mathbf{n}_v(\mathbf{x}) = u_v(\mathbf{x}, t) \quad \text{over } \Gamma_v \tag{2.2d}$$

where:

- $\mathbf{x}$ is the Cartesian spatial coordinate vector;
- p_{in} is the pressure at the initial time;
- $\mathbf{v}_{in}$ is Darcy's velocity at the initial time;
- p_p is the prescribed pressure (Dirichlet condition) over Γ_p;
- $\mathbf{n}_v$ is the outward unit normal to Γ_v;
- u_v is the prescribed fluid flux (Neumann condition) over Γ_v.

For the heat transfer, the initial and boundary conditions are:

$$\theta(\mathbf{x},0) = \theta_{in}(\mathbf{x},0) \tag{2.3a}$$

$$\mathbf{q}(\mathbf{x},0) = \mathbf{q}_{in}(\mathbf{x},0) \tag{2.3b}$$

$$\theta(\mathbf{x},t) = \theta_\theta(\mathbf{x},t) \quad \text{over } \Gamma_\theta \tag{2.3c}$$

$$\mathbf{q}(\mathbf{x},t)\cdot\mathbf{n}_q(\mathbf{x}) = q_q(\mathbf{x},t) \quad \text{over } \Gamma_q \tag{2.3d}$$

$$(c_{v,f}\theta\mathbf{v}+\mathbf{q})\cdot\mathbf{n}_c = q_c(\mathbf{x},t) \quad \text{over } \Gamma_c \tag{2.3e}$$

where:

- θ_{in} is the temperature at the initial time;
- $\mathbf{q}_{in}$ is the heat flux at the initial time;
- θ_θ is the prescribed temperature (Dirichlet condition) over Γ_θ;
- $\mathbf{n}_q$ and $\mathbf{n}_c$ are the outward unit normal to Γ_q and Γ_c, respectively;
- q_q is the prescribed conductive heat flux (Neumann condition) over Γ_q;
- q_c is the prescribed total (conductive plus convective) heat flux (Cauchy condition) on boundary Γ_c.

The system (2.1a)-(2.1d) is coupled because of the flow dependence temperature in equation (2.1b) and the thermal balance dependence on pressure in equation (2.1d) via Darcy's law. In case of constant density and viscosity, i.e. $\beta_f = \beta'_f = \alpha = 0$, coupling is ensured by the velocity term in (2.1d). Although the system is physically coupled, mathemathically it is not and equations (2.1b) and (2.1d) can be solved sequentially. However, generally the system is irreducible and nonlinear.

2.3 Numerical model

The solution to system (2.1a)-(2.1d) is addressed by Picard-like scheme which decouples the problem solving the flow equation first, computing the velocity field, solving the thermal equation, and finally iterating to convergence (Figure 2.1). The flow equation is discretized by MHFEs, while a time-splitting technique based on the combined use of cell-centered FVs and MHFEs is used for the heat transfer equation. Using this approach a single computational grid can be employed to discretize the domain $\Omega \subset \mathbb{R}^d$ ($d = 2$ or 3). Triangular or tetrahedral elements are used in the two-dimensional and the three-dimensional case, respectively.

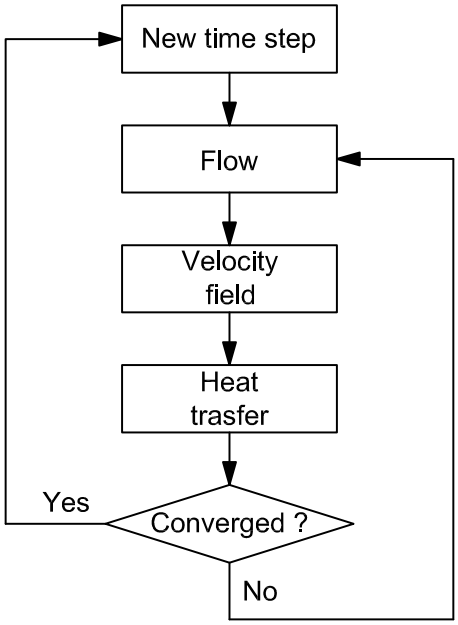

Figure 2.1: Flow chart of the sequential iterative approach.

2.3.1 Dicretization of the flow equation

The MHFE method finds a solution to the flow problem (2.1a)-(2.1b) by approximating both p and $\mathbf{v}$. Let $\mathcal{T}$ be a partition of Ω with n_e elements T_j $(j = 1, \ldots, n_e)$ and n_f internal elemental edges e_j $(j = 1, \ldots, n_f)$. If a generic element T_ℓ is considered, its edges can be identified by two superscript denoting T_ℓ and its neighbour element index sharing each edge, i.e. $e^{\ell,\ell_j} = T_\ell \cap T_{\ell_j}$ $(j = 1, \ldots, d+1)$. The pressure p is approximated by:

$$p(\mathbf{x}, t) \simeq \sum_{j=1}^{n_e} p_j(t) h_j(\mathbf{x}) \tag{2.4}$$

where h_j is an element-wise constant function equal to one over T_j and zero elsewhere with p_j the T_j elemental pressures. The element-wise Darcy's velocity $\mathbf{v}^\ell$ is defined as a linear combination of the $(d+1)$ edge fluxes:

$$\mathbf{v}^\ell(\mathbf{x}, t) \simeq \sum_{j=1}^{d+1} u^{\ell,\ell_j}(t) \mathbf{w}^{\ell,j}(\mathbf{x}) \qquad \ell = 1, \ldots, n_e \tag{2.5}$$

where $\mathbf{w}^{\ell,j}$ are vector basis functions selected in the zero-degree Raviart-Thomas space of degree zero [Raviart and Thomas, 1977] so as to produce a unit outward flux across the edge e^{ℓ,ℓ_j} and zero on all other edges. Coefficient u^{ℓ,ℓ_j} represents the value of the normal flux across edge e^{ℓ,ℓ_j} of T_ℓ. The support for each $\mathbf{w}^{\ell,j}$ is T_ℓ only with the following

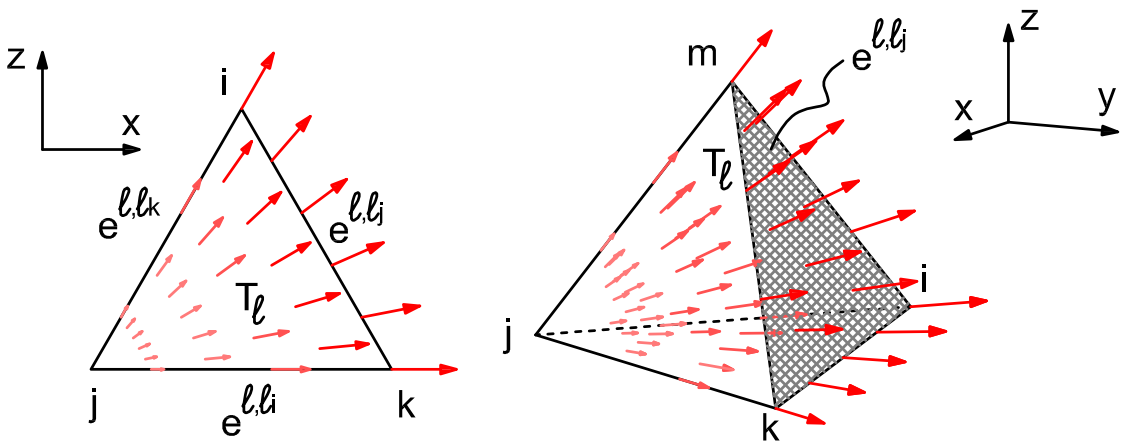

Figure 2.2: Vector basis function $\mathbf{w}^{\ell,j}$ on a triangular element and on a tetrahedral element.

expression:

$$\mathbf{w}^{\ell,j}(\mathbf{x}) = \frac{1}{d|T_\ell|}(\mathbf{x} - \mathbf{x}_j) \tag{2.6}$$

where $|T_\ell|$ is the area ($d = 2$) or the volume ($d = 3$) of T_ℓ and $\mathbf{x}_j$ is the position vector of the node opposite to e^{ℓ,ℓ_j} in T_ℓ (see Figure 2.2). Because of the local $\mathbf{w}^{\ell,j}$ support the continuity of $\mathbf{v}$ across inter-element edges e_j, i.e.:

$$\mathbf{v}^{\ell_L} \cdot \mathbf{n}^{\ell_L,\ell_R} + \mathbf{v}^{\ell_R} \cdot \mathbf{n}^{\ell_R,\ell_L} = 0 \tag{2.7}$$

is generally not satisfied, with $\mathbf{n}^{\ell_L,\ell_R}$ and $\mathbf{n}^{\ell_R,\ell_L}$ the outward unit normal to edge e_j shared by T_{ℓ_L} and T_{ℓ_R} for element T_{ℓ_L} and T_{ℓ_R}, respectively. In the MHFE method such continuity is obtained enforcing equation (2.7) and introducing the pressure ψ at the elemental edges as a Lagrange multiplier [Quarteroni & Valli, 1994]:

$$\psi(\mathbf{x}, t) \simeq \sum_{j=1}^{n_f} \psi_j(t)\varphi_j(\mathbf{x}) \tag{2.8}$$

where φ_j are piecewise basis function equal to one over edge e_j and zero elsewhere. A summary of the degrees of freedom used with the MHFE approach is shown in Figure (2.3) for triangular and tetrahedral elements.

Let us develop a variational form of equations (2.1a)-(2.1b) by orthogonalizing the residuals to $\mathbf{w}^{\ell,i}$ and h_ℓ, respectively, over Ω. Because of the local support of the test

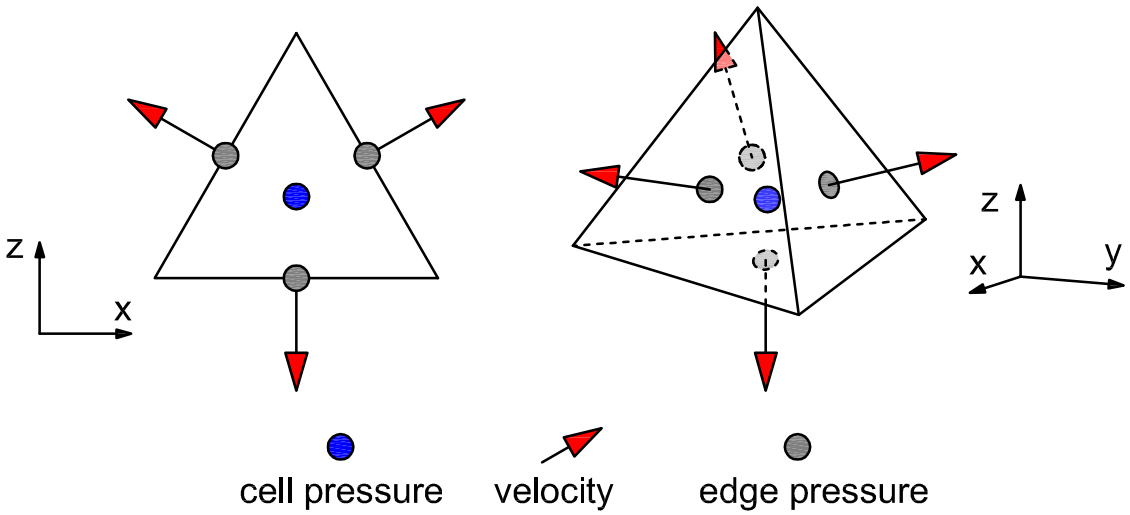

Figure 2.3: Locations of the different unknowns (pressure, fluid velocity and edge pressure) on triangular and tetrehedral cells.

functions, the integrals can be restricted to T_ℓ only:

$$\int_{T_\ell} \overline{\boldsymbol{\kappa}}^{-1}\mathbf{v}^\ell \cdot \mathbf{w}^{\ell,i} d\Delta + \int_{T_\ell} \nabla p \cdot \mathbf{w}^{\ell,i} d\Delta = -\int_{T_\ell} \nabla\left(\rho_f g z\right) \cdot \mathbf{w}^{\ell,i} d\Delta$$

$$i = 1, \ldots, d+1 \quad \ell = 1, \ldots, n_e \tag{2.9a}$$

$$\int_{T_\ell} \nabla \cdot \left(\frac{\rho_f}{\rho_{f,0}}\mathbf{v}^\ell\right) h_\ell d\Delta + \int_{T_\ell} \eta_p \frac{\partial p}{\partial t} h_\ell d\Delta = \int_{T_\ell} \eta_T \frac{\partial \theta}{\partial t} h_\ell d\Delta + \int_{T_\ell} \frac{\rho_{f,*}}{\rho_{f,0}} f h_\ell d\Delta$$

$$\ell = 1, \ldots, n_e \tag{2.9b}$$

Assuming ρ_f constant over T_ℓ and developing a weak form for the second term on the left-hand side of equation (2.9a), yields:

$$\int_{T_\ell} \overline{\boldsymbol{\kappa}}^{-1}\mathbf{v}^\ell \cdot \mathbf{w}^{\ell,i} d\Delta - \int_{T_\ell} p \nabla \cdot \mathbf{w}^{\ell,i} d\Delta + \int_{e^{\ell,\ell_i}} \psi \mathbf{w}^{\ell,i} \cdot \mathbf{n}^{\ell,\ell_i} d\Gamma =$$

$$= -\int_{T_\ell} \rho_f g \nabla z \cdot \mathbf{w}^{\ell,i} d\Delta \tag{2.10a}$$

$$\int_{T_\ell} \nabla \cdot \mathbf{v}^\ell d\Delta + \int_{T_\ell} \frac{\rho_{f,0}}{\rho_f} \eta_p \frac{\partial p}{\partial t} d\Delta = \int_{T_\ell} \frac{\rho_{f,0}}{\rho_f} \eta_T \frac{\partial \theta}{\partial t} d\Delta + \int_{T_\ell} \frac{\rho_{f,*}}{\rho_f} f d\Delta \tag{2.10b}$$

The normal flux discontinuity at each elemental edge, leading to a violation of the mass conservation, is prevented by adding the weak form of equation (2.7):

$$\int_{e_j} \mathbf{v}^{\ell_L} \cdot \mathbf{n}^{\ell_L,\ell_R} d\Gamma + \int_{e_j} \mathbf{v}^{\ell_R} \cdot \mathbf{n}^{\ell_R,\ell_L} d\Gamma = 0 \tag{2.11}$$

Substitution of (2.4), (2.5), (2.8) into (2.10a), (2.10b) and (2.11) leads to the following set of nonlinear differential-algebraic equations:

$$\begin{array}{rcrcrl} A\mathbf{u} & - & B\mathbf{p} & + & C\boldsymbol{\psi} & = \mathbf{g_1} \\ B^T\mathbf{u} & + & D\dot{\mathbf{p}} & & & = \mathbf{g_2} \\ C^T\mathbf{u} & & & & & = \mathbf{0} \end{array} \tag{2.12}$$

where the unknowns vectors $\mathbf{u}$, $\mathbf{p}$ and $\boldsymbol{\psi}$ are:

$$\mathbf{u} = \begin{bmatrix} \left\{ \begin{array}{c} u^{1,1_1} \\ \vdots \\ u^{1,1_{d+1}} \end{array} \right\} \\ \left\{ \begin{array}{c} u^{2,2_1} \\ \vdots \\ u^{2,2_{d+1}} \end{array} \right\} \\ \vdots \\ \left\{ \begin{array}{c} u^{n_e,n_{e_1}} \\ \vdots \\ u^{n_e,n_{e_{d+1}}} \end{array} \right\} \end{bmatrix} \qquad \mathbf{p} = \begin{bmatrix} p_1 \\ p_2 \\ \vdots \\ p_{n_e} \end{bmatrix} \qquad \boldsymbol{\psi} = \begin{bmatrix} \psi_1 \\ \psi_2 \\ \vdots \\ \psi_{n_f} \end{bmatrix}$$

The matrix A is block diagonal and each block A_ℓ is $(d+1) \times (d+1)$:

$$A_\ell \equiv (a_{ij}^\ell) = \int_{T_\ell} (\overline{\boldsymbol{\kappa}}^\ell)^{-1} \mathbf{w}^{\ell,j} \cdot \mathbf{w}^{\ell,i} d\Delta \qquad i,j = 1,\ldots,d+1$$

thus A is a $(d+1)n_e \times (d+1)n_e$ matrix:

$$A = \begin{bmatrix} A_1 & 0 & 0 & 0 \\ 0 & A_2 & 0 & 0 \\ \vdots & \vdots & \ddots & 0 \\ 0 & 0 & \ldots & A_{ne} \end{bmatrix}$$

The matrix B is also block diagonal, but each block B_ℓ is $(d+1) \times 1$:

$$B_\ell \equiv (b_i^\ell) = \int_{T_\ell} \nabla \cdot \mathbf{w}^{\ell,i} d\Delta \qquad i = 1, \ldots, d+1$$

and

$$B = \begin{bmatrix} B_1 & 0 & 0 & 0 \\ 0 & B_2 & 0 & 0 \\ \vdots & \vdots & \ddots & 0 \\ 0 & 0 & \ldots & B_{ne} \end{bmatrix}$$

The matrix D is $n_e \times n_e$ diagonal with coefficients $d_\ell = \int_{T_\ell} \frac{\rho_{f,0}}{\rho_f} \eta_p^\ell d\Delta$:

$$D = \begin{bmatrix} d_1 & 0 & 0 & 0 \\ 0 & d_2 & 0 & 0 \\ \vdots & \vdots & \ddots & 0 \\ 0 & 0 & \ldots & d_{ne} \end{bmatrix}$$

The matrix C is $(d+1)n_e \times n_f$ and has no simple block structure:

$$C = \begin{bmatrix} C_1 \\ C_2 \\ \vdots \\ C_{n_e} \end{bmatrix}$$

Each row of C has one non-zero entry given by:

$$C_\ell \equiv (c_{ij}^\ell) = \int_{e^{\ell,\ell_i}} \varphi_j \mathbf{w}^{\ell,i} \cdot \mathbf{n}^{\ell,\ell_i} d\Gamma \qquad i = 1, \ldots, d+1 \qquad j = 1, \ldots, n_f$$

Finally, $\mathbf{g_1}$ and $\mathbf{g_2}$ are defined as follows:

$$\mathbf{g_1} = \begin{bmatrix} \mathbf{g_1}_1 \\ \mathbf{g_1}_2 \\ \vdots \\ \mathbf{g_1}_{n_e} \end{bmatrix}_{(d+1)n_e \times 1} \quad \text{with} \quad \mathbf{g_1}_\ell \equiv (g_{1_i}^\ell) = -\int_{T_\ell} \rho_f g \nabla z \cdot \mathbf{w}^{\ell,i} d\Delta \qquad i = 1, \ldots, d+1$$

$$\mathbf{g_2} = \begin{bmatrix} g_{2_1} \\ g_{2_2} \\ \vdots \\ g_{2_{n_e}} \end{bmatrix}_{n_e \times 1} \qquad \text{with} \qquad g_{2_\ell} = \int_{T_\ell} \frac{1}{\rho_f} \left(\rho_{f,0} \eta_T \frac{\partial \theta}{\partial t} + \rho_{f,*} f \right) d\Delta$$

Time integration of (2.12) is performed by a backward finite difference scheme:

$$\begin{bmatrix} A^{t+\Delta t} & -B & C \\ B^T & \frac{1}{\Delta t} D^{t+\Delta t} & 0 \\ C^T & 0 & 0 \end{bmatrix} \begin{bmatrix} \mathbf{u}^{t+\Delta t} \\ \mathbf{p}^{t+\Delta t} \\ \boldsymbol{\psi}^{t+\Delta t} \end{bmatrix} = \begin{bmatrix} \mathbf{g_1}^{t+\Delta t} \\ \mathbf{g_2}^{t+\Delta t} + \frac{1}{\Delta t} D^{t+\Delta t} \mathbf{p}^t \\ \mathbf{0} \end{bmatrix} \tag{2.13}$$

The system of algebraic equations (2.13) is nonlinear because A, D, $\mathbf{g_1}$ and $\mathbf{g_2}$ depend on pressure p through ρ_f. However, the nonlinearity degree in single-phase flow is generally smaller than in multiphase flow with a simple Picard iteration process converging rapidly [Aziz & Settari, 1979]. Denoting by k the non-linear iteration index and setting $\hat{A} = A^{t+\Delta t,k}$, $\hat{D} = D^{t+\Delta t,k}/\Delta t$, $\hat{\mathbf{g_1}} = \mathbf{g_1}^{t+\Delta t,k}$ and $\hat{\mathbf{g_2}} = \mathbf{g_2}^{t+\Delta t,k}$, the iterative scheme is

$$\begin{bmatrix} \hat{A} & -B & C \\ B^T & \hat{D} & 0 \\ C^T & 0 & 0 \end{bmatrix} \begin{bmatrix} \mathbf{u}^{t+\Delta t,k+1} \\ \mathbf{p}^{t+\Delta t,k+1} \\ \boldsymbol{\psi}^{t+\Delta t,k+1} \end{bmatrix} = \begin{bmatrix} \hat{\mathbf{g_1}} \\ \hat{\mathbf{g_2}} + \hat{D}\mathbf{p}^t \\ \mathbf{0} \end{bmatrix} \qquad k = 0, 1, \ldots \tag{2.14}$$

with

$$\begin{bmatrix} \mathbf{u}^{t+\Delta t,0} \\ \mathbf{p}^{t+\Delta t,0} \\ \boldsymbol{\psi}^{t+\Delta t,0} \end{bmatrix} = \begin{bmatrix} \mathbf{u}^t \\ \mathbf{p}^t \\ \boldsymbol{\psi}^t \end{bmatrix}$$

The system (2.14) is generally indefinite with a number of unknowns equal to $(d+2) \times n_e + n_f$. The problem size can be properly reduced. First, $\mathbf{u}^{t+\Delta t,k+1}$ is obtained from the upper system block:

$$\mathbf{u}^{t+\Delta t,k+1} = \hat{A}^{-1} \left(B\mathbf{p}^{t+\Delta t,k+1} - C\boldsymbol{\psi}^{t+\Delta t,k+1} + \hat{\mathbf{g_1}} \right) \tag{2.15}$$

As matrix $\hat{A}$ is block-diagonal, it can be easily inverted. Substitution of (2.15) into the lower equations yields a smaller system:

$$\begin{bmatrix} \hat{D} + B^T \hat{A}^{-1} B & -B^T \hat{A}^{-1} C \\ C^T \hat{A}^{-1} B & -C^T \hat{A}^{-1} C \end{bmatrix} \begin{bmatrix} \mathbf{p}^{t+\Delta t,k+1} \\ \boldsymbol{\psi}^{t+\Delta t,k+1} \end{bmatrix} = \begin{bmatrix} \hat{\mathbf{g_2}} + \hat{D}\mathbf{p}^t - B^T \hat{A}^{-1} \hat{\mathbf{g_1}} \\ -C^T \hat{A}^{-1} \hat{\mathbf{g_1}} \end{bmatrix} \tag{2.16}$$

As $\hat{D}$ and $B^T\hat{A}^{-1}B$ are diagonal, $\mathbf{p}^{t+\Delta t,k+1}$ can be eliminated from the first equation. Setting $H = \hat{D} + B^T\hat{A}^{-1}B$ and $S = \hat{A}^{-1}B$, we obtain:

$$\mathbf{p}^{t+\Delta t,k+1} = H^{-1}\left[S^T\left(C\boldsymbol{\psi}^{t+\Delta t,k+1} - \hat{\mathbf{g_1}}\right) + \hat{\mathbf{g_2}} + \hat{D}\mathbf{p}^t\right] \tag{2.17}$$

Again, matrix H is diagonal and easily invertible. Finally, the solution of the $n_f \times n_f$ system with $\boldsymbol{\psi}^{t+\Delta t,k+1}$ as unknowns is required. Setting $M = \hat{A}^{-1} - SH^{-1}S^T$, this system reads:

$$C^TMC\boldsymbol{\psi}^{t+\Delta t,k+1} = C^TM\hat{\mathbf{g_1}} + C^TSH^{-1}\left(\hat{\mathbf{g_2}} + \hat{D}\mathbf{p}^t\right) \tag{2.18}$$

with C^TMC symmetric and positive definite and with at most $(2d+1)$ nonzero elements per row. The system (2.18) can be effectively solved by a preconditioned conjugate gradient technique. Once $\boldsymbol{\psi}^{t+\Delta t,k+1}$ is computed, $\mathbf{p}^{t+\Delta t,k+1}$ and $\mathbf{u}^{t+\Delta t,k+1}$ can be evaluated using equations (2.17) and (2.15).

2.3.2 Discretization of the heat transfer equation

The heat transfer equation is discretized using a time splitting algorithm. In essence, the method consists of splitting the time derivative in (2.1d) between the convective and conductive parts yielding two partial differential equations, namely:

$$c_{v,M}\frac{\partial\theta}{\partial t} = -\nabla\cdot(c_{v,f}\theta\mathbf{v}) \tag{2.19}$$

and

$$c_{v,M}\frac{\partial\theta}{\partial t} = -\nabla\cdot\mathbf{q} + c_{v,f}\theta_* f \tag{2.20}$$

with (2.19) and (2.20) addressed sequentially using independent discretizations.

In particular, an explicit FV method and the MHFE method are used to approximate the convective term (equation (2.19)) and the conductive (equation (2.20)) term, respectively. This approach can be regarded as a predictor-corrector method: for each time step, the temperature is predicted by n_{conv} explicit FV steps and then used as initial condition for the MHFE step. Two different time step size for convection and conduction, Δt_{conv} and Δt_{cond}, respectively, can be used. The stability of the explicit convective step is governed by a Courant-Friedrichs-Lewy (CFL) constraint [Liu, 1993; Mazzia *et al.*, 2000], with the CFL number defined on each element as:

$$\mathrm{CFL} = \Delta t_{conv}\sup\frac{\overline{T}_\ell}{|T_\ell|}\sup\left|\frac{d\mathbf{F}}{d\theta}\right| \tag{2.21}$$

with $\overline{T}_\ell$ the perimeter ($d=2$) or the surface area ($d=3$) of T_ℓ and $\mathbf{F} = c_{v,f}\theta\mathbf{v}$. On the other hand, no stability restriction exists for Δt_{cond} assuming $\Delta t_{cond} = n_{conv}\Delta t_{conv}$.

FV discretization

Let consider the same triangulation $\mathcal{T}$ defined for the flow problem. The discretization of (2.19) follows the FV scheme on unstructured triangular grid developed by Durlofsky *et al.* [1992] and then modified by Liu [1993].

At first, the integral form of equation (2.19) is written on each element T_ℓ:

$$\int_{T_\ell} c_{v,M} \frac{\partial \theta}{\partial t} d\Delta = -\int_{T_\ell} \nabla \cdot \mathbf{F}(\theta) d\Delta \tag{2.22}$$

The temperature $\theta(\mathbf{x}, t)$ is approximated by constant element-wise function $h_\ell(\mathbf{x})$:

$$\theta(\mathbf{x}, t) \simeq \sum_{\ell=1}^{n_e} \theta_\ell(t) h_\ell(\mathbf{x}) \qquad \ell = 1, \ldots, n_e \tag{2.23}$$

with

$$\theta_\ell(t) = \frac{1}{|T_\ell|} \int_{T_\ell} \theta(\mathbf{x}, t) d\Delta \tag{2.24}$$

the mean temperature value in T_ℓ and h_ℓ are the function defined in (2.4). Using divergence theorem to the right-hand side of (2.22) and recalling (2.24), yields:

$$c_{v,M} \frac{\partial \theta_\ell}{\partial t} = -\frac{1}{|T_\ell|} \sum_{j=1}^{d+1} \int_{e^{\ell,\ell_j}} \mathbf{F}(\theta) \cdot \mathbf{n}^{\ell,\ell_j} d\Gamma \qquad \ell = 1, \ldots, n_e \tag{2.25}$$

The integrals above are approximated introducing the intercell flux H^{ℓ,ℓ_j}:

$$c_{v,M} \frac{\partial \theta_\ell}{\partial t} = -\frac{1}{|T_\ell|} \sum_{j=1}^{d+1} H^{\ell,\ell_j} \qquad \ell = 1, \ldots, n_e \tag{2.26}$$

where $H^{\ell,\ell_j} = H(\theta_\ell^{\ell,\ell_j}, \theta_{\ell_j}^{\ell_j,\ell}, \mathbf{n}^{\ell,\ell_j}) \left| e^{\ell,\ell_j} \right|$ depends on the cell averaged values of the temperature $\theta_\ell^{\ell,\ell_j}$ and $\theta_{\ell_j}^{\ell_j,\ell}$ evaluated on the left and the right sides of e^{ℓ,ℓ_j}, respectively, and the elemental edge length or area $\left| e^{\ell,\ell_j} \right|$.

To get a second order approximation in space, $\theta_\ell^{\ell,\ell_j}$ and $\theta_{\ell_j}^{\ell_j,\ell}$ are linearly reconstructed component-wise from the cell-averaged data:

$$\theta_\ell^{\ell,\ell_j} = \theta_\ell + \mathbf{r}_\ell^{\ell,\ell_j} \cdot \nabla(L_\ell) \tag{2.27}$$

$$\theta_{\ell_j}^{\ell_j,\ell} = \theta_{\ell_j} + \mathbf{r}_{\ell_j}^{\ell_j,\ell} \cdot \nabla(L_{\ell_j}) \tag{2.28}$$

where $\mathbf{r}_r^{r,s}$ is the vector from the centroid of cell T_r to the centroid of the face $e^{r,s}$ and $\nabla(L_r)$ is the gradient of a linear polynomial L_r defined on T_r, $(r, s) = (\ell, \ell_j), (\ell_j, \ell)$. This guarantees that a linear θ is reproduced exactly, but overshoots and undershoots at

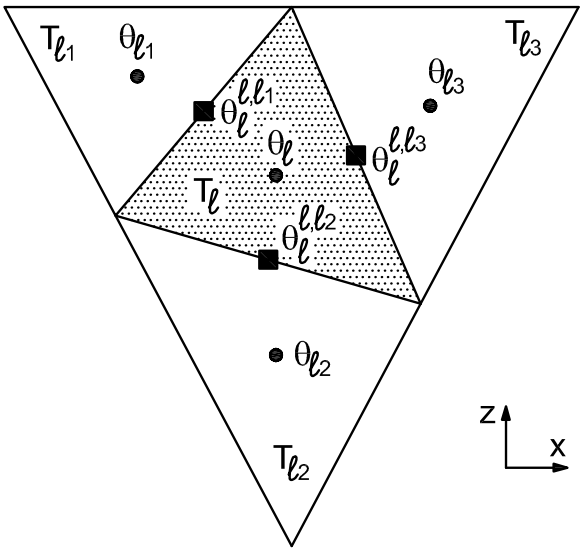

Figure 2.4: Triangular grid.

the centroids of the tetrahedra faces may be introduced. Non-linear correction factors, called limiters, are used to avoid these numerical oscillations and satisfy a local maximum principle. These limiters must be designed so as to preserve the global second order accuracy, i.e. they have to correct (2.27)-(2.28) acting locally only and in case of sharp gradients. A careful definition of this limiting function is crucial to exploit fully the method.

In the two-dimensional case, the reconstruction and corresponding limiter are defined as follows [Liu, 1993]. In each triangle T_ℓ three linear functions are built by interpolating the temperature values at its centroid $\mathbf{x}_\ell$ and at the centroids $\mathbf{x}_{\ell_j}$ of its three neighbours T_{ℓ_j}, $j = 1, \ldots, 3$ (see Figure 2.4), namely:

- L_ℓ^1 is the linear interpolant of $(\mathbf{x}_\ell, \theta_\ell)$, $(\mathbf{x}_{\ell_1}, \theta_{\ell_1})$, and $(\mathbf{x}_{\ell_2}, \theta_{\ell_2})$;
- L_ℓ^2 is the linear interpolant of $(\mathbf{x}_\ell, \theta_\ell)$, $(\mathbf{x}_{\ell_2}, \theta_{\ell_2})$, and $(\mathbf{x}_{\ell_3}, \theta_{\ell_3})$;
- L_ℓ^3 is the linear interpolant of $(\mathbf{x}_\ell, \theta_\ell)$, $(\mathbf{x}_{\ell_3}, \theta_{\ell_3})$, and $(\mathbf{x}_{\ell_1}, \theta_{\ell_1})$.

The euclidean norm of the gradient of each L_ℓ^j is computed:

$$\left|\nabla L_\ell^j\right| = \sqrt{\left(\frac{\partial L_\ell^j}{\partial x}\right)^2 + \left(\frac{\partial L_\ell^j}{\partial y}\right)^2} \qquad j = 1, 2, 3.$$

Starting from the function L_ℓ^j with maximum gradient toward the one with minimum

gradient, the first j is selected such that

$$\begin{aligned} &L_\ell^j(\mathbf{x}^{\ell,\ell_1}) \text{ is between } \theta_\ell \text{ and } \theta_{\ell_1} \\ &L_\ell^j(\mathbf{x}^{\ell,\ell_2}) \text{ is between } \theta_\ell \text{ and } \theta_{\ell_2} \\ &L_\ell^j(\mathbf{x}^{\ell,\ell_3}) \text{ is between } \theta_\ell \text{ and } \theta_{\ell_3}, \end{aligned} \tag{2.29}$$

where $\mathbf{x}^{\ell,\ell_j}$ is the centroid of the edge e^{ℓ,ℓ_j} $(j = 1,\ldots,3)$. If no L_ℓ^j satisfies (2.29) the local upper bound UB_ℓ and the local lower bound LB_ℓ of T_ℓ, defined as the maximum and the minimum temperature values, respectively, at the centroids of triangles sharing at least one point with T_ℓ, are determined. Hence, starting again from L_ℓ^j with the largest gradient, the first j such that L_ℓ^j satifies

$$\begin{aligned} UB_\ell &\geq \max\left(L_\ell^j(\mathbf{x}^{\ell,\ell_1}), L_\ell^j(\mathbf{x}^{\ell,\ell_2}), L_\ell^j(\mathbf{x}^{\ell,\ell_3})\right) \\ LB_\ell &\leq \min\left(L_\ell^j(\mathbf{x}^{\ell,\ell_1}), L_\ell^j(\mathbf{x}^{\ell,\ell_2}), L_\ell^j(\mathbf{x}^{\ell,\ell_3})\right). \end{aligned} \tag{2.30}$$

is chosen. If no L_ℓ^j satisfies the inequalities (2.30), $L_\ell = \theta_\ell$ is assumed, i.e. a first order reconstruction is used.

In a three-dimensional setting, a linear interpolant based on a least-square approximation of the centroids values of the reference tetrathedron T_ℓ and its four neighbours combined with the limiter described in Barth & Jespersen [1989] is adopted as suggested by Mazzia & Putti [2005], because the extension of the method above appears inadequate to obtain the desired accuracy when using tetrahedra. This approach requires the definition of one interpolant only accounting for all information available in T_ℓ and its neighbours T_{ℓ_j} $(j = 1,\ldots,4)$. The least-square method minimizes the functional

$$S(L_\ell) = \sum_{v\in\{\ell,\ell_1,\ell_2,\ell_3,\ell_4\}} (L_\ell(\mathbf{x}_v) - \theta_v)^2 \tag{2.31}$$

where the gradient of L_ℓ is the slope of the resulting hyperplane. The slope limiter is applied computing [Barth & Jespersen, 1989]:

$$\theta_\ell^{\ell,\ell_j} = \theta_\ell + \Phi_\ell \mathbf{r}_\ell^{\ell,\ell_j} \cdot \nabla(L_\ell) \qquad j = 1,\ldots,4 \tag{2.32}$$

where $\Phi_\ell = \min\left(\Phi_{\ell_1}, \Phi_{\ell_2}, \Phi_{\ell_3}, \Phi_{\ell_4}\right)$ and

$$\Phi_{\ell_j} = \begin{cases} 1 & \text{if } (\theta_\ell^{\ell,\ell_j})^{old} - \theta_\ell = 0, \\ \min\left(1, \dfrac{\theta_\ell^{max} - \theta_\ell}{(\theta_\ell^{\ell,\ell_j})^{old} - \theta_\ell}\right) & \text{if } (\theta_\ell^{\ell,\ell_j})^{old} - \theta_\ell > 0, \\ \max\left(1, \dfrac{\theta_\ell^{min} - \theta_\ell}{(\theta_\ell^{\ell,\ell_j})^{old} - \theta_\ell}\right) & \text{if } (\theta_\ell^{\ell,\ell_j})^{old} - \theta_\ell < 0. \end{cases} \tag{2.33}$$

In the previous formula, $\theta_l^{min} = \min\left(\theta_\ell, \min_j \theta_\ell^{\ell,\ell_j}\right)$ and $\theta_\ell^{max} = \max\left(\theta_\ell, \max_j \theta_\ell^{\ell,\ell_j}\right)$.

Once L_ℓ is computed for every T_ℓ, the reconstructed left $\theta_\ell^{\ell,\ell_j}$ and right $\theta_{\ell_j}^{\ell_j,\ell}$ temperature values at the centroid of each elemental edge $e^{\ell,\ell_j} \equiv e^{\ell_j,\ell}$ represent the boundary conditions of a local Riemann problem [e.g., Toro , 1999]. Hence, the second order semidiscrete approximation to (2.22) reads:

$$c_{v,M}\frac{\partial \theta_\ell}{\partial t} = -\frac{1}{|T_\ell|}\sum_{j=1}^{d+1} H(\theta_\ell^{\ell,\ell_j}, \theta_{\ell_j}^{\ell_j,\ell}, \mathbf{n}^{\ell,\ell_j})\left|e^{\ell,\ell_j}\right| \qquad \ell = 1,\ldots,n_e \tag{2.34}$$

with

$$H(\theta_\ell^{\ell,\ell_j}, \theta_{\ell_j}^{\ell_j,\ell}, \mathbf{n}^{\ell,\ell_j}) = \begin{cases} \mathbf{F}(\theta_\ell^{\ell,\ell_j})\cdot\mathbf{n}^{\ell,\ell_j} & \text{if } \mathbf{v}\cdot\mathbf{n}^{\ell,\ell_j} \geq 0 \\ \mathbf{F}(\theta_{\ell_j}^{\ell_j,\ell})\cdot\mathbf{n}^{\ell,\ell_j} & \text{if } \mathbf{v}\cdot\mathbf{n}^{\ell,\ell_j} < 0 \end{cases} \tag{2.35}$$

Time integration between t and $t+\Delta t_{conv}$ of (2.34) is performed explicitly by means of a two-stage second-order Runge-Kutta method (Heun formula):

$$\begin{aligned} &\underline{\text{stage 1}} \qquad \theta_\ell^1 &&= \theta_\ell^t - \Delta t E_\ell(\mathbf{x},\theta^t) && \ell = 1,\ldots,n_e \\ &\underline{\text{stage 2}} \quad \theta_\ell^{t+\Delta t_{conv}} &&= \tfrac{1}{2}\theta_\ell^t + \tfrac{1}{2}(\theta_\ell^1 - \Delta t E_\ell(\mathbf{x},\theta_\ell^1)) && \ell = 1,\ldots,n_e \end{aligned} \tag{2.36}$$

where E_ℓ is defined as

$$E_\ell(\mathbf{x},\theta) = \frac{1}{|T_\ell|}\sum_{j=1}^{d+1} H(\theta_\ell^{\ell,\ell_j}, \theta_{\ell_j}^{\ell_j,\ell}, \mathbf{n}^{\ell,\ell_j})\left|e^{\ell,\ell_j}\right|. \tag{2.37}$$

MHFE dicretization

The MHFE method is used to discretize equation (2.20). The temperature θ is approximated by (2.23), while the elemental heat flux $\mathbf{q}^\ell$ and the temperature on the elemental edges τ, i.e. the Lagrange multiplier, are expressed as:

$$\mathbf{q}^\ell(\mathbf{x},t) \simeq \sum_{j=1}^{d+1} q^{\ell,\ell_j}(t)\mathbf{w}^{\ell,j}(\mathbf{x}) \qquad \ell = 1,\ldots,n_e \tag{2.38}$$

$$\tau(\mathbf{x},t) \simeq \sum_{j=1}^{n_f} \tau_j(t)\varphi_j(\mathbf{x}) \tag{2.39}$$

where $\mathbf{w}^{\ell,j}$ and φ_j are the the basis functions used in (2.5) and (2.8), q^{ℓ,ℓ_j} is the the normal heat flux across element edge e^{ℓ,ℓ_j} of T_j and τ_j is the temperature on e_j.

The MHFE method applied to (2.20) produces the following system of linear equations:

$$\int_{T_\ell} \mathbf{\Lambda}^{-1}\mathbf{q}\cdot\mathbf{w}^{\ell,i}d\Delta - \int_{T_\ell}\theta\nabla\cdot\mathbf{w}^{\ell,i}d\Delta + \int_{e^{\ell,\ell_i}}\tau\mathbf{w}^{\ell,i}\cdot\mathbf{n}^{\ell}d\Gamma = 0 \tag{2.40a}$$

$$\int_{T_\ell}\nabla\cdot\mathbf{q}d\Delta + \int_{T_\ell} c_{v,M}\frac{\partial\theta}{\partial t}d\Delta = \int_{T_\ell} c_{v,f}\theta_* f d\Delta \tag{2.40b}$$

$$\int_{e_j}\mathbf{q}^{\ell_L}\cdot\mathbf{n}^{\ell_L,\ell_R}d\Gamma + \int_{e_j}\mathbf{q}^{\ell_R}\cdot\mathbf{n}^{\ell_R,\ell_L}d\Gamma = 0 \tag{2.40c}$$

with $\ell = 1,\ldots,n_e$, $i = 1,\ldots,d+1$ and $j = 1,\ldots,n_f$.

Substitution of (2.23), (2.38) and (2.39) in (2.40a), (2.40b) and (2.40c) leads to the following set of nonlinear differential-algebraic equations:

$$\begin{array}{rcrcrcl} E\mathbf{q} & - & B\boldsymbol{\theta} & + & C\boldsymbol{\tau} & = & \mathbf{0} \\ B^T\mathbf{q} & + & F\dot{\boldsymbol{\theta}} & & & = & \mathbf{t_2} \\ C^T\mathbf{q} & & & & & = & \mathbf{0} \end{array} \tag{2.41}$$

where the unknowns vectors $\mathbf{q}$, $\boldsymbol{\theta}$ and $\boldsymbol{\tau}$ are:

$$\mathbf{q} = \begin{bmatrix} \left\{ \begin{array}{c} q^{1,1_1} \\ \vdots \\ q^{1,1_{d+1}} \end{array} \right\} \\ \left\{ \begin{array}{c} q^{2,2_1} \\ \vdots \\ q^{2,2_{d+1}} \end{array} \right\} \\ \vdots \\ \left\{ \begin{array}{c} q^{n_e,n_{e_1}} \\ \vdots \\ q^{n_e,n_{e_{d+1}}} \end{array} \right\} \end{bmatrix} \qquad \boldsymbol{\theta} = \begin{bmatrix} \theta_1 \\ \theta_2 \\ \vdots \\ \theta_{n_e} \end{bmatrix} \qquad \boldsymbol{\tau} = \begin{bmatrix} \tau_1 \\ \tau_2 \\ \vdots \\ \tau_{n_f} \end{bmatrix}$$

E, F and $\mathbf{t_2}$ have the same pattern as A, D and $\mathbf{g_2}$ respectively, and their coefficients expressions are:

$$
\begin{aligned}
E_\ell \equiv (e^\ell_{ij}) &= \int_{T_\ell} (\mathbf{\Lambda}^\ell)^{-1} \mathbf{w}^{\ell,j} \cdot \mathbf{w}^{\ell,i} d\Delta \qquad i,j = 1,\ldots,d+1 \\
f_\ell &= \int_{T_\ell} c_{v,M} d\Delta \\
t_{2\ell} &= \int_{T_\ell} c_{v,f} \theta_* d\Delta
\end{aligned}
$$

The time marching scheme and the developments leading to the final system of algebraic equations are the same as in Section 2.3.1 for the fluid flow problem.

Boundary conditions

The time-splitting approach requires a careful implementation of the boundary conditions. To better describe how the boundary conditions are handled inflow and outflow boundaries are analyzed separately.

Inflow boundaries are characterized by Darcy's velocity $\mathbf{v}$ pointing inward the domain. Cauchy boundary conditions can represent a fluid flow at a prescribed temperature. The implementation of these boundary conditions is obtained by prescribing Dirichlet-type boundary conditions in the convective step and Neumann-type boundary conditions in the conductive step. For example, inflow at a fixed temperature θ_1 is specified as:

$$
\begin{aligned}
c_{v,f}\theta \mathbf{v}\cdot\mathbf{n} &= c_{v,f}\theta_1 \mathbf{v}\cdot\mathbf{n} \implies \text{i.e. Dirichlet b.c. } \theta = \theta_1 \text{ for the convective step} \\
\mathbf{q}\cdot\mathbf{n} &= 0 \implies \text{i.e. zero Neumann flux for the conductive step}
\end{aligned}
$$

Outflow boundaries are characterized by outgoing velocities, zero Neumann fluxes are imposed in the conduction equation, as the outgoing convective flux is governed only by the velocity field.

Along fluid impermeable boundaries, either Dirichlet or Neumann can be used, the former prescribed both in the convective and conductive steps and the latter only on the conduction equation.

2.3.3 The Picard method

The iteratively coupled method for the solution of the nonlinear system of equations proceeds as follows. To advance in time from t to $t+\Delta t$, at the $(k+1)-th$ iteration the flow equation is first solved for $\mathbf{p}^{t+\Delta t,k+1}$ and $\mathbf{u}^{t+\Delta t,k+1}$, freezing the values of the temperature $\boldsymbol{\theta}^{t+\Delta t,k}$ at the previous iteration. Employing these updated values of pressure and velocity, the heat transfer equation is then solved for $\boldsymbol{\theta}^{t+\Delta t,k+1}$. The procedure is repeated until convergence is achieved. The algorithm is summarized in Table 2.1.

DO $k = 1, 2, \ldots$ UNTIL CONVERGENCE

- **Flow equation**

$$H = \hat{D} + B^T \hat{A}^{-1} B$$
$$S = \hat{A}^{-1} B$$
$$M = \hat{A}^{-1} - S H^{-1} S^T$$
$$C^T M C \boldsymbol{\psi}^{t+\Delta t,k+1} = C^T M \hat{\mathbf{g_1}} + C^T S H^{-1} \left(\hat{\mathbf{g_2}} + \hat{D} \mathbf{p}^t \right)$$
$$\mathbf{p}^{t+\Delta t,k+1} = H^{-1} \left[S^T \left(C \boldsymbol{\psi}^{t+\Delta t,k+1} - \hat{\mathbf{g_1}} \right) + \hat{\mathbf{g_2}} + \hat{D} \mathbf{p}^t \right]$$
$$\mathbf{u}^{t+\Delta t,k+1} = \hat{A}^{-1} \left(B \mathbf{p}^{t+\Delta t,k+1} - C \boldsymbol{\psi}^{t+\Delta t,k+1} + \hat{\mathbf{g_1}} \right)$$

- **Heat transfer equation**

Convective step

DO $r = 1, \ldots, n_{conv}$

$$\hat{t} = t + (r-1)\Delta t_{conv}$$

DO $\ell = 1, \ldots, n_e$

$$\theta_\ell^1 = \theta_\ell^{\hat{t}} - \Delta t_{conv} E_\ell(\mathbf{x}, \theta^{\hat{t}})$$

END DO

DO $\ell = 1, \ldots, n_e$

$$\theta_\ell^{\hat{t}+\Delta t_{conv}} = \frac{1}{2}\theta_\ell^{\hat{t}} + \frac{1}{2}(\theta_\ell^1 - \Delta t_{conv} E_\ell(\mathbf{x}, \theta_\ell^1))$$

END DO

END DO

Conductive step

$$H = \hat{F} + B^T \hat{E}^{-1} B$$
$$S = \hat{E}^{-1} B$$
$$M = \hat{E}^{-1} - S H^{-1} S^T$$
$$C^T M C \boldsymbol{\tau}^{t+\Delta t,k+1} = C^T S H^{-1} \left(\hat{\mathbf{t_2}} + \hat{F} \boldsymbol{\theta}^{t+n_{conv}\Delta t_{conv}} \right)$$
$$\boldsymbol{\theta}^{t+\Delta t,k+1} = H^{-1} \left(S^T C \boldsymbol{\tau}^{t+\Delta t,k+1} + \hat{\mathbf{t_2}} + \hat{F} \boldsymbol{\theta}^{t+n_{conv}\Delta t_{conv}} \right)$$

END DO

Table 2.1: Picard iteration algorithm.

Convergence is achieved when:

$$\begin{aligned} \|\mathbf{p}^{t+\Delta t,k+1} - \mathbf{p}^{t+\Delta t,k}\|_2 &\leq \text{tol}_p \\ \|\boldsymbol{\theta}^{t+\Delta t,k+1} - \boldsymbol{\theta}^{t+\Delta t,k}\|_2 &\leq \text{tol}_\theta \end{aligned} \tag{2.42}$$

where tol_p and tol_θ are two fixed tolerances. In case convergence is not achieved, Δt is reduced using an empirical algorithm already tested in several problems [e.g., D'Haese *et al.*, 2007]. Given Δt_{cond} as selected by this procedure, the value of n_{conv} is chosen so that the CFL constraint is satisfied (2.21).

2.4 Numerical results

2.4.1 Elder's problem

The Elder problem is an example of free convection, where the fluid flow is driven by density differences only. Elder [1967a,b] presented experimental and numerical studies concerning the thermal convection produced by heating a partion of the basis of a porous layer. The original experiment, called the *short-heater problem*, was performed in a Hele-Shaw cell, which provides a laboratoy analogue for flow in porous media. Elder conducted these studies mainly to verify the finite difference model he developed for the two-dimensional simulation of thermal-driven convection and provided his results graphically for the temperature and stream-function fields. Because of its complexity, Elder's problem is tipically used as a bechmark in flow-transport problems.

The Elder problem consists of a two-dimensional water-saturated rectangular porous volume (Figure 2.5). Hydrostatic pressure and uniform temperature are the initial condition. A specified pressure of 0 Pa (atmospheric conditions) is imposed at the upper corners of the region and all boundaries are impervious to fluid flow. A source of heat at constant temperature θ_B is applied at part of the bottom boundary, while the temperature at the top boundary is kept constant. All remaining boundary portions are considered adiabatic (insulated).

The Elder [1967b] formulation was in terms of dimensionless variables, selecting as units of length, temperature and velocity the height of the box, H, the excess of temperature of the heated region, $\Delta\theta = \theta_B - \theta_{in}$, and $\lambda_M c_{v,M}^{-1} H^{-1}$, respectively. Figure (2.6) shows the contoured temperature fields he obtained at four dimensionless time $\tilde{t}_j$ $(j = 1, \ldots, 4)$. Note that a vertical exaggeration of a factor two is used in all these figures.

The dimensional parameters used in the simulation are taken from Kipp [1997] (Table 2.2). The domain is discretized with 2000 regular triangular elements with a uniform

Symbol	Quantity	Value	Unit
B	length	4	m
H	height	1	m
ϕ	porosity	0.10	-
k	permeability	9.084×10^{-9}	m^2
S_s	elastic storage	0	m^{-1}
λ_s	thermal conductivity of solid	2.0	W m^{-1} $°C^{-1}$
$c_{v,s}$	heat capacity of solid	2.0×10^6	J m^{-3} $°C^{-1}$
ρ_0	water Density	1000	kg m^{-3}
μ_0	water viscosity	0.001	Pa s
α_L	longitudinal thermodispersivity	0	m
α_T	transverse thermodispersivity	0	m
$c_{v,f}$	heat capacity of the fluid	4.182×10^6	J m^{-3} $°C^{-1}$
λ_f	thermal conductivity of the fluid	0.6	W m^{-1} $°C^{-1}$
β	water compressibility	0	Pa^{-1}
β'	Thermal expansion coefficient of the fluid	1.5×10^{-4}	$°C^{-1}$
α	viscosity coefficient	-0.0233	$°C^{-1}$
θ_{in}	initial temperature	10	°C
θ_B	temperature at the bottom boundary	20	°C
θ_T	temperature at the top boundary	10	°C

Table 2.2: Simulation parameters for the Elder problem.

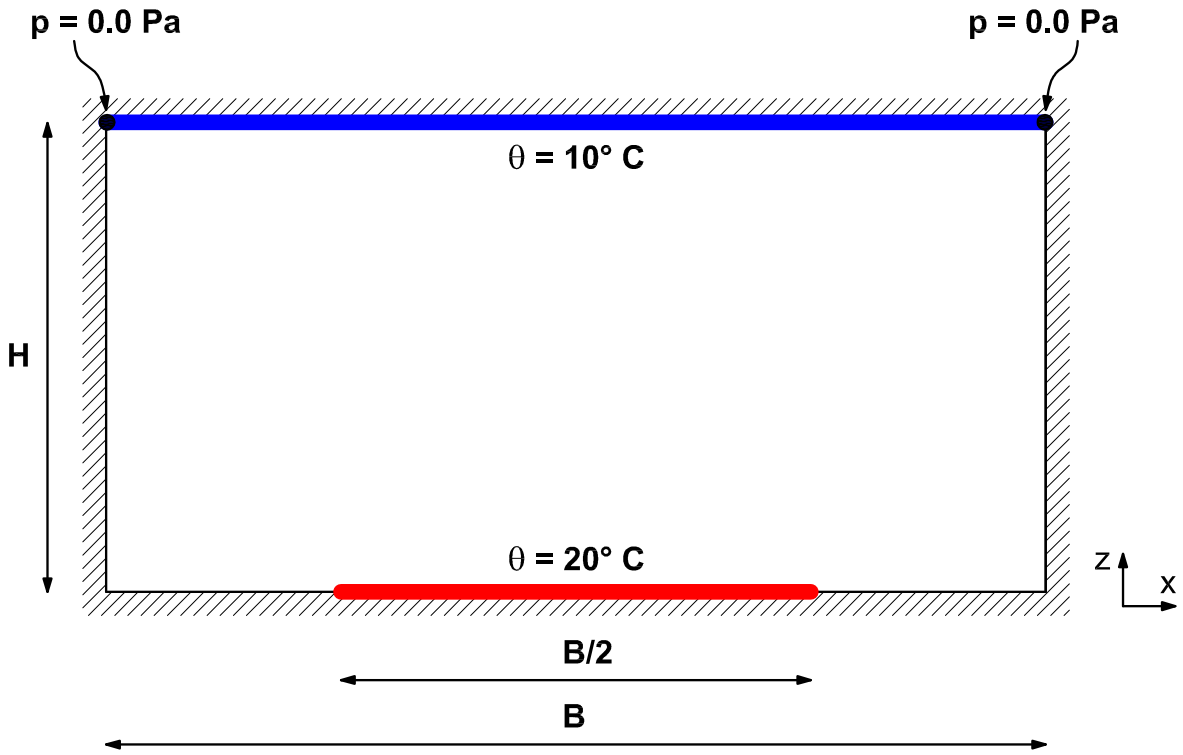

Figure 2.5: Definition of Elder's problem.

node spacing $\Delta x = 0.08$ m in the horizontal direction and $\Delta z = 0.05$ m in the vertical direction. A constant time step of 500 s is used for the conductive step while the convective one is imposed by condition (2.21) assuming CFL = 0.3. The dimensionless temperature and the velocity fields as simulated by MHFE and GMMs coupled models are reported in Figure (2.7)-(2.10). At first, heat propagates into the domain by conduction from the bottom boundary, inducing a decrease in water density and a consequent circulating flow. The fluid motion develops a set of eddies forming at the two ends of the heated zone, because of the larger density gradient. Small eddies of reverse circulation are associated with the end eddies, followed by a further set of eddies growing near the ends. The solution is in good agreement with both Elder's and other similar results available in the literature [e.g. Diersch & Kolditz, 1998]. Moreover, it does not suffer from numerical oscillations without introducing a significant numerical diffusion, as tipically done by more conventional upwind discretization. The solution does not seem to be significantly influenced by the computational grid.

The three-dimensional analogue of Elder's problem consists of a porous box with a square base of side 4 m and height 1 m [Diersch & Kolditz, 1998]. The box has the same cross-section as the two-dimensional problem. Boundary and initial conditions are the

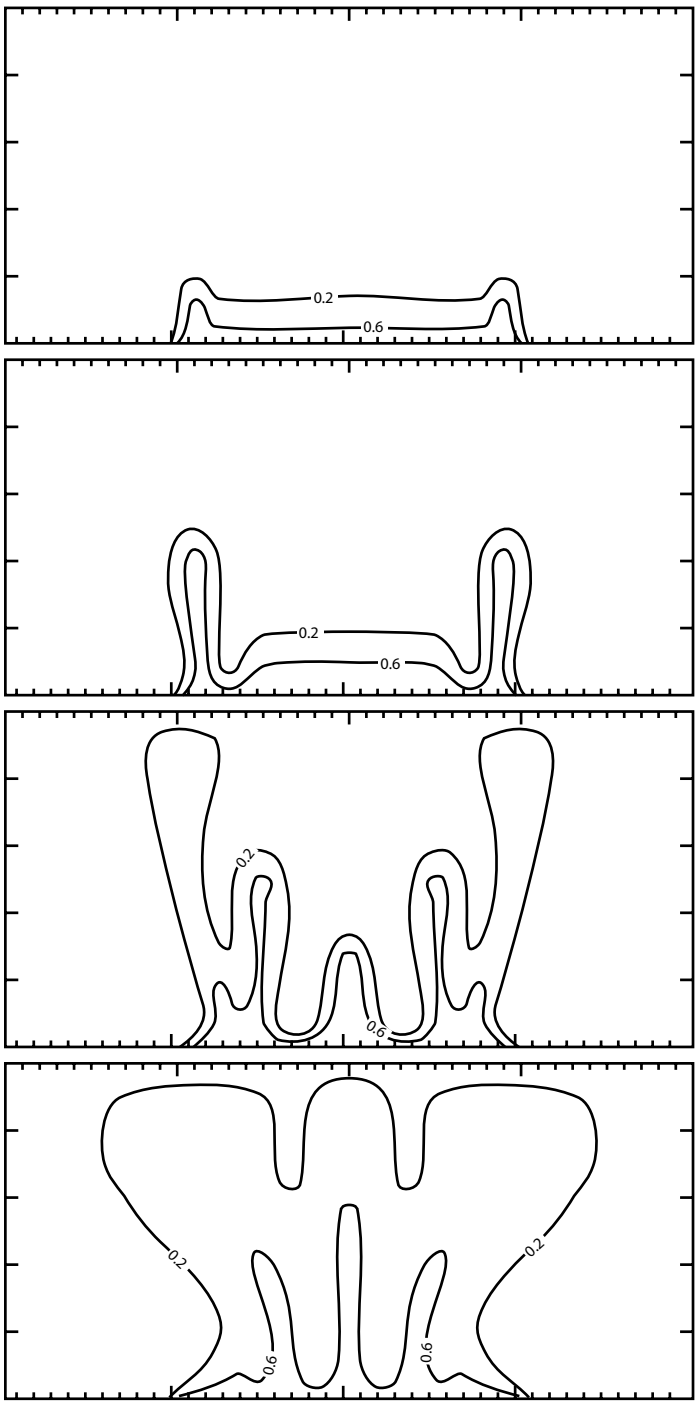

Figure 2.6: Dimensionless temperature at four dimensionless time values for Elder's problem (from Elder [1967b]).

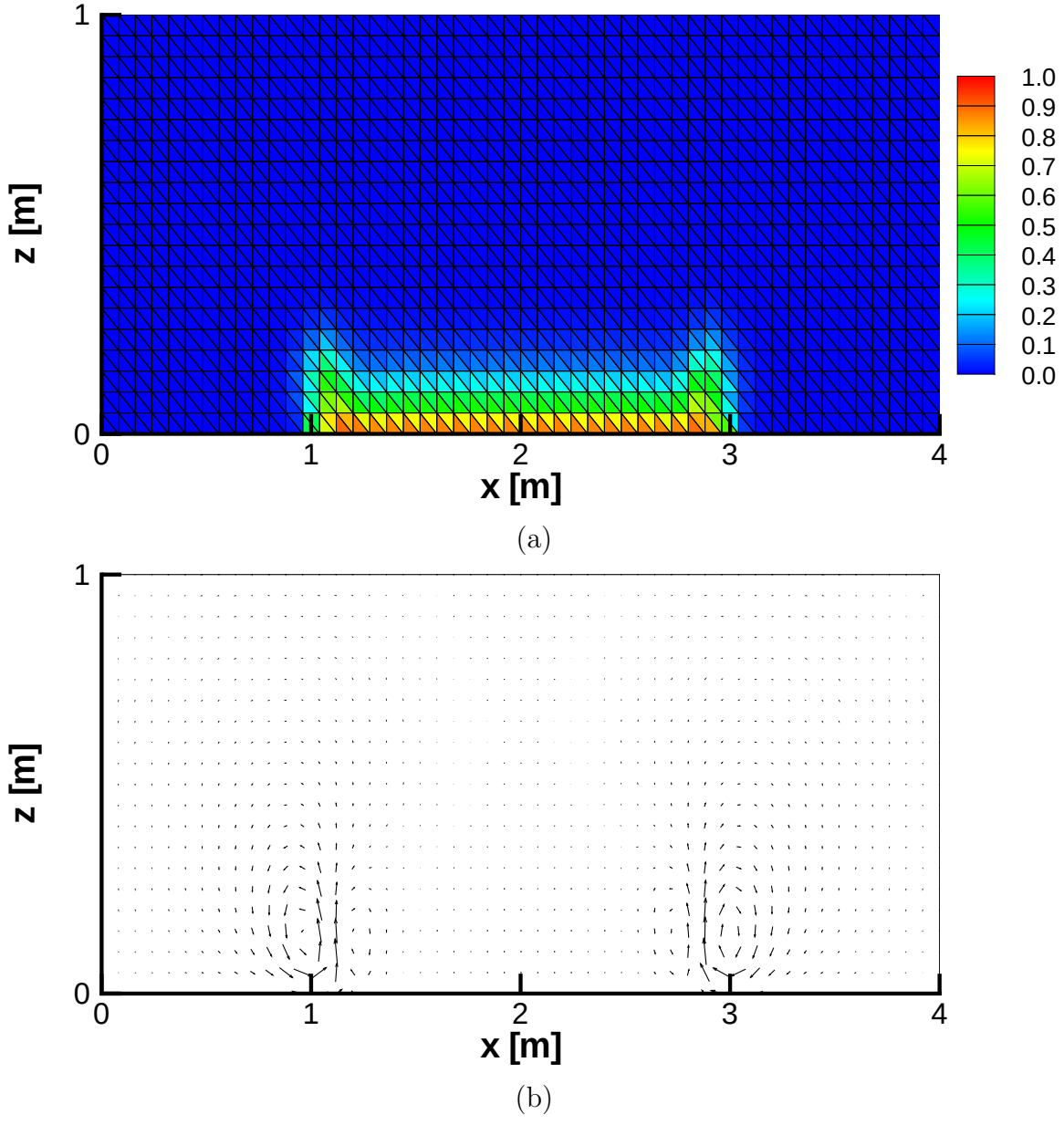

Figure 2.7: Elder's problem: dimensionless temperature $\tilde{\theta}$ (a) and velocity field (b) at time $\tilde{t}_1$. Temperature varies between $\tilde{\theta} = 0$ ($\theta = 10°\text{C}$) and $\tilde{\theta} = 1$ ($\theta = 20°\text{C}$).

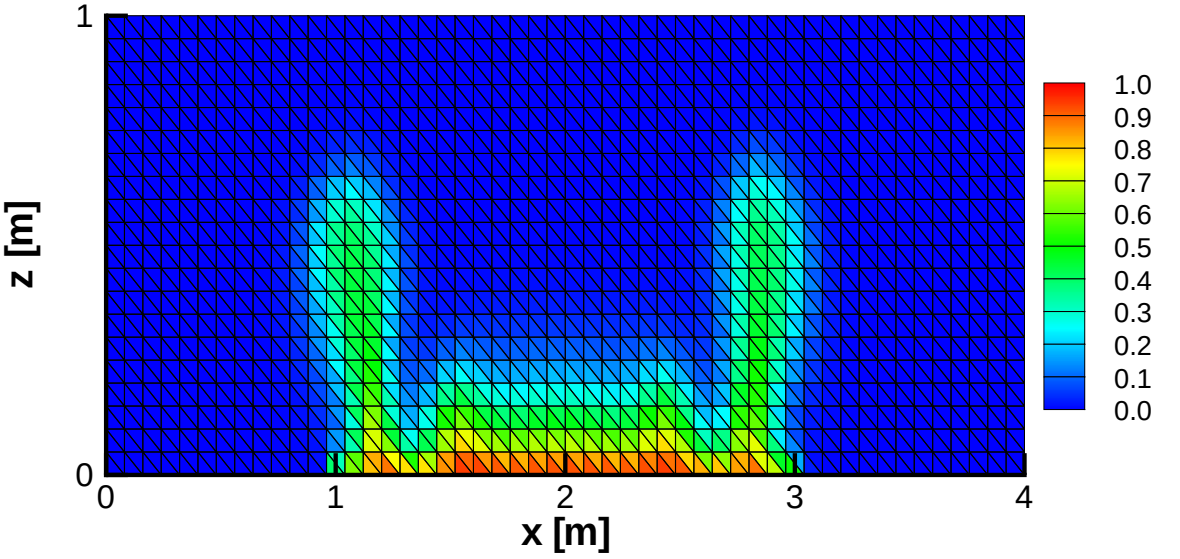

(a)

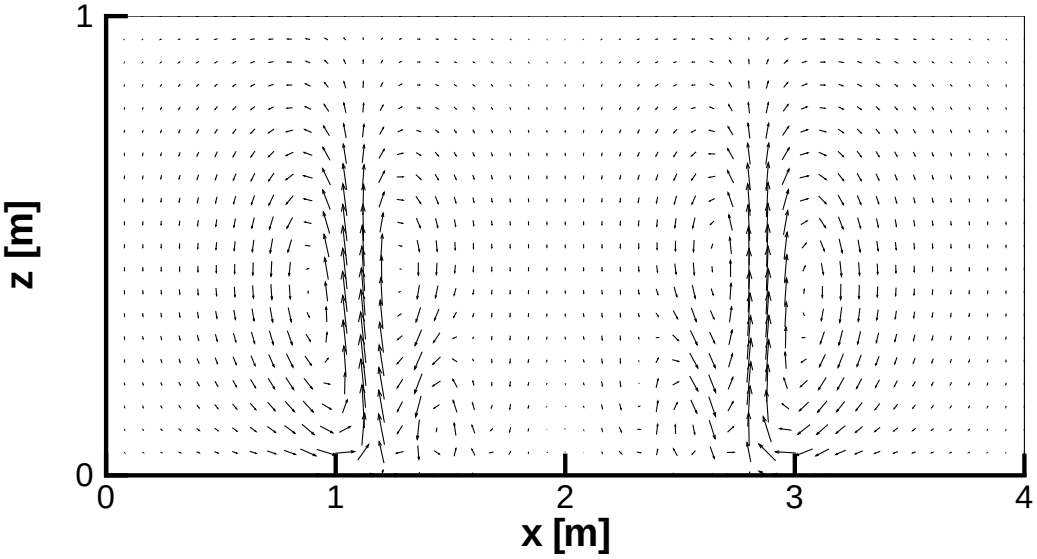

(b)

Figure 2.8: The same as Figure 2.7 at time $\tilde{t}_2$.

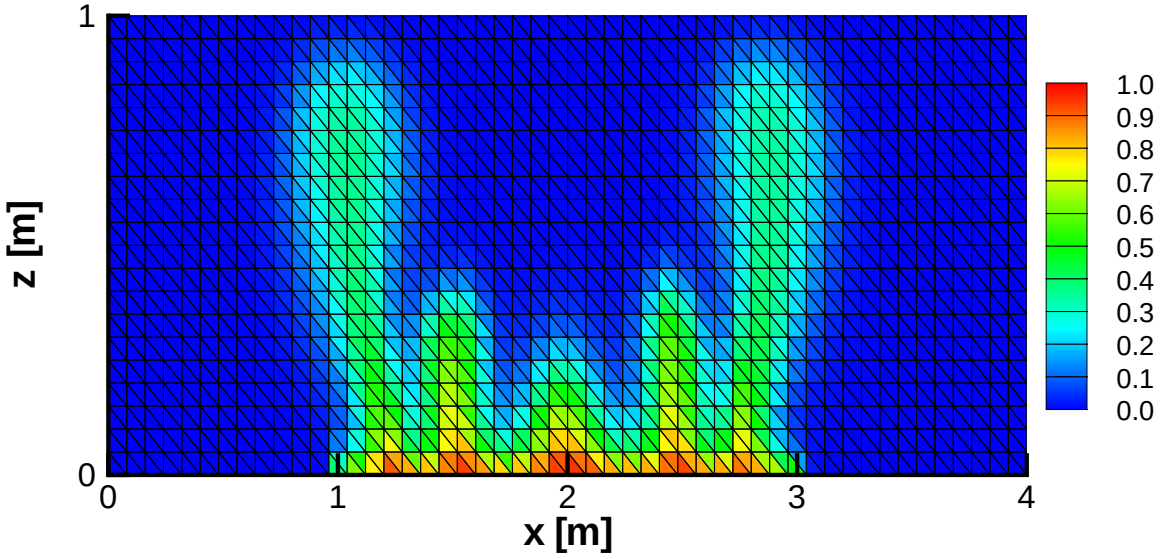

(a)

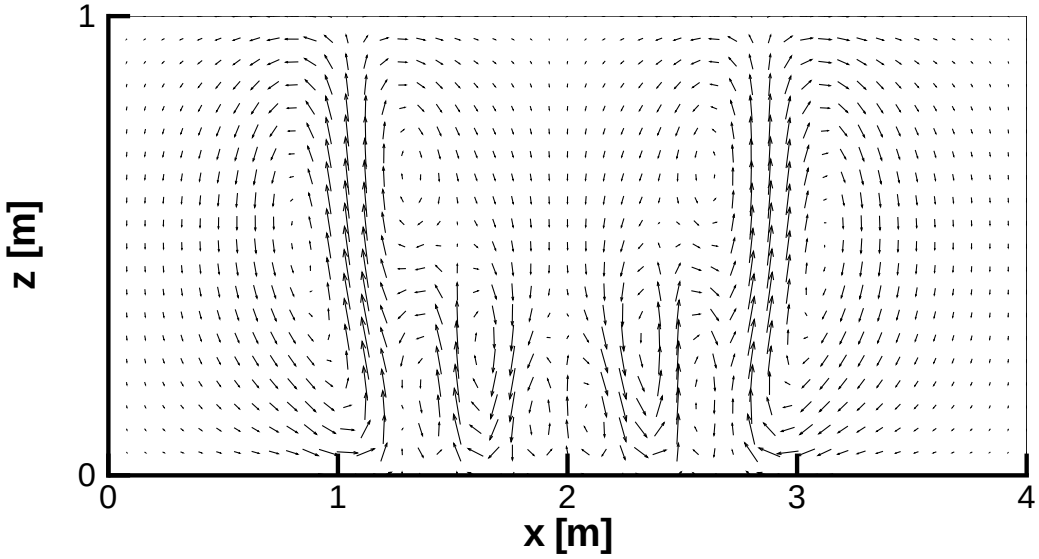

(b)

Figure 2.9: The same as Figure 2.7 at time $\tilde{t}_3$.

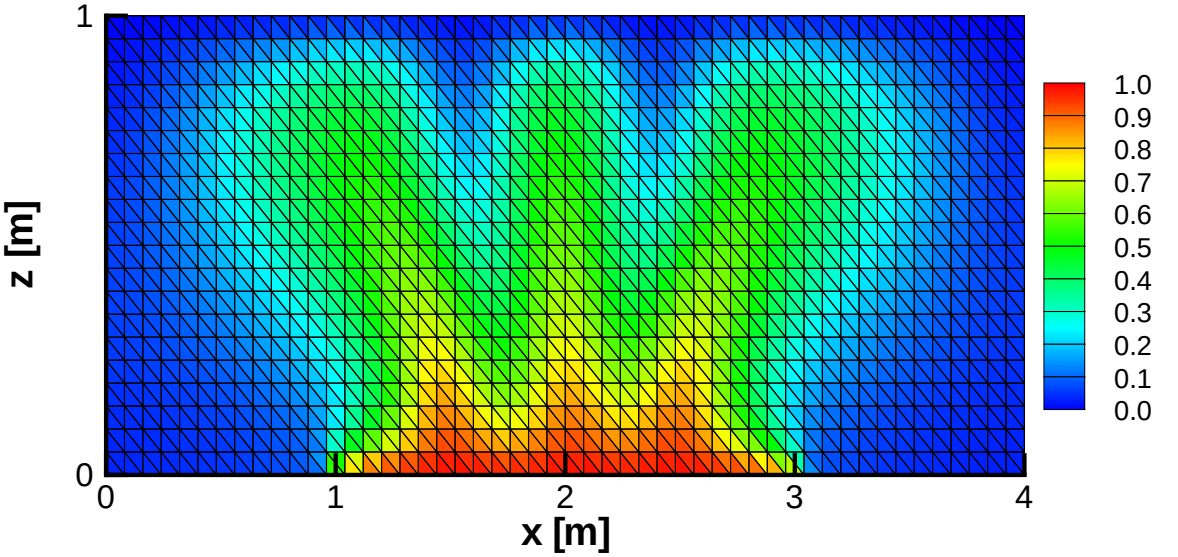

(a)

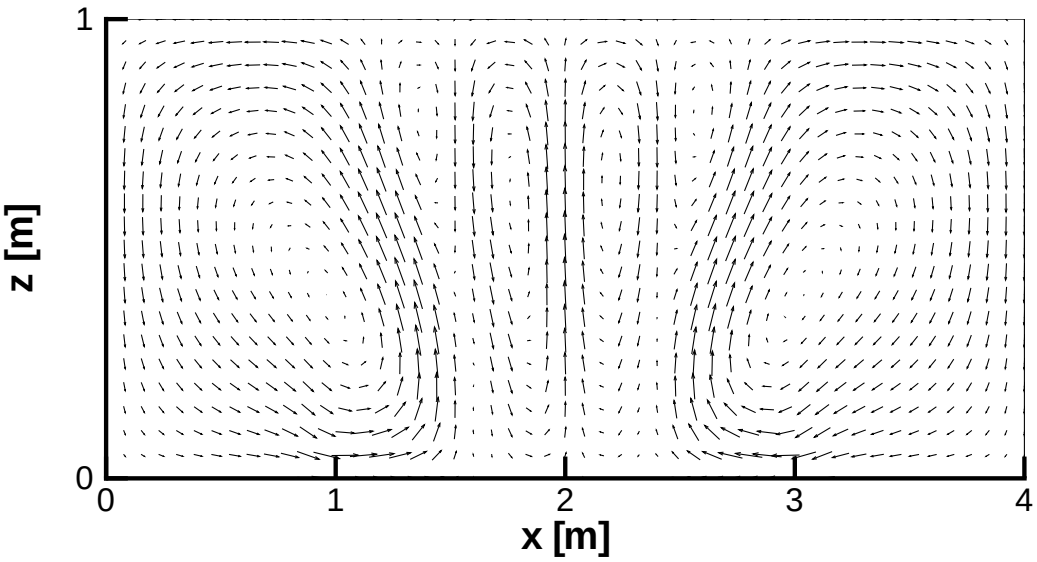

(b)

Figure 2.10: The same as Figure 2.7 at time $\tilde{t}_4$.

same, with a 2×2 m area heated at the bottom (red region in Figure 2.5a). The used parameters correspond to those given in (Table 2.2). The box is discretized with a regular tetrahedral grid of 192000 elements as shown in Figure 2.5b. The three-dimensional free convection process is similar to the two-dimensional case: eddies appear around the border of the heating area with four predominant patterns growing at the four corners at the beginning of the simulation (Figures 2.12 and 2.13). The distinctive features, i.e. no numerical oscillations and mesh effects, observed in the two-dimensional case are preserved. These results are in good agreement with similar ones published in the literature [e.g. Diersch & Kolditz, 1998].

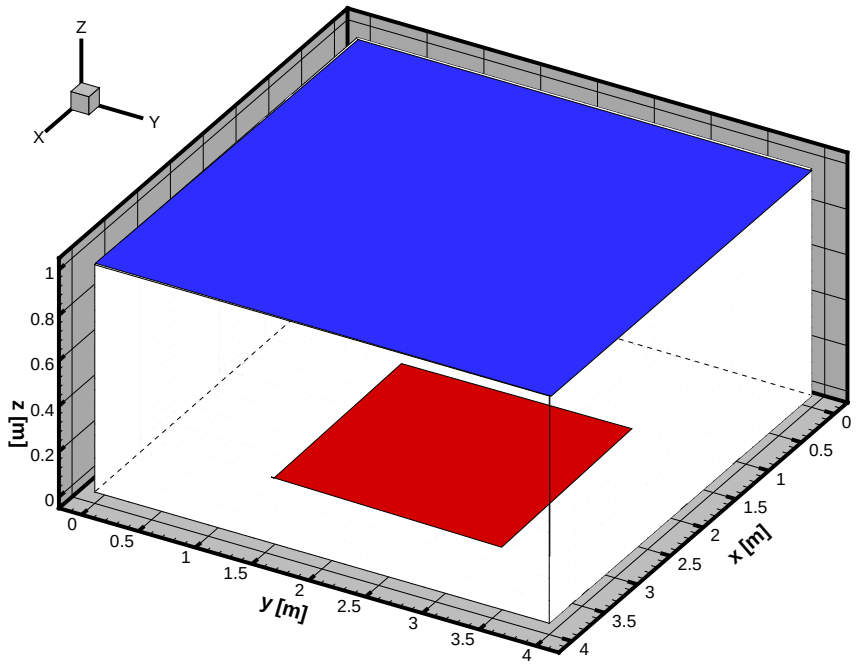

(a)

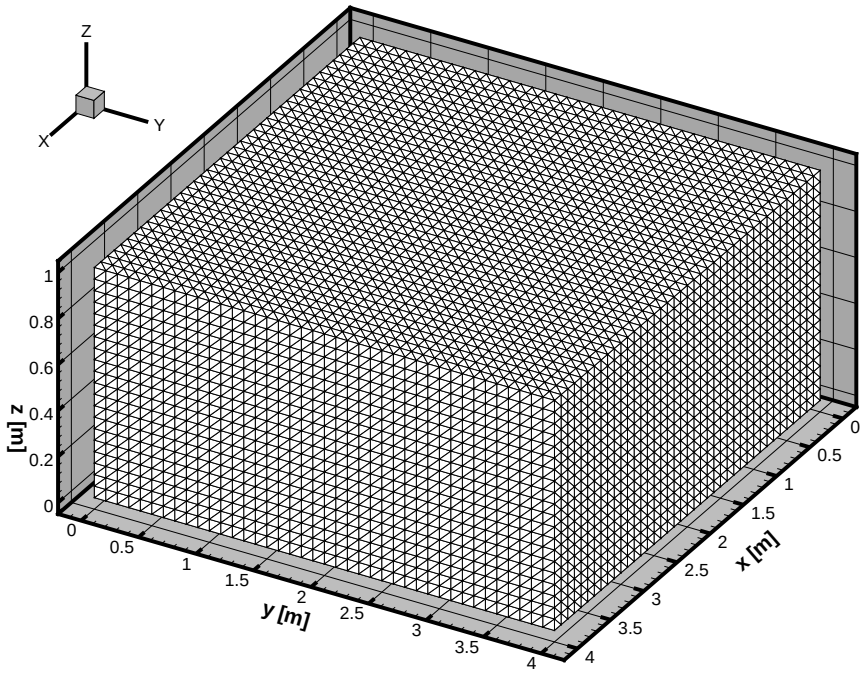

(b)

Figure 2.11: Definition of the extended 3D Elder's problem (a) and tetrahedral mesh used in the simulation (b).

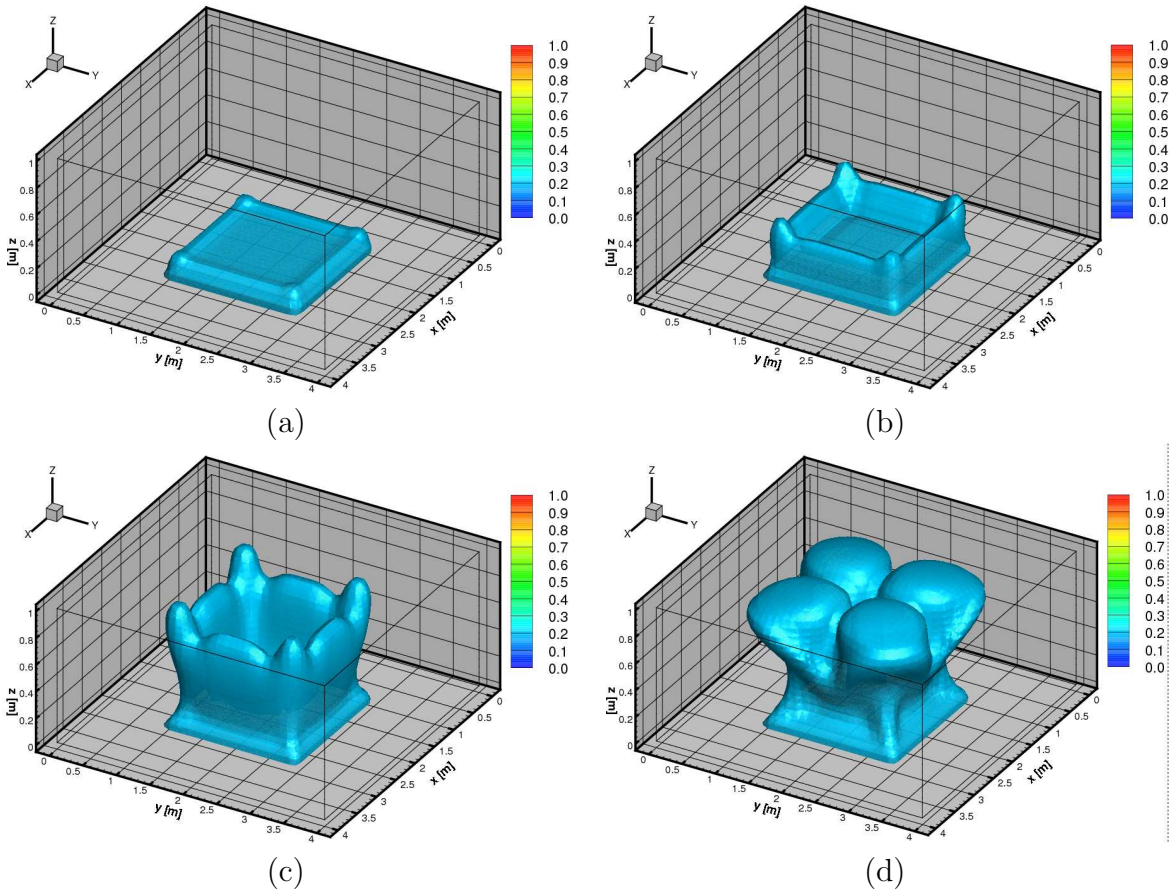

Figure 2.12: Three-dimensional view of the 0.2 dimensionless temperature isosurface at times $\tilde{t}_1$ (a), $\tilde{t}_2$ (b), $\tilde{t}_3$ (c) and $\tilde{t}_4$ (d).

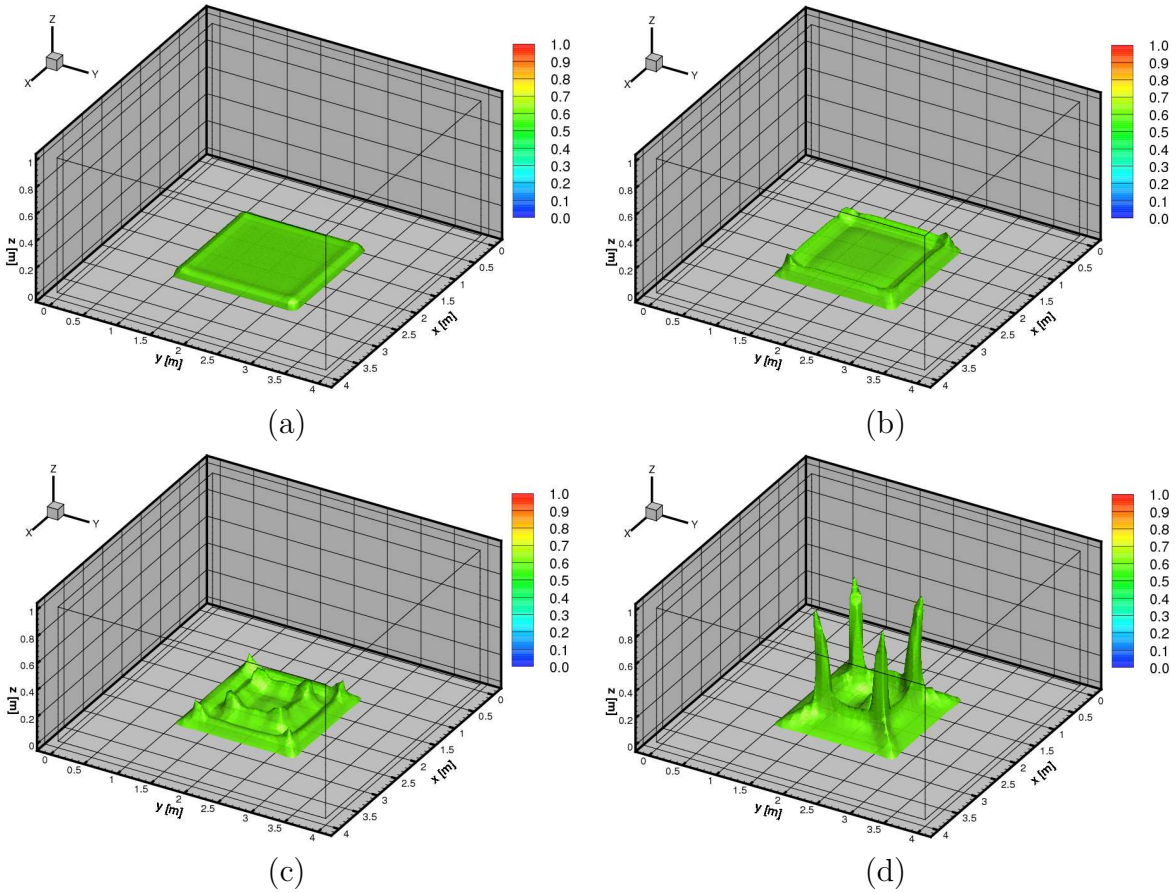

Figure 2.13: Three-dimensional view of the 0.6 dimensionless temperature isosurface at times $\tilde{t}_1$ (a), $\tilde{t}_2$ (b), $\tilde{t}_3$ (c) and $\tilde{t}_4$ (d).

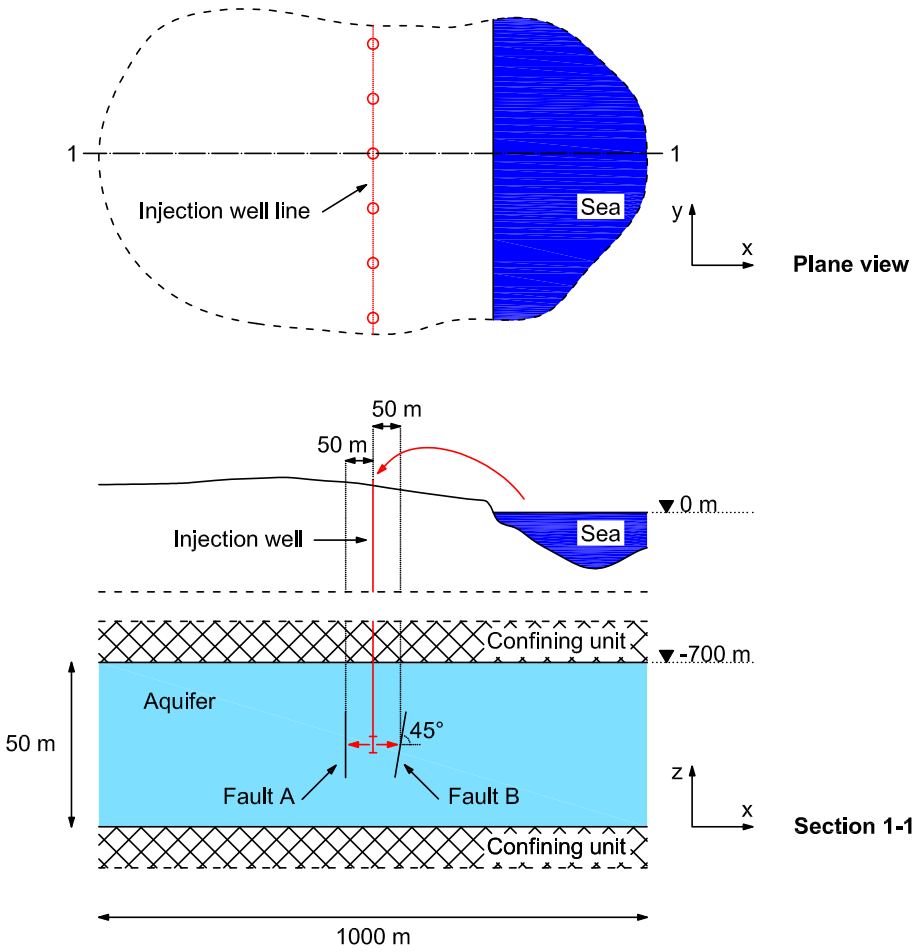

Figure 2.14: Sketch of the integration domain used in the numerical simulation: seawater is injected in a deep formation (*ciano*) and the injection wells (*red*) are placed forming a linear pattern. Two faults are located close to the injection line: fault A is vertical while fault B has a 45° inclination.

2.4.2 A 2-D aquifer injection example

Injecting water in producing oil fields is an important operation for EOR. Typically, water is taken from the sea, especially in offshore and near coastal operations, because of its abundance, compatibility with the formation water and ease of capture. Seawater injection can also be a useful option to mitigate land subsidence in coastal areas, as it will be discussed in detail in Chapter 4. This simple example of a deep aquifer injection is addressed to emphasize the GMMs model effectiveness in real field configurations, such as faulted geological formations.

A sketch of the domain is shown in Figure 2.14. Seawater is injected in a faulted

Symbol	Quantity	Value	Unit
ϕ	porosity	0.25	-
$K_{x,aquifer}$	horizontal hydraulic conductivity (aquifer)	0.14	m s^{-1}
$K_{x,faults}$	horizontal hydraulic conductivity (faults)	0.14×10^{-5}	m s^{-1}
$K_{z,aquifer}$	vertical hydraulic conductivity (aquifer)	0.14×10^{-2}	m s^{-1}
$K_{z,faults}$	vertical hydraulic conductivity (faults)	0.14×10^{-7}	m s^{-1}
S_s	elastic storage	0.8×10^{-3}	m^{-1}
λ_M	thermal conductivity of the porous medium	0.15	W m^{-1} $°C^{-1}$
$c_{v,M}$	heat capacity of the porous medium	3.76×10^6	J m^{-3} $°C^{-1}$
ρ_0	water Density	999.7	kg m^{-3}
α_L	longitudinal thermodispersivity	0	m
α_T	transverse thermodispersivity	0	m
$c_{v,f}$	heat capacity of the fluid	4.182×10^6	J m^{-3} $°C^{-1}$
β	water compressibility	9.22×10^{-10}	Pa^{-1}
β'	Thermal expansion coefficient of the fluid	$4,52 \times 10^{-4}$	$°C^{-1}$
α	viscosity coefficient	-0.6	$°C^{-1}$

Table 2.3: Simulation parameters for the aquifer injection of Figure 2.14.

homegeneous formation between 700 m and 750 m depth, with the injection wells forming a line-drive pattern. The flow does not exhibit significant variations in the y direction with the model reduced to a 2-D cross section. Two sealing faults are located 50 m left (A) and 50 m right (B) of the injection well: fault A is vertical while fault B has a 45° inclination. Hydrostatic pressure is initially assumed along with a constant temperature of 50 °C. The aquifer is confined on top and bottom by impermeable units while the outer boundaries preserve the initial pressure and temperature conditions. Faults are modelled as thin layers with hydraulic conductivity 5 orders of magnitude lower that of the aquifer, while thermal properties are uniform. The simulation parameters are summarized in Table 2.3. An unstructured mesh with 3587 nodes, 6746 triangles and 10332 edges is used. An overall constant source of 2 m^3 $day^{-1}m^{-1}$ is prescribed over 23 elements for a four-year period. Seawater temperature is assumed constant at 10 °C.

The overpressure and temperature distributions are shown in Figures 2.15 and 2.16, respectively, at four different instants. At the early stage of the injection, both pressure and temperature evolve symmetrically. When a fault is encountered the pressure propagates around it with a consequent temperature front distortion due to convection. MHFEs allow for an accurate description of the velocity field at the fault location as shown in Figures 2.17 and 2.18, because they are element-wise mass conservative. Observe also

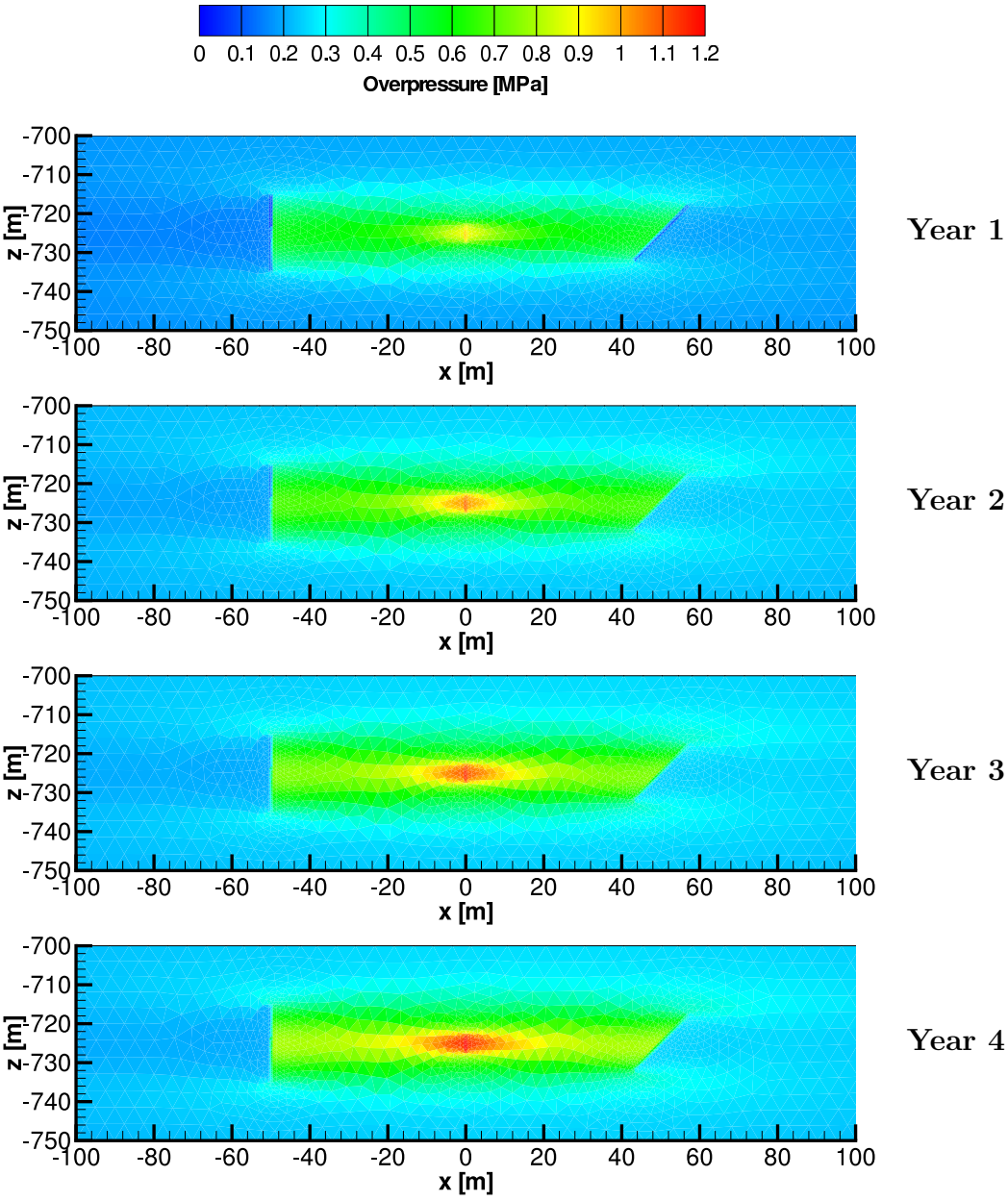

Figure 2.15: Overpressure distributions at several time steps.

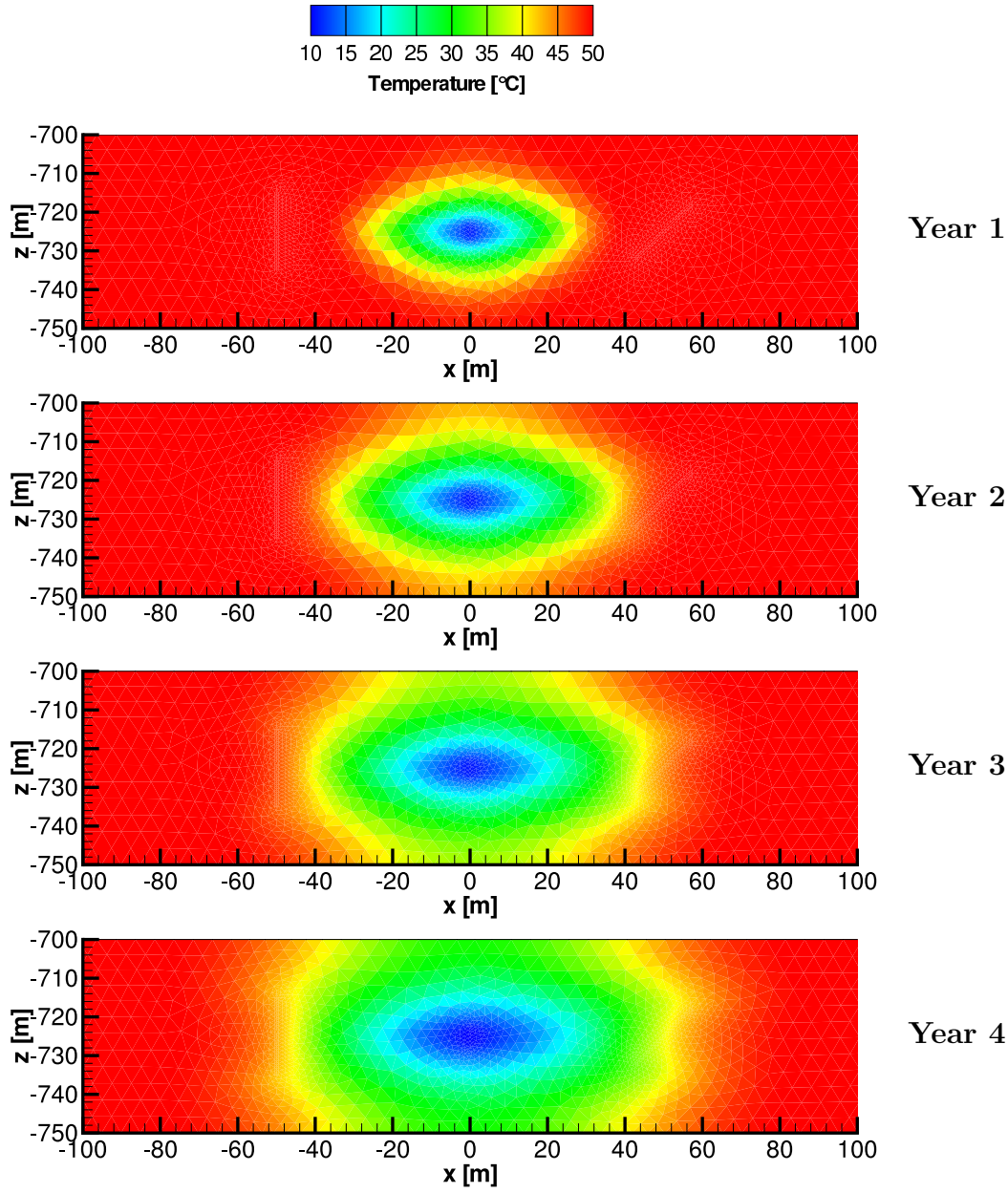

Figure 2.16: Temperature distributions at several time steps.

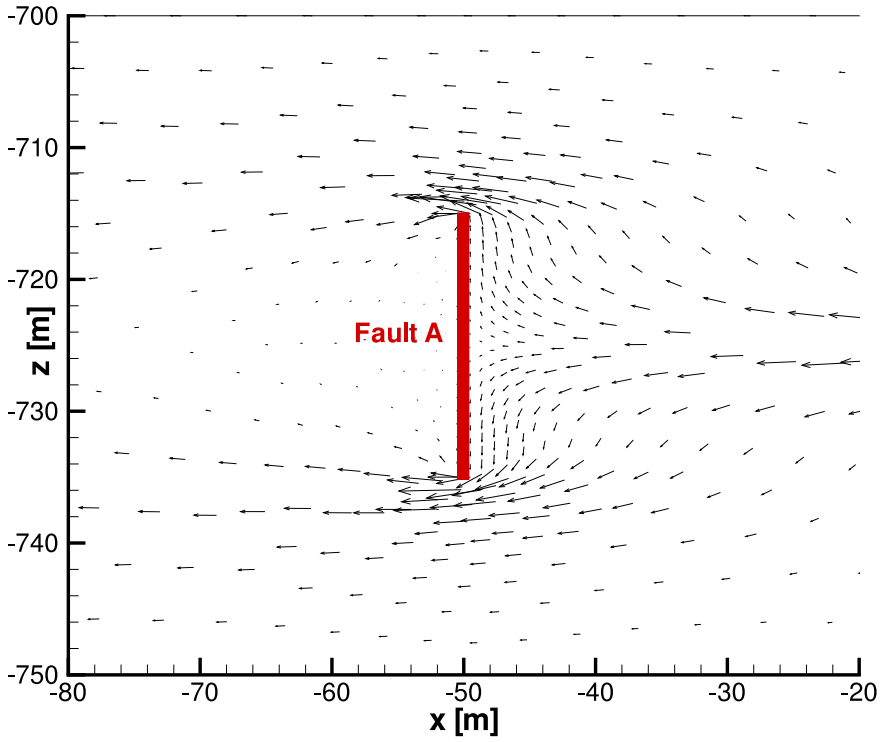

Figure 2.17: Velocity field around Fault A at 4 years.

that such accuracy is obtained avoiding an excessive mesh refinement by the faults, as traditional finite elements would have required.

2.5 Conclusions

A numerical method for coupled fluid flow and heat transfer in saturated porous media has been discussed. The model consists of a nonlinear system of partial differential equations solved by Godunov-Mixed Methods, combining MHFEs in the discretization of the diffusion term, both in the flow and the thermal equations, and a high-resolution cell-centered FV scheme for the convective term via a time-splitting tecnique. The solution is obtained through a Picard linearization scheme, solving the flow problem first, then the thermal balance, and iterating the procedure at each time step until convergence. Elder's problem, a typical challenging benchmark test involving severe nonlinearities due to strong density contrasts, has been used to verify the robustness and stability of the proposed scheme in both 2- and 3-D. Finally, the model has been used to simulate seawater injection into a faulted aquifer.

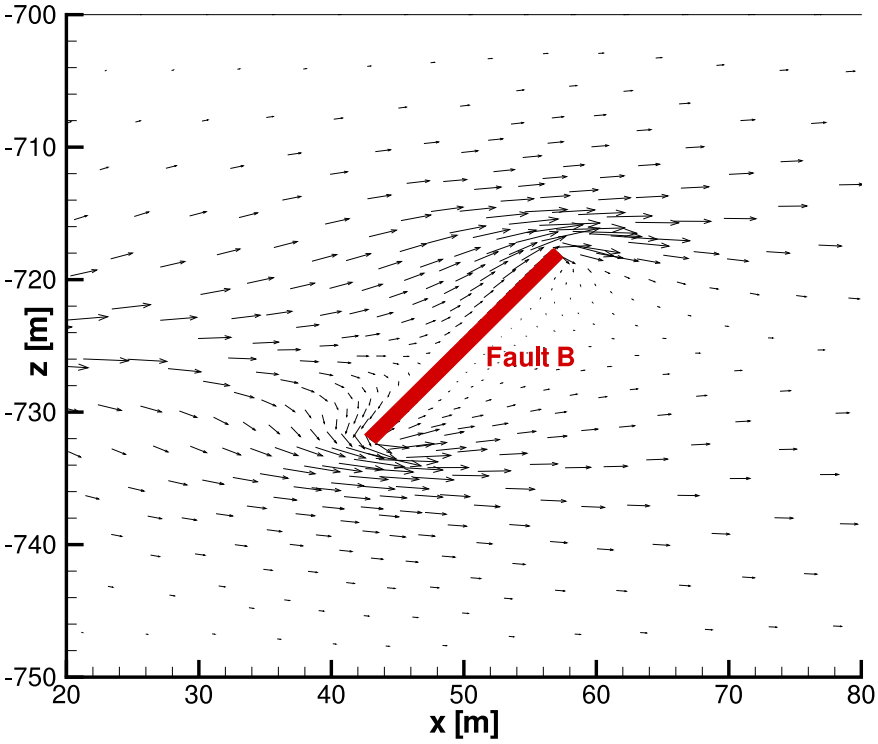

Figure 2.18: Velocity field around Fault B at 4 years.

The main results can be summarized as follows:

- the MHFE discretization for the flow equation leads to an element-wise mass-conservative scheme, providing an accurate discrete velocity field;
- the time-operator splitting approach for the heat transfer equation allows for the distinct treatment of the convective and the conductive contribution. For the convective step a FV scheme is selected because of its robustness in simulating very sharp fronts, while MHFEs are employed in the conductive step.
- MHFEs and cell-centered FVs are used with a weak variational form of the governing equations using similar basis functions for the approximated solution, with the practical benefit that only one grid is required;
- in the examples discussed herein, the numerical solution does not suffer from spurious oscillations and is negligibly affected by numerical diffusion;
- significant mesh effects are not encountered in both structured and unstructured grids. Hence, in convective-dominated problems or heterogeneous geological formations this formulation does not require an excessive mesh resolution in order to ensure accuracy and stability.

Chapter 3

A fully coupled 3-D Mixed Finite Element model of Biot consolidation

3.1 Introduction

Poro-elasticity denotes the coupled process between mechanics and flow in porous media. Its theoretical basis goes back to the mid 1920s when Terzaghi described analytically the one-dimensional (1-D) consolidation of a soil column under a constant load [Terzaghi, 1925]. In 1941 Biot generalized Terzaghi's theory to three-dimensional (3-D) porous media [Biot, 1941] by establishing the mathematical framework which is usually termed as poro-elasticity. Even though sophisticated, and perhaps more elegant, approaches have been recently advanced [e.g., Coussy, 1995], the Biot equations of consolidation are still used today in a great variety of fields, ranging from reservoir engineering to biomechanics. For example, poro-elasticity is the basic theory to predict the compaction of a producing hydrocarbon reservoir and the related hazards, including land subsidence and borehole damages [Pao *et al.*, 2001; Ferronato *et al.*, 2004; Yin *et al.*, 2009]. Several environmental issues connected with groundwater withdrawal [e.g., Teatini *et al.*, 2006], or the safe long-term disposal of wastes in the subsurface [e.g., Hudson *et al.*, 2001], can be addressed with the aid of poro-elastic models. In biomechanics the poro-elastic theory is used to describe tumor-induced stresses in the brain [Roose *et al.*, 2003] and the bone deformation under a mechanical load [Swan *et al.*, 2003].

Despite the intensive research in the area, the numerical solution to the Biot partial differential equations is still a challenging task for a number of reasons. First, the fully coupled approach leads to algebraic systems which can be quite difficult to solve. In

real 3-D applications the number of unknowns may easily grow up to several hundreds of thousands and the non-linearities in the constitutive laws of the porous medium can require multiple nested loops to be properly addressed. Second, the coefficient matrix resulting from the numerical discretization can be severely ill-conditioned especially at the early stage of the process [Ferronato *et al.*, 2001], hence advanced preconditioners with ad hoc solvers are needed to handle the fully coupled system [Bergamaschi *et al.*, 2008; Ferronato *et al.*, 2009a]. An alternative approach relies on the iteratively coupled scheme which solves separately in a staggered way the mechanical and the fluid flow models until convergence. If sufficiently tight convergence criteria are prescribed, the iteratively coupled solution can be as accurate as the fully coupled one, but the number of required steps might be prohibitively high. Moreover, convergence of the iterative procedure is not always guaranteed depending on the fluid and soil mechanical properties [Wheeler & Gai, 2007].

A third challenge is related to different forms of instabilities suffered by the numerical solution. For example, if an advection-dominated thermal process is associated to the Biot equations spurious oscillations may arise in the temperature and pressure fields because of sharp transient gradients [Idelson *et al.*, 1996]. However, the origin of most instabilities is due to the assumption that at the initial conditions the soil skeleton behaves as an incompressible medium if the pore fluid is so. Prescribing the volume change rate to be initially zero leads to the Finite Element (FE) pathology known as locking, which typically causes an oscillatory numerical behavior in the pore pressure. In practice, such an occurrence takes place even if the fluid compressibility is different from zero but small enough with respect to the bulk compressibility. This form of instability appears at times smaller than a critical bound depending on the porous medium permeability and stiffness [Vermeer & Verruijt, 1981]. Different remedies can be implemented to cope with such numerical difficulty. For example, Reed [1984] observed that using a different approximation order for displacement and pressure may help keep the spurious oscillations under control. In particular the pore pressure should be computed with the same approximation order as the stress, i.e. one order below the displacement, leading to the so-called Composite FEs characterized by a linear pressure and a quadratic displacement. Unfortunately, Composite FEs typically provide a less accurate prediction of the soil deformation [Sandhu *et al.*, 1977] with the oscillations in the pore pressure not entirely eliminated [Murad & Loula, 1994]. Post-processing techniques intended to smooth the spurious modes have been proposed with the aim at restoring the standard FE convergence rate [Reed, 1984; Murad & Loula, 1992]. More recently some approaches have been advanced based on

mixed formulations. The main advantage from the mixed approximation spaces relies on the possibility of solving nearly incompressible problems with no locking and a greater flexibility in describing independently pressures, stresses and displacements. Tchonkova *et al.* [2008] have developed a least-square mixed model for poro-elasticity yielding a positive definite discrete problem, while Phillips & Wheeler [2007a,b, 2008] have shown the theoretical convergence of two-dimensional (2-D) models that couple both continuous and discontinuous Galerkin elements for the displacements with mixed spaces for the fluid flow. A locally mass conservative approach coupling a mixed method for the flow problem with traditional FEs for the soil displacements has been proposed by Jha & Juanes [2007] who suggest solving the overall model by an unconditionally stable sequential scheme.

In the present chapter a fully coupled 3-D mixed FE formulation is developed to solve numerically the Biot equations of consolidation with the aim at alleviating the instabilities in the pore pressure solution. The fluid pore pressure and flux are approximated in the lowest order Raviart-Thomas mixed space, while linear tetrahedral FEs are used for the displacements. The main reasons for the above choices are threefold. First, keeping the flux as a primary variable allows for a greater accuracy in the velocity field, which can be of interest whenever a consolidation model is coupled with an advection-diffusion equation, e.g. to account for thermal effects or contaminant transport. Second, a mixed formulation for the flow problem is element-wise mass conservative because the normal flux is continuous across the element boundaries. Third, the practical advantages from using low-order interpolation elements, such as ease of implementation, refinement, and discretization of geometrically complex and heterogeneous domains, are thouroughly preserved. The chapter is organized as follows. After recalling the governing equations, the mixed variational formulation is developed in a 3-D setting with the discrete system of ordinary differential equations integrated in time. A fully coupled algorithm is then derived in detail using a block version of the Symmetric Quasi-Minimal Residual (SQMR) solver [Freund & Nachtingal, 1994] with an ad hoc developed block preconditioner. Finally, the Mixed FE model is validated against the well-known Terzaghi's analytical solution and compared to the results obtained from a standard FE method, with the relative merits discussed.

3.2 Mixed FE model of Biot consolidation

The interaction between a granular material and the fluid filling its pores is governed by a stress equilibrium equation coupled to a mass balance equation, with the relationship

linking the grain forces to the fluid pore pressure based on Terzaghi's effective stress principle. The equilibrium equation for an isotropic poro-elastic medium incorporating the effective stress concept reads:

$$G\nabla^2\hat{\delta\mathbf{x}} + \left(K + \frac{G}{3}\right)\nabla\mathrm{div}\hat{\delta\mathbf{x}} = b\nabla p + \rho\mathbf{g} \tag{3.1}$$

where G and K are the shear and bulk moduli, respsctively, b is the Biot coefficient, $\rho\mathbf{g}$ the body forces, $\hat{\delta\mathbf{x}}$ the medium displacements and p the fluid pore pressure. The fluid mass balance is prescribed by the continuity equation:

$$\mathrm{div}\mathbf{v} + \frac{\partial}{\partial t}\left(\phi\beta_f p + b\ \mathrm{div}\hat{\delta\mathbf{x}}\right) = f \tag{3.2}$$

where ϕ is the medium porosity, β_f the fluid compressibility, t time, f a flow source or sink and $\mathbf{v}$ the Darcy's velocity. Equation (3.2) must be coupled with the Darcy's law defining $\mathbf{v}$:

$$\overline{\boldsymbol{\kappa}}^{-1}\mathbf{v} + \nabla p = 0 \tag{3.3}$$

with $\overline{\boldsymbol{\kappa}} = \overline{\mathbf{k}}/\gamma_f$, $\overline{\mathbf{k}}$ the hydraulic conductivity tensor and γ_f the fluid specific weight.

Equations (3.1) through (3.3) form a coupled partial differential system defined on a 3-D domain Ω bounded by the frontier Γ with $\hat{\delta\mathbf{x}}$, $\mathbf{v}$ and p as unknowns. This system can be solved with appropriate boundary:

$$\begin{cases} \hat{\delta\mathbf{x}}\left(\mathbf{x},t\right) = \hat{\delta\mathbf{x}}_D\left(\mathbf{x},t\right) & \text{over } \Gamma_D \\ \overline{\boldsymbol{\sigma}}\left(\mathbf{x},t\right)\mathbf{n}\left(\mathbf{x}\right) = \mathbf{t}_N\left(\mathbf{x},t\right) & \text{over } \Gamma_N \\ p\left(\mathbf{x},t\right) = p_D\left(\mathbf{x},t\right) & \text{over } \Gamma_p \\ \mathbf{v}\left(\mathbf{x},t\right)\cdot\mathbf{n}\left(\mathbf{x}\right) = u_N\left(\mathbf{x},t\right) & \text{over } \Gamma_u \end{cases} \tag{3.4}$$

and initial conditions:

$$\begin{cases} \hat{\delta\mathbf{x}}\left(\mathbf{x},0\right) = \hat{\delta\mathbf{x}}_0\left(\mathbf{x}\right) \\ \mathbf{v}\left(\mathbf{x},0\right) = \mathbf{v}_0\left(\mathbf{x}\right) \\ p\left(\mathbf{x},0\right) = p_0\left(\mathbf{x}\right) \end{cases} \tag{3.5}$$

In equations (3.4) and (3.5) $\Gamma_D \cup \Gamma_N = \Gamma_p \cup \Gamma_u = \Gamma$, $\overline{\boldsymbol{\sigma}}$ is the total stress tensor, $\mathbf{n}$ the outer normal to Γ and $\mathbf{x}$ the position vector in $\mathbb{R}^3$, while the right-hand sides are known functions.

3.2.1 Variational formulation

Approximate the medium displacement in space with continuous piecewise linear polynomials ℓ_i, $i = 1, \ldots, n_n$, with n_n the number of FE nodes in Ω:

$$\hat{\delta\mathbf{x}}(\mathbf{x},t) = \begin{bmatrix} \hat{\delta x}_x(\mathbf{x},t) \\ \hat{\delta x}_y(\mathbf{x},t) \\ \hat{\delta x}_z(\mathbf{x},t) \end{bmatrix} \simeq \begin{bmatrix} \sum_{i=1}^{n_n} \ell_i(\mathbf{x})\,\delta x_{x,i}(t) \\ \sum_{i=1}^{n_n} \ell_i(\mathbf{x})\,\delta x_{y,i}(t) \\ \sum_{i=1}^{n_n} \ell_i(\mathbf{x})\,\delta x_{z,i}(t) \end{bmatrix} = N_{\delta x}(\mathbf{x})\,\delta\mathbf{x}(t) \tag{3.6}$$

The fluid pore pressure and Darcy's flux are discretized in space with piecewise constant polynomials and in the lowest order Raviart-Thomas space, respectively, satisfying the LBB condition that ensures the well-posedness of the discrete problem [Roberts & Thomas, 1991]. Denoting by n_e and n_f the number of elements and elemental edges, respectively, p and $\mathbf{v}$ are approximated as follows:

$$p(\mathbf{x},t) \simeq \sum_{j=1}^{n_e} h_j(\mathbf{x})\,p_j(t) = \mathbf{h}^T(\mathbf{x})\,\mathbf{p}(t) \tag{3.7}$$

$$\mathbf{v}(\mathbf{x},t) \simeq \sum_{k=1}^{n_f} \mathbf{w}_k(\mathbf{x})\,u_k(t) = W(\mathbf{x})\,\mathbf{u}(t) \tag{3.8}$$

where h_j are element-wise constant functions such that:

$$h_j(\mathbf{x}) = \begin{cases} 1 & \mathbf{x} \in T^{(j)} \\ 0 & \mathbf{x} \in \Omega - T^{(j)} \end{cases} \tag{3.9}$$

and $\mathbf{w}_k$ are vectorial functions in $\mathbb{R}^3$ associated to the k-th elemental edge:

$$\mathbf{w}_k(\mathbf{x}) = \pm\frac{1}{3\,|V(T^{(j)})|}(\mathbf{x} - \mathbf{x_k}) \tag{3.10}$$

In equations (3.9) and (3.10) $T^{(j)}$ denotes the j-th tetrahedron, V its volume and $\mathbf{x}_k$ the position vector of the node opposite to the k-th elemental edge in $T^{(j)}$. The $\pm$ sign in (3.10) identifies a conventional edge orientation such that $\mathbf{w}_k$ is oriented outward the element $T^{(j)}$ with the smallest index j. Because of this orientation, the function $\mathbf{w}_k$ gives rise to a unitary flux through the k-th elemental edge and a zero flux through all other edges. The vectors $\delta\mathbf{x}(t)$, $\mathbf{p}(t)$ and $\mathbf{u}(t)$ whose components are the nodal displacements $u_{x,i}$, $u_{y,i}$, $u_{z,i}$, the elemental pressures p_j and the edge normal fluxes u_k, respectively, are the discrete unknowns of the variational problem.

The elastic equilibrium equation (3.1) can be classically solved by minimizing the total potential energy in the domain Ω with the aid of the virtual work principle:

$$\int_{\Omega} \boldsymbol{\epsilon}^{v,T} \boldsymbol{\sigma} \, \mathrm{d}\Omega = \int_{\Omega} \hat{\delta \mathbf{x}}^{v,T} \rho \mathbf{g} \, \mathrm{d}\Omega + \int_{\Gamma_N} \hat{\delta \mathbf{x}}^{v,T} \mathbf{t}_N \, \mathrm{d}\Gamma \tag{3.11}$$

where $\boldsymbol{\epsilon}$ is the strain vector ($= B_{\delta x} \delta \mathbf{x}$, with $B_{\delta x}$ the strain elastic matrix) and $\boldsymbol{\sigma}$ is the total stress vector. The apex v denotes the virtual variables. Recalling Terzaghi's principle:

$$\boldsymbol{\sigma} = \boldsymbol{\sigma}' - bp\mathbf{i} \tag{3.12}$$

where $\boldsymbol{\sigma}'$ is the effective stress vector ($= D_e \boldsymbol{\epsilon}$, with D_e the elastic constant matrix) and $\mathbf{i}$ the Kronecker delta in vectorial form, and differentiating with respect to the virtual displacements, equation (3.11) yields:

$$\left(\int_{\Omega} B_{\delta x}^T D_e B_{\delta x} \, \mathrm{d}\Omega \right) \delta \mathbf{x} - \int_{\Omega} b B_{\delta x}^T \mathbf{i} p \, \mathrm{d}\Omega = \int_{\Omega} N_{\delta x}^T \rho \mathbf{g} \, \mathrm{d}\Omega + \int_{\Gamma_N} N_{\delta x}^T \mathbf{t}_N \, \mathrm{d}\Gamma \tag{3.13}$$

Using the pore pressure approximation (3.7) produces the final discrete form of equation (3.1):

$$K \delta \mathbf{x} - Q \mathbf{p} = \mathbf{f}_1 \tag{3.14}$$

where:

$$K = \int_{\Omega} B_{\delta x}^T D_e B_{\delta x} \, \mathrm{d}\Omega \tag{3.15}$$

$$Q = \int_{\Omega} b B_{\delta x}^T \mathbf{i} \mathbf{h}^T \, \mathrm{d}\Omega \tag{3.16}$$

$$\mathbf{f}_1 = \int_{\Omega} N_{\delta x}^T \rho \mathbf{g} \, \mathrm{d}\Omega + \int_{\Gamma_N} N_{\delta x}^T \mathbf{t}_N \, \mathrm{d}\Gamma \tag{3.17}$$

The Dirichlet boundary conditions along Γ_D are prescribed in a strong way.

The continuity equation (3.2) and the Darcy's law (3.3) are both solved by the Galerkin method of weighted residuals. Using the approximations (3.6) through (3.8) and orthogonalizing the residuals to $\mathbf{h}$ and W, respectively, give:

$$\int_{\Omega} \mathbf{h} \mathrm{div} \mathbf{v} \, \mathrm{d}\Omega + \int_{\Omega} \mathbf{h} \frac{\partial \phi \beta_f p}{\partial t} \, \mathrm{d}\Omega + \int_{\Omega} \mathbf{h} \frac{\partial b \mathrm{div} \hat{\delta \mathbf{x}}}{\partial t} \, \mathrm{d}\Omega = \int_{\Omega} \mathbf{h} f \, \mathrm{d}\Omega \tag{3.18}$$

$$\int_{\Omega} W^T \overline{\boldsymbol{\kappa}}^{-1} \mathbf{v} \, \mathrm{d}\Omega + \int_{\Omega} W^T \nabla p \, \mathrm{d}\Omega = 0 \tag{3.19}$$

Assuming that ϕ, β_f and b are independent of time and using a weak form for the last integral in equation (3.19), the semi-discrete Mixed FE expression of equations (3.2) and (3.3) read:

$$B^T \mathbf{u} + P \dot{\mathbf{p}} + Q^T \dot{\delta \mathbf{x}} = \mathbf{f}_2 \tag{3.20}$$

$$A\mathbf{u} - B\mathbf{p} = \mathbf{f}_3 \tag{3.21}$$

where:

$$A = \int_\Omega W^T \overline{\boldsymbol{\kappa}}^{-1} W \, \mathrm{d}\Omega \tag{3.22}$$

$$B = \int_\Omega \boldsymbol{\omega}\mathbf{h}^T \mathrm{d}\Omega \tag{3.23}$$

$$P = \int_\Omega \phi\beta_f \mathbf{h}\mathbf{h}^T \, \mathrm{d}\Omega \tag{3.24}$$

$$\mathbf{f}_2 = \int_\Omega \mathbf{h} f \, \mathrm{d}\Omega \tag{3.25}$$

$$\mathbf{f}_3 = -\int_{\Gamma_p} p_D W^T \mathbf{n} \, \mathrm{d}\Gamma \tag{3.26}$$

The components of $\boldsymbol{\omega}$ in (3.23) are equal to $\mathrm{div}(\mathbf{w}_k)$, $k = 1, \ldots, n_f$. Unlike standard FEs, the Dirichlet boundary conditions are the natural conditions for equation (3.21) and are therefore prescribed in a weak way, whereas the Neumann boundary conditions are to be imposed in a strong way.

3.2.2 Numerical implementation

The system of differential-algebraic equations (3.14), (3.20) and (3.21) is numerically integrated in time by a finite difference scheme. Consider any time-dependent function to vary linearly in time between t and $t + \Delta t$, and approximate any time-derivative at the intermediate instant t^*:

$$t^* = \vartheta\,(t + \Delta t) + (1 - \vartheta)\, t \tag{3.27}$$

with a simple incremental ratio. In equation (3.27) ϑ is a scalar value comprised between 0 and 1. The discrete solution scheme thus obtained is the following:

$$\vartheta\left[K\delta\mathbf{x}^{t+\Delta t} - Q\mathbf{p}^{t+\Delta t}\right] = (1-\vartheta)\left[Q\mathbf{p}^t - K\delta\mathbf{x}^t + \mathbf{f}_1^t\right] + \vartheta\mathbf{f}_1^{t+\Delta t} \tag{3.28}$$

$$\begin{aligned}\frac{Q^T\delta\mathbf{x}^{t+\Delta t} + P\mathbf{p}^{t+\Delta t}}{\Delta t} + \vartheta B^T\mathbf{u}^{t+\Delta t} &= (1-\vartheta)\left[\mathbf{f}_2^{t+\Delta t} - B^T\mathbf{u}^t\right] + \\ &+ \frac{Q^T\delta\mathbf{x}^t + P\mathbf{p}^t}{\Delta t} + \vartheta\mathbf{f}_2^{t+\Delta t}\end{aligned} \tag{3.29}$$

$$\vartheta\left[A\mathbf{u}^{t+\Delta t} - B\mathbf{p}^{t+\Delta t}\right] = (1-\vartheta)\left[B\mathbf{p}^t - A\mathbf{u}^t + \mathbf{f}_3^t\right] + \vartheta\mathbf{f}_3^{t+\Delta t} \tag{3.30}$$

Set $\gamma = \vartheta\Delta t$ and $\psi = (1-\vartheta)/\vartheta$, divide equation (3.28) by $-\vartheta$, multiply equation (3.29) by Δt and equation (3.30) by $-\Delta t$. The numerical solution at time $t+\Delta t$ can be therefore

computed by solving a linear algebraic system:

$$\mathcal{A}\mathbf{z}^{t+\Delta t} = \mathbf{f}^t \tag{3.31}$$

where:

$$\mathcal{A} = \begin{bmatrix} P & Q^T & \gamma B^T \\ Q & -K & 0 \\ \gamma B & 0 & -\gamma A \end{bmatrix} \qquad \mathbf{z}^{t+\Delta t} = \begin{bmatrix} \mathbf{p}^{t+\Delta t} \\ \delta\mathbf{x}^{t+\Delta t} \\ \mathbf{u}^{t+\Delta t} \end{bmatrix} \qquad \mathbf{f}^t = \begin{bmatrix} \mathbf{f}^{(p)} \\ \mathbf{f}^{(\delta x)} \\ \mathbf{f}^{(u)} \end{bmatrix} \tag{3.32}$$

$$\mathbf{f}^{(p)} = (\Delta t - \gamma)\left[\mathbf{f}_2^t - B^T\mathbf{u}^t\right] + Q^T\delta\mathbf{x}^t + P\mathbf{p}^t + \gamma\mathbf{f}_2^{t+\Delta t} \tag{3.33}$$

$$\mathbf{f}^{(\delta x)} = \psi\left[K\delta\mathbf{x}^t - Q\mathbf{p}^t - \mathbf{f}_1^t\right] - \mathbf{f}_1^{t+\Delta t} \tag{3.34}$$

$$\mathbf{f}^{(u)} = (\Delta t - \gamma)\left[A\mathbf{u}^t - B\mathbf{p}^t - \mathbf{f}_3^t\right] - \gamma\mathbf{f}_2^{t+\Delta t} \tag{3.35}$$

The matrix $\mathcal{A}$ in (3.31) has size $n_e + 3n_n + n_f$ and is sparse, symmetric and indefinite. Suitable solvers for (3.31) belong to the class of the iterative projection-type Krylov subspace methods properly preconditioned. The explicit construction of $\mathcal{A}$, however, is generally not convenient from a computational point of view. In fact, while A, B, K, P and Q can be computed just once at the beginning of the simulation as they do not depend on t, $\mathcal{A}$ changes at each step because Δt, hence γ, is generally increased as the consolidation proceeds. Therefore a specific block version of a preconditioned Krylov subspace method is to be implemented.

As far as the preconditioner is concerned, a variant of the block constraint approach successfully applied to standard FE consolidation models [Bergamaschi *et al.*, 2008; Ferronato *et al.*, 2009a] is developed. Write $\mathcal{A}$ as a 2×2 block matrix:

$$\mathcal{A} = \begin{bmatrix} P & H^T \\ H & -C \end{bmatrix} \tag{3.36}$$

with:

$$H = \begin{bmatrix} Q \\ \gamma B \end{bmatrix} \qquad C = \begin{bmatrix} K & 0 \\ 0 & \gamma A \end{bmatrix} \tag{3.37}$$

Note that C is a block-diagonal symmetric positive definite (SPD) matrix, as both K and A are SPD and γ is positive. Now consider the following $\mathcal{A}$ decomposition:

$$\mathcal{A} = \begin{bmatrix} I & 0 \\ HP^{-1} & I \end{bmatrix} \begin{bmatrix} P & 0 \\ 0 & -S \end{bmatrix} \begin{bmatrix} I & P^{-1}H^T \\ 0 & I \end{bmatrix} \tag{3.38}$$

where S is the SPD Schur complement:

$$S = C + HP^{-1}H^T = \begin{bmatrix} K + QP^{-1}Q^T & \gamma QP^{-1}B^T \\ \gamma BP^{-1}Q^T & \gamma A + \gamma^2 BP^{-1}B^T \end{bmatrix} \tag{3.39}$$

Equations (3.38) and (3.39) could be computed exactly as P is diagonal, however S is much less sparse than C, hence some dropping can be conveniently enforced. A simple approximation relies on prescribing the dropped S to preserve the same block diagonal structure as C:

$$S \simeq \widetilde{S} = \begin{bmatrix} \widetilde{S}_1 & 0 \\ 0 & \widetilde{S}_2 \end{bmatrix} = \begin{bmatrix} K + QP^{-1}Q^T & 0 \\ 0 & \gamma A + \gamma^2 BP^{-1}B^T \end{bmatrix} \tag{3.40}$$

The blocks $\widetilde{S}_1$ and $\widetilde{S}_2$ cannot be efficiently inverted, so an additional approximation is performed by replacing them with their incomplete Cholesky factorizations:

$$\widetilde{S} \simeq \begin{bmatrix} L_{S1}L_{S1}^T & 0 \\ 0 & L_{S2}L_{S2}^T \end{bmatrix} = L_S L_S^T \tag{3.41}$$

$\widetilde{S}$ is used in equation (3.38) in place of the exact Schur complement S, thus providing a factored approximation of $\mathcal{A}$ that can be used as preconditioner. Inverting equation (3.38) and accounting for (3.41) yields:

$$\mathcal{M}^{-1} = \mathcal{U}^{-1}\mathcal{L}^{-1} = \begin{bmatrix} I & -P^{-1}H^T L_S^{-T} \\ 0 & L_S^{-T} \end{bmatrix} \begin{bmatrix} P^{-1} & 0 \\ L_S^{-1}HP^{-1} & -L_S^{-1} \end{bmatrix} \tag{3.42}$$

with $\mathcal{M}^{-1}$ the Constraint Preconditioner (CP).

Preconditioner (3.42) is used to accelerate the SQMR solver [Freund & Nachtingal, 1994] which has proved a robust and efficient algorithm for sparse symmetric indefinite problems [e.g., Toh & Poon, 2008; Ferronato *et al.*, 2009b]. An ad hoc block version, however, is to be implemented. The resulting Block CP-SQMR algorithm for the solution of equations (3.31) is provided in Table 3.1. The repeated solution of equations (3.31) starting from the initial conditions (3.5) gives the discrete vectors $\delta\mathbf{x}$, $\mathbf{p}$ and $\mathbf{u}$ at the selected values of time, hence the approximate $\hat{\delta\mathbf{x}}$, p and $\mathbf{v}$ through equations (3.6), (3.7) and (3.8), respectively.

SET $\vartheta_0 = 0$, $\mathbf{d}_0^{(p)} = \mathbf{0}$, $\mathbf{d}_0^{(\delta x)} = \mathbf{0}$, $\mathbf{d}_0^{(u)} = \mathbf{0}$

CHOOSE $\mathbf{p}_0$, $\delta\mathbf{x}_0$, $\mathbf{u}_0$ ARBITRARILY

$$\mathbf{r}_0^{(p)} = \mathbf{f}^{(p)} - P\mathbf{p}_0 - Q^T\delta\mathbf{x}_0 - \gamma B^T\mathbf{u}_0$$
$$\mathbf{r}_0^{(\delta x)} = \mathbf{f}^{(\delta x)} - Q\mathbf{p}_0 + K\delta\mathbf{x}_0$$
$$\mathbf{r}_0^{(u)} = \mathbf{f}^{(u)} - \gamma\left(B\mathbf{p}_0 - A\mathbf{u}_0\right)$$

$$\mathbf{t}_0^{(p)} = P^{-1}\mathbf{r}_0^{(p)}$$
$$\mathbf{t}_0^{(\delta x)} = L_{S1}^{-1}\left(Q\mathbf{t}_0^{(p)} - \mathbf{r}_0^{(\delta x)}\right)$$
$$\mathbf{t}_0^{(u)} = L_{S2}^{-1}\left(\gamma B\mathbf{t}_0^{(p)} - \mathbf{r}_0^{(u)}\right)$$

$$\tau_0 = \sqrt{\|\mathbf{t}_0^{(p)}\|_2^2 + \|\mathbf{t}_0^{(\delta x)}\|_2^2 + \|\mathbf{t}_0^{(u)}\|_2^2}$$

$$\mathbf{w}_0^{(u)} = L_{S2}^{-T}\mathbf{t}_0^{(u)}$$
$$\mathbf{w}_0^{(\delta x)} = L_{S1}^{-T}\mathbf{t}_0^{(\delta x)}$$
$$\mathbf{w}_0^{(p)} = \mathbf{t}_0^{(p)} - P^{-1}\left(Q^T\mathbf{w}_0^{(\delta x)} + \gamma B^T\mathbf{w}_0^{(u)}\right)$$

$$\rho_0 = \mathbf{r}_0^{(p),T}\mathbf{w}_0^{(p)} + \mathbf{r}_0^{(\delta x),T}\mathbf{w}_0^{(\delta x)} + \mathbf{r}_0^{(u),T}\mathbf{w}_0^{(u)}$$

DO $k = 1, 2, \ldots$ UNTIL CONVERGENCE

$$\mathbf{s}_k^{(p)} = P\mathbf{w}_{k-1}^{(p)} + Q^T\mathbf{w}_{k-1}^{(\delta x)} + \gamma B^T\mathbf{w}_{k-1}^{(u)}$$
$$\mathbf{s}_k^{(\delta x)} = Q\mathbf{w}_{k-1}^{(p)} - K\mathbf{w}_{k-1}^{(\delta x)}$$
$$\mathbf{s}_k^{(u)} = \gamma\left(B\mathbf{w}_{k-1}^{(p)} - A\mathbf{w}_{k-1}^{(u)}\right)$$

$$\sigma_k = \mathbf{w}_{k-1}^{(p),T}\mathbf{s}_k^{(p)} + \mathbf{w}_{k-1}^{(\delta x),T}\mathbf{s}_k^{(\delta x)} + \mathbf{w}_{k-1}^{(u),T}\mathbf{s}_k^{(u)}$$

IF $[(\sigma_k = 0)$ OR $(\rho_{k-1} = 0)]$ THEN

STOP WITH SOLUTION $\mathbf{p}_{k-1}$, $\delta\mathbf{x}_{k-1}$, $\mathbf{u}_{k-1}$

ELSE

$$\alpha_k = \rho_{k-1}/\sigma_k$$

$$\mathbf{r}_k^{(p)} = \mathbf{r}_{k-1}^{(p)} - \alpha_k\mathbf{s}_k^{(p)}$$
$$\mathbf{r}_k^{(\delta x)} = \mathbf{r}_{k-1}^{(\delta x)} - \alpha_k\mathbf{s}_k^{(\delta x)}$$
$$\mathbf{r}_k^{(u)} = \mathbf{r}_{k-1}^{(u)} - \alpha_k\mathbf{s}_k^{(u)}$$

$$\mathbf{t}_k^{(p)} = P^{-1}\mathbf{r}_k^{(p)}$$
$$\mathbf{t}_k^{(\delta x)} = L_{S1}^{-1}\left(Q\mathbf{t}_k^{(p)} - \mathbf{r}_k^{(\delta x)}\right)$$
$$\mathbf{t}_k^{(u)} = L_{S2}^{-1}\left(\gamma B\mathbf{t}_k^{(p)} - \mathbf{r}_k^{(u)}\right)$$

$\ldots$

$$\ldots$$

$$\vartheta_k = \left(\sqrt{\|\mathbf{t}_k^{(p)}\|_2^2 + \|\mathbf{t}_k^{(\delta x)}\|_2^2 + \|\mathbf{t}_k^{(u)}\|_2^2} \right) / \tau_{k-1}$$

$$\psi_k = 1/\sqrt{1+\vartheta_k^2}$$

$$\tau_k = \tau_{k-1}\vartheta_k\psi_k$$

$$\mathbf{d}_k^{(p)} = \psi_k^2\vartheta_{k-1}^2\mathbf{d}_{k-1}^{(p)} + \psi_k^2\alpha_k\mathbf{w}_{k-1}^{(p)}$$
$$\mathbf{d}_k^{(\delta x)} = \psi_k^2\vartheta_{k-1}^2\mathbf{d}_{k-1}^{(\delta x)} + \psi_k^2\alpha_k\mathbf{w}_{k-1}^{(\delta x)}$$
$$\mathbf{d}_k^{(u)} = \psi_k^2\vartheta_{k-1}^2\mathbf{d}_{k-1}^{(u)} + \psi_k^2\alpha_k\mathbf{w}_{k-1}^{(u)}$$

$$\mathbf{p}_k = \mathbf{p}_{k-1} + \mathbf{d}_k^{(p)}$$

$$\delta\mathbf{x}_k = \delta\mathbf{x}_{k-1} + \mathbf{d}_k^{(\delta x)}$$

$$\mathbf{u}_k = \mathbf{u}_{k-1} + \mathbf{d}_k^{(u)}$$

$$\mathbf{v}_k^{(u)} = L_{S2}^{-T}\mathbf{t}_k^{(u)}$$
$$\mathbf{v}_k^{(\delta x)} = L_{S1}^{-T}\mathbf{t}_k^{(\delta x)}$$
$$\mathbf{v}_k^{(p)} = \mathbf{t}_k^{(p)} - P^{-1}\left(Q^T\mathbf{v}_k^{(\delta x)} + \gamma B^T\mathbf{v}_k^{(u)}\right)$$

$$\rho_k = \mathbf{r}_k^{(p),T}\mathbf{v}_k^{(p)} + \mathbf{r}_k^{(\delta x),T}\mathbf{v}_k^{(\delta x)} + \mathbf{r}_k^{(u),T}\mathbf{v}_k^{(u)}$$

$$\beta_k = \rho_k/\rho_{k-1}$$

$$\mathbf{w}_k^{(p)} = \mathbf{v}_k^{(p)} + \beta_k\mathbf{w}_{k-1}^{(p)}$$
$$\mathbf{w}_k^{(\delta x)} = \mathbf{v}_k^{(\delta x)} + \beta_k\mathbf{w}_{k-1}^{(\delta x)}$$
$$\mathbf{w}_k^{(u)} = \mathbf{v}_k^{(u)} + \beta_k\mathbf{w}_{k-1}^{(u)}$$

End If

End Do

Table 3.1: Block CP-SQMR algorithm.

3.3 Numerical results

The stability and accuracy of the 3-D Mixed FE consolidation model previously described is investigated with the aid of a few examples. The model is validated against analytical solutions and it is compared to a standard FE model.

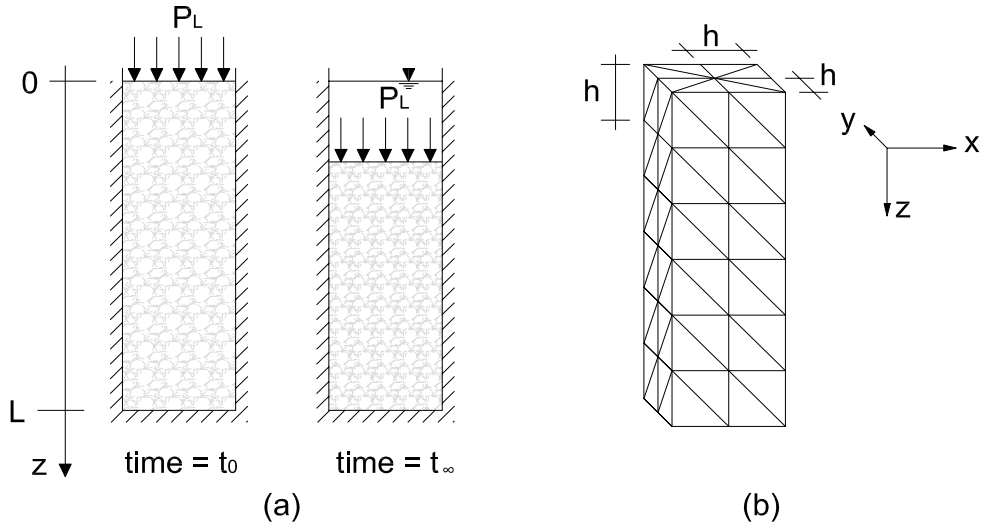

Figure 3.1: Sketch of the setup for Terzaghi's consolidation test.

3.3.1 Model validation

The model is validated against Terzaghi's classical consolidation problem, consisting of a fluid-saturated column of height L with a constant loading P_L on top (Figure 3.1). Drainage is allowed for through the upper moving boundary only. The basement is fixed. The load is applied istantaneously at time $t = 0$ yielding a non-zero initial overpressure $p_0(z)$ and a corresponding settlement $\delta x_{z,0}(z)$. Assuming the z-axis positive downward, the analytical solution reads [Wang, 2001; Wang & Hsu, 2009]:

$$p(z,t) = \frac{4}{\pi} p_0 \sum_{m=0}^{\infty} \frac{1}{2m+1} \exp\left[\frac{-(2m+1)^2 \pi^2 ct}{4L^2}\right] \sin\left[\frac{(2m+1)\pi z}{2L}\right] \tag{3.43}$$

$$\delta x_z(z,t) = c_M p_0 \left\{ (L-z) - \frac{8L}{\pi^2} \sum_{m=0}^{\infty} \frac{1}{(2m+1)^2} \exp\left[\frac{-(2m+1)^2 \pi^2 ct}{4L^2}\right] \cos\left[\frac{(2m+1)\pi z}{2L}\right] \right\} + \delta x_{z,0} \tag{3.44}$$

where:

$$p_0(z) = \frac{bM}{K_u + 4G/3} P_L \tag{3.45}$$

$$\delta x_{z,0}(z) = \frac{1}{K_u + 4G/3} P_L (L - z) \tag{3.46}$$

with $M = [\phi\beta_f + (b-\phi)\beta_s]^{-1}$ the Biot modulus, β_s the solid grain compressibility, $K_u = K + b^2 M$ the undrained bulk modulus, $c_M = (K + 4G/3)^{-1}$ the vertical uniaxial compressibility, and $c = k/[\gamma_f (M^{-1} + b^2 c_M)]$ the consolidation coefficient.

	Porous Column
k_{sand} [m/s]	10^{-5}
k_{clay} [m/s]	10^{-8}
ϕ	0.375
β_f [MPa^{-1}]	4.4×10^{-4}
K [MPa]	66.7
G [MPa]	40.0
b	1.0

Table 3.2: Hydraulic and mechanical parameters of the porous column used for the model validation. In Terzaghi's consolidation test the sample is made from sand only.

A homogeneous sandy column with unit section and $L = 15$ m is simulated, with the relevant hydraulic and mechanical properties given in Table 3.2. The prescribed distributed load P_L is 10^4 Pa. The column is discretized into regular tetrahedrals with a characteristic element size $h = 0.5$ m (Figure 3.1). The time integration is performed with a first-order implicit scheme ($\vartheta = 1$) and a constant time step $\Delta t = 0.1$ s. The simulation proceeds until steady state conditions are attained. A good matching between the analytical and the numerical solution is obtained for both pore pressure and vertical displacement, as it is shown in Figure 3.2 and 3.3, respectively.

The convergence properties of the 3D Mixed FE model have been investigated by comparing the analytical solutions (3.43)-(3.44) at $t = 60$ s with the numerical solution obtained on progressively refined computational grids, ranging from $h = 1$ m to 0.0625 m. In Figure 3.4 the L^∞-norm of the pressure error is plotted vs. h in a double log-log plot. The profile exhibits initially a linear behaviour, then it flattens out as h decreases. This agrees with the theoretical results provided in Phillips & Wheeler [2007b] for a 1-D formulation, with the lack of convergence basically due to the time discretization error. A similar remark holds true for the displacements using the L^2-norm of the error (Figure 3.5). Consistent with the pore pressure L^∞-norm profile, the theoretical quadratic convergence [Phillips & Wheeler, 2007b] is progressively lost as h decreases while Δt is kept constant. Figure 3.6 shows the relative residual norm:

$$r_r = \frac{\|\mathbf{f}^t - \mathcal{A}\mathbf{z}^{t+\Delta t}\|_2}{\|\mathbf{f}^t\|_2} \tag{3.47}$$

vs. the number of iterations required by the CP-SQMR algorithm of Table 3.1 to solve the linear system (3.31). The different number of CP-SQMR iterations to converge indicates that the conditioning of $\mathcal{A}$ gets worse as h decreases and Δt increases, which is consistent with the numerical behaviour typically encountered in mixed FE models of subsurface

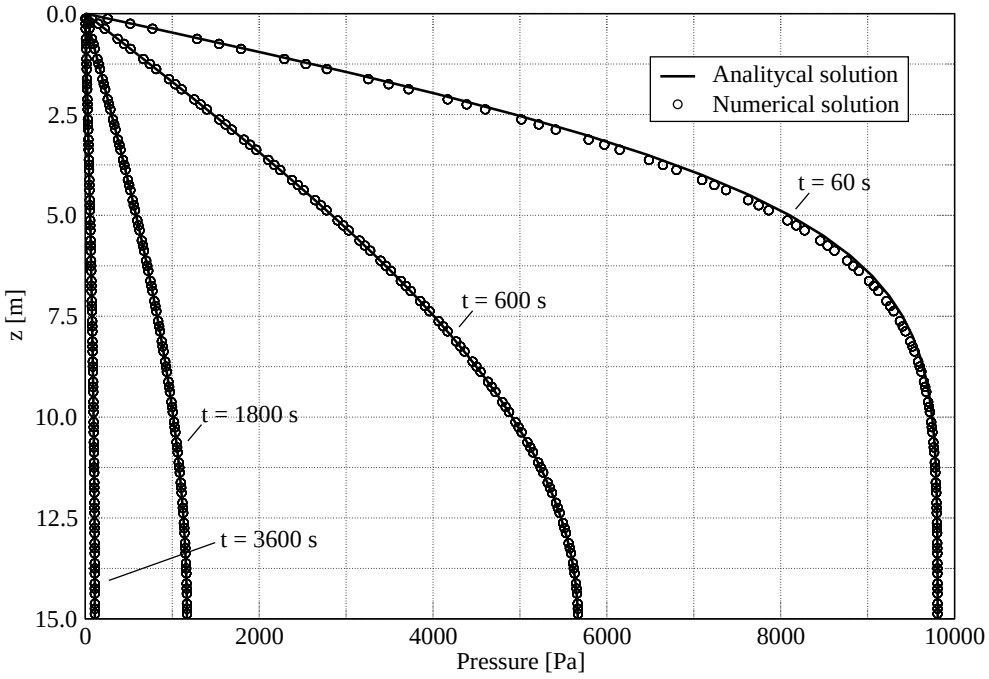

Figure 3.2: Terzaghi's consolidation test: analytical and numerical solutions for the pore pressure.

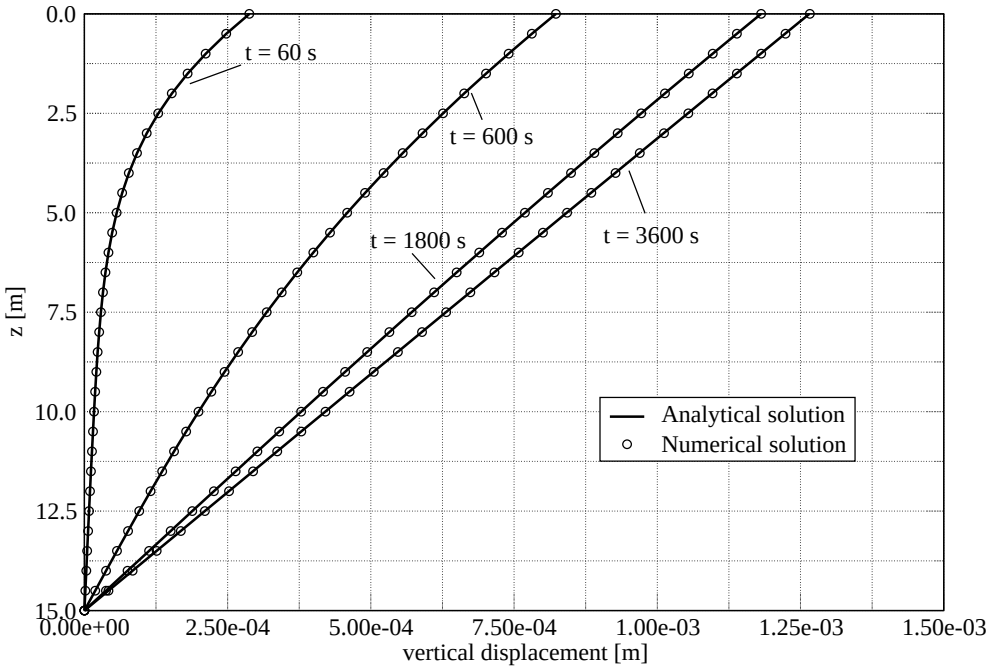

Figure 3.3: Terzaghi's consolidation test: analytical and numerical solutions for the vertical displacement.

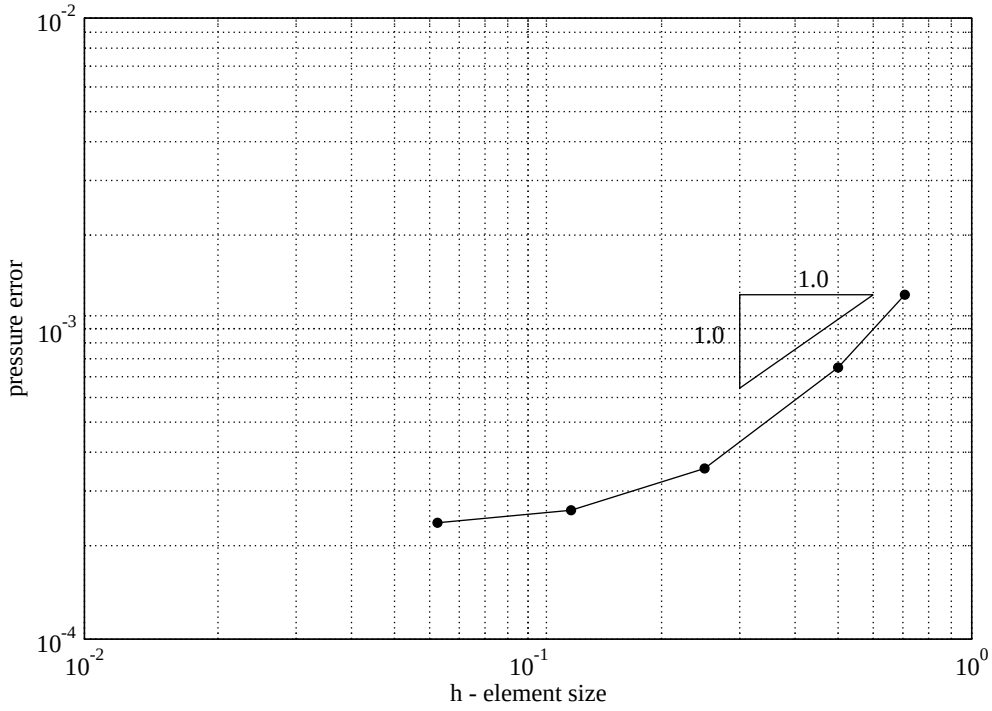

Figure 3.4: Terzaghi's consolidation test: L^∞ pressure error norm vs. spacing h.

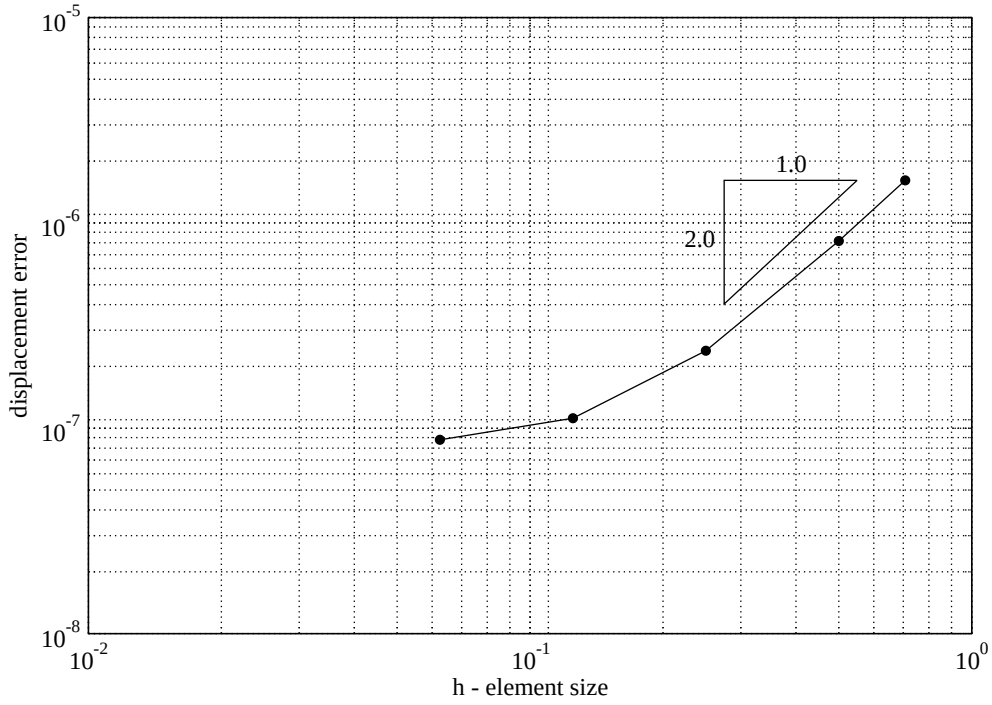

Figure 3.5: Terzaghi's consolidation test: L^2 displacement error norm vs. spacing h.

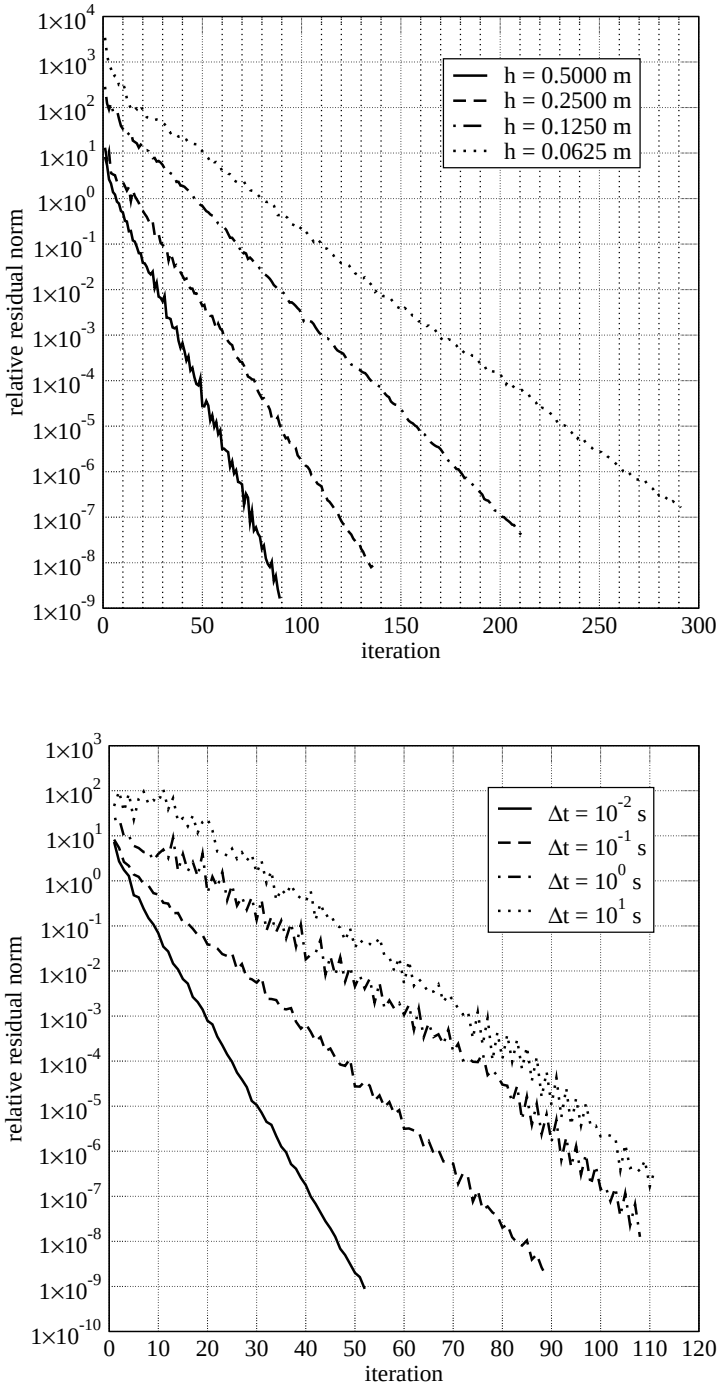

Figure 3.6: CP-SQMR convergence profiles varying h with $\Delta t = 0.01$ s (top) and varying Δt with $h = 0.5$ m (bottom).

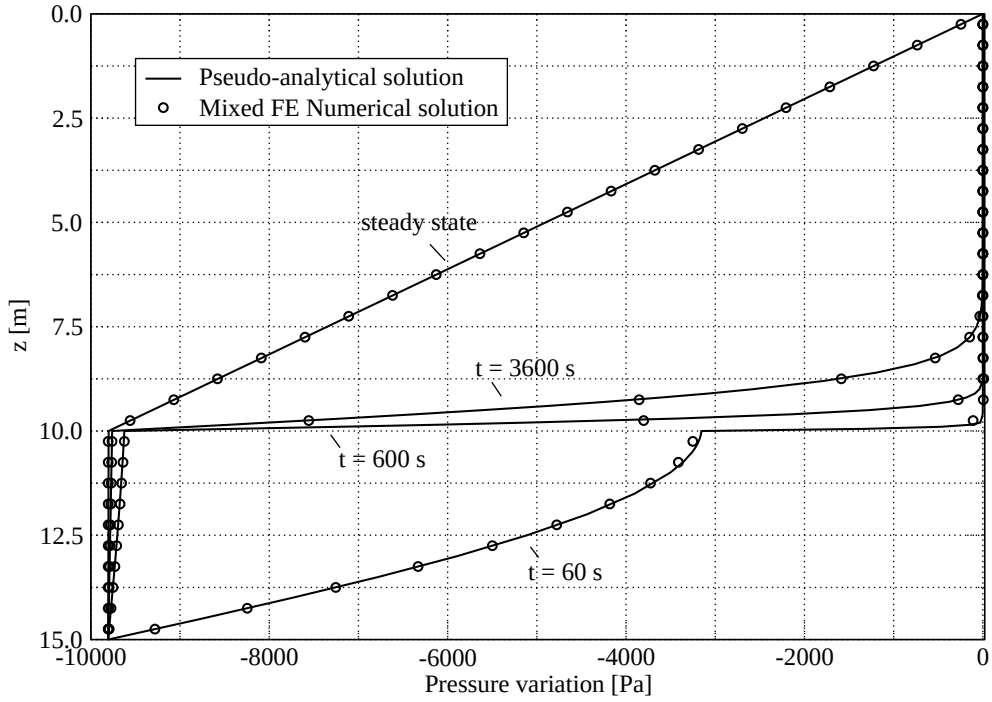

Figure 3.7: Heterogeneous consolidation test: pseudo-analytical and Mixed FE numerical solutions for the pore pressure.

flow [Bergamaschi & Mantica, 1996].

3.3.2 Comparison with standard FEs

The stability of the numerical solution obtained with the Mixed FE model is investigated in a second test problem. The porous column of Figure 3.1 is now assumed to be heterogeneous, with 10 m of clay on top and 5 m of sand on bottom. The clay permeability is 1000 times smaller than sand (Table 3.2) while the elastic properties are the same. Drainage is allowed for also on the bottom boundary where a pore pressure variation of 9810 Pa is prescribed. The top boundary is now traction-free. The computational grid is the same as in Figure 3.1.

The simulated pore pressure at different times is shown in Figure 3.7. The pseudo-analytical solution has been obtained by progressively refining the tetrahedral mesh until convergence. The numerical solution is close to the pseudo-analytical one and appears to be quite stable, with no oscillations at the sand-clay interface. For the sake of a comparison, Figure 3.8 provides the pore pressure solution simulated by a standard FE model based on the same mesh and equal order pressure and displacement approximations. Even in this simple problem, standard FEs exhibit pronounced initial pressure oscillations

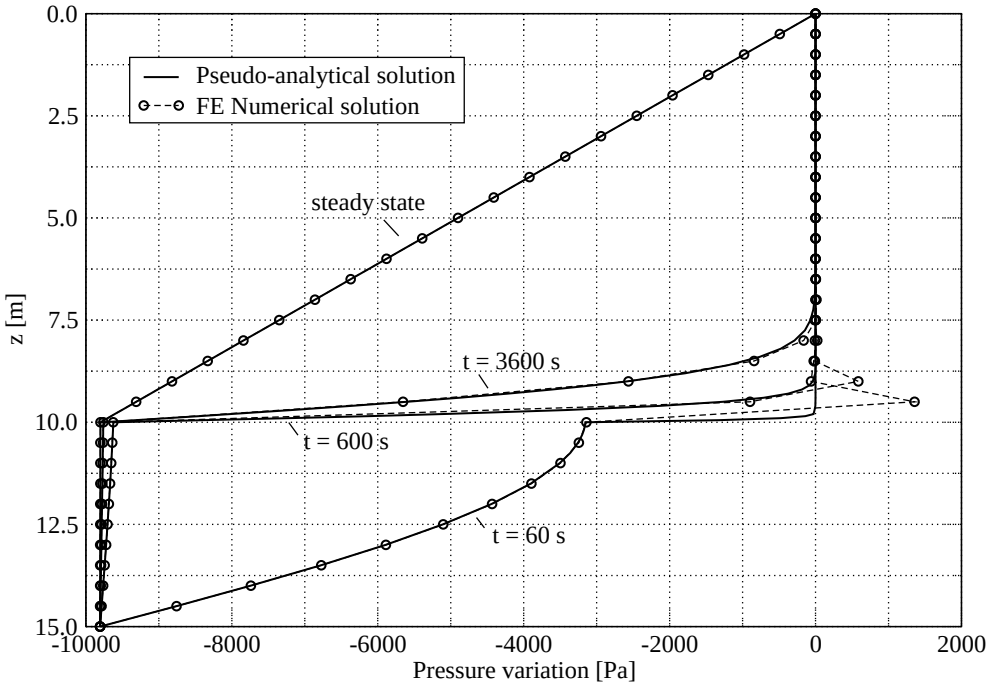

Figure 3.8: Heterogeneous consolidation test: pseudo-analytical and standard FE numerical solutions for the pore pressure.

at the sand-clay interface. By contrast, the vertical displacement is stable and accurate in both the FE and Mixed FE models (Figure 3.9).

The stable pore pressure solution provided by the Mixed FE model is obtained at the cost of a larger number of unknowns. To have an idea, the standard FE model has 837 and 279 displacement and pressure unknowns, respectively, while the Mixed FE model totals 837, 720 and 1,688 unknowns for displacement, pressure and velocity, respectively, with an overall system size equal to 3,245. However, if the tetrahedral mesh is regularly refined so that the standard FE system size is three times larger, oscillations in the pore pressure solution do not vanish, although they are less pronounced than before (Figure 3.10). To have practically insignificant oscillations ($\leq$ 50 Pa) the mesh size h at the sand-clay interface must be $\leq$ 5 cm.

3.4 Conclusions

A fully coupled 3D Mixed FE model for the simulation of Biot consolidation has been developed with the aim at alleviating the oscillations of the pore pressure solution along the interface between materials with different permeabilities at the initial stage of the process. A linear piecewise polynomial and the lowest order Raviart-Thomas mixed space

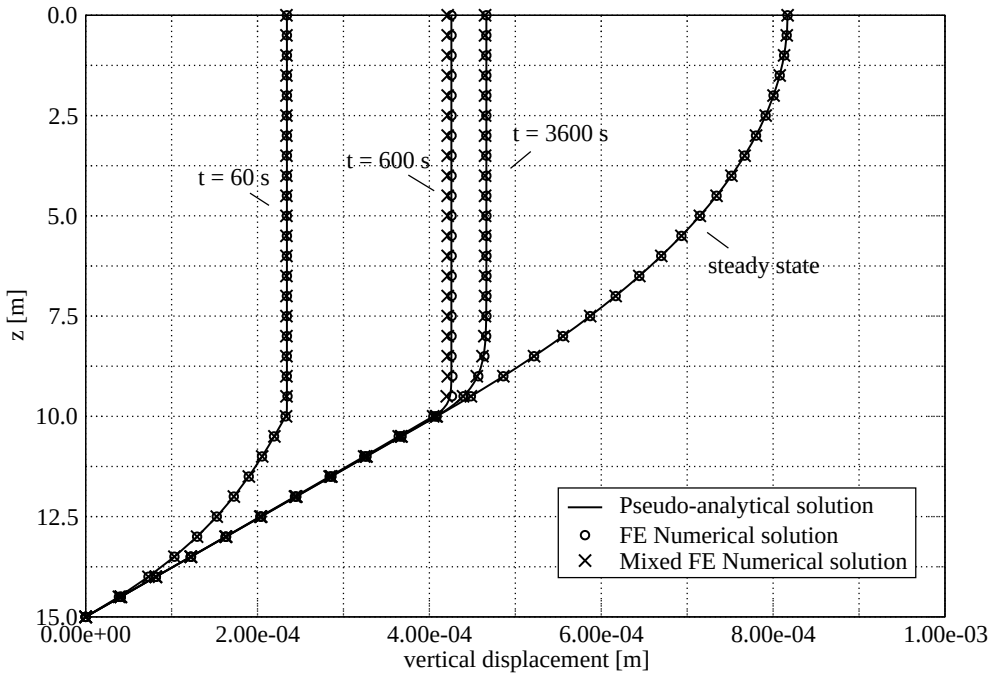

Figure 3.9: Heterogeneous consolidation test: pseudo-analytical and numerical solutions for t

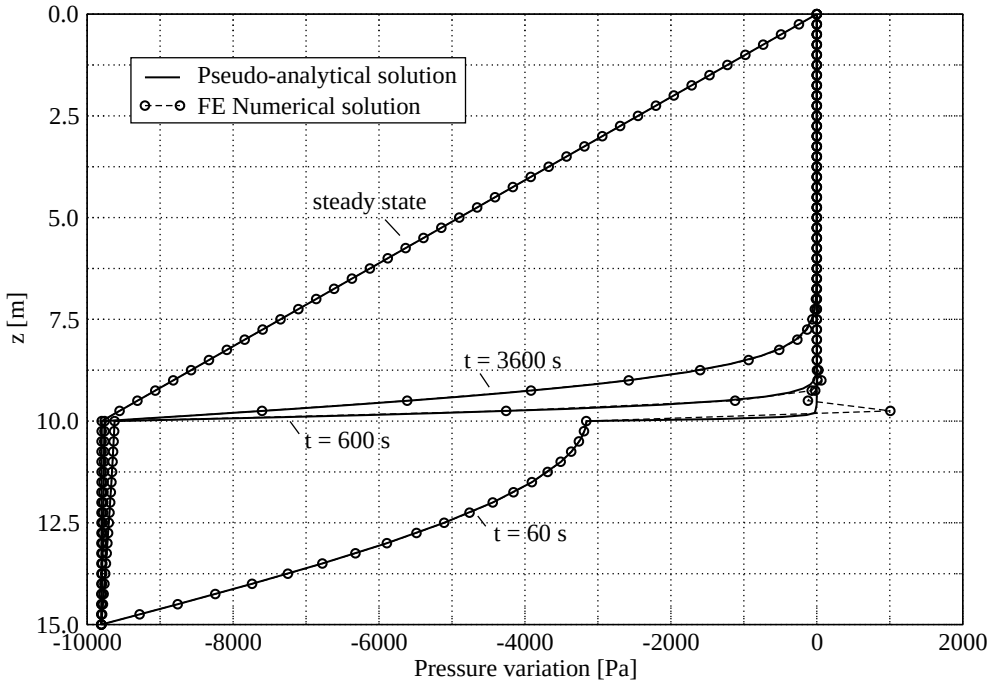

Figure 3.10: Heterogeneous consolidation test: pseudo-analytical and standard FE numerical solutions for the pore pressure on a regularly refined tetrahedral mesh so that the total number of unknowns equates that of the Mixed FE model.

are selected to approximate the medium displacement and the fluid flow rate, respectively. The numerical solution is obtained with an ad hoc algorithm that takes advantage of the block structure of the algebraic linearized system. The numerical model is validated against the well-known Terzaghi's analytical solution and then compared to standard FEs. The following results are worth summarizing:

- the Mixed FE formulation is element-wise mass conservative and preserves the practical advantage of using low-order interpolation elements for the medium displacement as well;
- the solution algorithm addresses the problem in a fully coupled way, thus improving the stability and avoiding the convergence issues that may arise in a sequential approach;
- the Block CP-SQMR algorithm appears to be a robust and efficient tool for the fully coupled solution even though the system conditioning gets worse as the element spacing decreases and the time integration step increases;
- as compared to standard FEs, the Mixed FE model appears to be numerically more stable, with no pressure oscillations at the interface between hydrologically heterogeneous media although a coarse discretization and an equally accurate approximation for displacement are used.

Chapter 4

Realistic applications in the Venice Lagoon

4.1 Introduction

The city of Venice and the surrounding Lagoon sites are periodically plagued by the "acqua alta" phenomenon, i.e. high tide flooding occurring typically in fall and winter due to a combination of low atmospheric pressure, strong on-shore winds from the Adriatic Sea and heavy rain. Floodings have increased in frequency and intensity since early 1900's mainly because of three reasons (Figure 4.1): the eustatic rise of the sea level, the natural land subsidence, and the man-induced land subsidence produced by water pumping. Water extraction in the Venice and Mestre area stopped in the mid 1970s, and, after a slight rebound, subsidence recovered its natural trend. Widely accepted estimates set at 0.23 m the land settlement with respect to mean sea level. According to the updated elevation map of Venice[1], the normal tide height ranges from -0.50 m to +0.80 m with respect to Punta della Salute datum, located opposite St.Mark's Square. Above the +0.80 m threshold, flooding takes place. For example, nearly 30% and more than 60% of the city area is flooded when tide height exceeds +1.20 m and +1.50 m, respectively.

The Italian government has point the Venice safeguarding as a matter of "priority national interest" after the devastating flood of November 1966, when the tide reached a height of 1.94 m above the tidal datum. Several solutions have been advanced to prevent Venice from drowning. The final project selected for the Venice safety is the "MOdulo

[1] "Venezia altimetria", aggiornamento 2009. A cura di L. Boato, P. Canestrelli, L. Facchin e R. Todaro. **Comune di Venezia - Istituzione centro previsioni e segnalazioni maree** in collaborazione con **Insula** spa (in Italian).

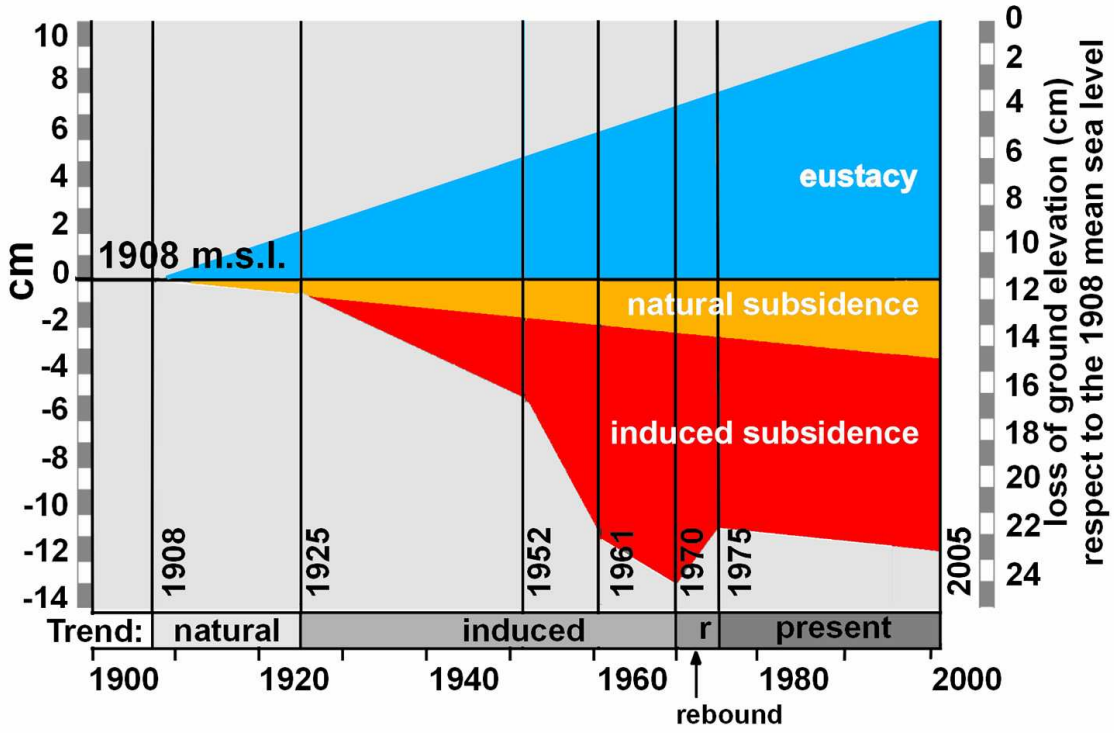

Figure 4.1: Loss of ground elevation (cm) with respect to the 1908 mean sea level during the last century. The blue region depicts the eustatic rise of the sea level. The subsidence trend is divided into the natural (in yellow) and the induced (in red) contribution, respectively [Carbognin *et al.*, 2005].

Sperimentale Elettromeccanico" (MOSE) mobile barriers system, which is currently currently under construction. The MOSE system uses fold-away steel gates that are raised from the sea floor to prevent water from entering the Venice lagoon when a high tide is expected. The floodgates are normally folded and embodied in concrete caissons buried at the bottom of the three lagoon inlets, i.e. Lido, Malamocco, and Chioggia. When tides higher than +1.1 m are expected, thus involving a flooding over about 14% of the city area, the mobile gates rise and isolate the lagoon environment from the Adriatic Sea as long as the sea level drops. Another flood prevention measure, known as the "Insulae" project, consists in raising the elevation of banks, pavements and sidewalks in selected areas, like St. Mark's Square [Burghignoli *et al.*, 2007], to prevent any flood caused by tides within +1.00 m.

A novel proposal to mitigate flooding is the anthropogenic uplift of the city by deep seawater injection recently advanced by Comerlati *et al.* [2004]. Such a proposal is intended as a complementary action to MOSE, since it might prolong its operational life considering the expected sea level rise of the next century, and at the same time reduce significantly its activation, thus limiting concerns at both an economic and environmental level. A pilot injection has been also designed to test the feasibility of the uplift, improve the knowledge of the subsurface below the Venice Lagoon and help the calibration of the full scale prediction models [Castelletto *et al.*, 2008]. In the sequel a review of the pilot project is provided. Then, the numerical approaches presented in Chapters 2 and 3 are tested in several large size realistic and computationally challenging applications using both a stratigraphic sequence typical of the geological basin underlying the Venice lagoon and the most recent available hydrogeological, geothermal and geomechanical data. The 3-D Mixed FE model is employed to address the consolidation of a shallow formation due to the construction of a trial embankment, such as the temporary facilities built at the inlets of the Venice lagoon during the MOSE construction, and the groundwater withdrawal from a confined aquifer. The problems above are also representative of in situ tests to assess the stress-strain properties of the heterogeneous lagoon soils [Simonini *et al.*, 2006] (the former) and characterize the hydraulic properties of an aquifer (the latter). Afterwards, the proposal by Castelletto *et al.* [2008] is supplemented with the investigation of the role played by a temperature variation should the seawater injection take place in non-isothermal conditions. The 3D non-linear hydro-thermo-mechanical model described in the previous Chapters is used, with lowest order Mixed Hybrid Finite Elements (MHFEs) and Finite Volumes (FVs) for the coupled subsurface fluid flow and heat transfer, and Finite Elements (FEs) for the structural equilibrium.

4.2 The pilot project of Venice uplift

Land subsidence caused by fluid withdrawal from subsurface has been experienced worldwide over the past century. A possible mitigation to such an occurrence can be obtained by the injection of fluids underground. Subsurface fluid injection is a well-known technique in the petroleum industry and has been used in the last 40-50 years for different purposes, with facilities discharging a variety of fluids into more than 400,000 injection wells across the United States alone [USEPA, 2002]. Although the technology is well-known, fluid injection has seldom been used for the purpose of raising subsiding areas, and therefore measurements of anthropogenic uplift are not generally planned. Two documented examples are the pumping of salt water into the subsurface formations at Long Beach Harbour, California, and the artificial recharge in the Las Vegas Valley, Nevada. As to Long Beach, during the oil production period in the 1950s a maximum 8.5 m settlement was recorded [Poland and Davis, 1969], while the injection program induced a modest observed rebound of 10 cm along the front pier in the San Pedro Bay [Rintoul, 1981], with a maximum local uplift of 33 cm from 1958 to 1975 [Kosloff *et al.*, 1980]. In Las Vegas, recent satellite maps show that the artificial recharge, started in the late '80s to partially compensate the groundwater level decline due to aquifer over-exploitation, has succeeded in mitigating the produced land subsidence, with a maximum seasonal uplift of more than 3 cm recorded during the 1997-1998 winter [Hoffman *et al.*, 2001]. The lack of uplift data is also due to the fact that most fluid injection projects, in particular the ones for enhancing oil recovery (EOR), occur in desert areas where traditional geodetic levelling is not usually performed. It is only very recently that technology from space, such as GPS (Global Positioning System) and especially InSAR (Interferometric Syntetic Aperture Radar), allows for the inexpensive and accurate detection, also in non-urban land by the use of ad hoc reflectors, of small displacements (on the order of 1-2 mm/year) that can be easily related to fluid injection. In fact, field measurements from satellite data provide documentary evidence that pumping fluid underground has indeed produced a measurable anthropogenic uplift [e.g. Bilak *et al.*, 1991; Wang and Kry, 1997; Hoffman *et al.*, 2001; Dusseault and Rothenburg, 2002; Collins, 2005]. Using satellite interferograms, an uplift of 29 cm caused by steam injection at the Cold Lake, Alberta, Canada, over less than a 3-month period was measured by Stancliffe and van der Kooij [2001], and even larger uplifts in steam-assisted gravity drainage projects may be expected [Davari, 2007]. The experiences above suggest that injecting water below the Venice lagoon can lead to an appreciable rebound of the city and represent a potential remedy to the settlement

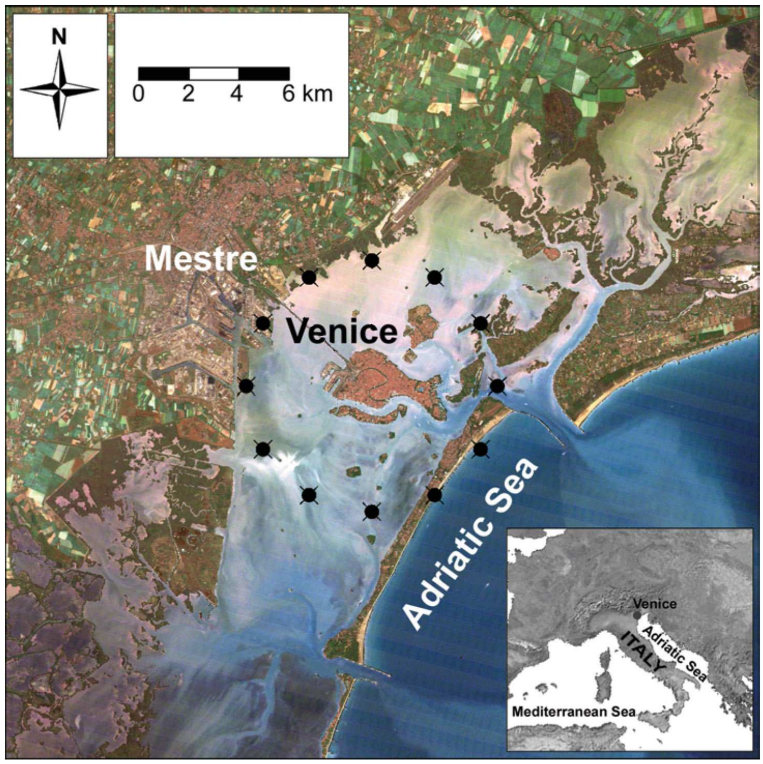

Figure 4.2: View of the Venice Lagoon with black dots denoting the seatwater injection wells. The two inlets of Lido (upper) and Malamocco (lower) are shown [Comerlati *et al.*, 2003].

already experienced.

The first idea to raise Venice was advanced by Comerlati *et al.* [2003], predicting an uplift of 30 cm due to saltwater injection through 12 injection wells (Figure 4.2) in 10 years on the basis of hydrogeological and geomechanical models. In 2004, based on more recent geological, litho-stratigraphical, hydrological and especially geomechanical data from the Northern Adriatic basin which comprises the lagoon subsurface [Baù *et al.*, 2002; Ferronato *et al.*, 2003a,b; Ferronato *et al.*, 2004], the Comerlati *et al.* [2003] modelling study was refined, with a 25 cm most-likely uplift estimate, comprised between a 40 cm upper and a 11 cm lower bound, respectively [Comerlati *et al.*, 2004]. It is worth noting that an upheaval of 25 cm would have precluded most of the flooding occurred from 1872 to 2002 [Comerlati *et al.*, 2004], and meanwhile would offset the 27 cm expected Northern Adriatic level rise over the XXI century as predicted in a pessimistic scenario by CORILA [1999], a consortium of universities and research institutions charged with coordinating the research activities in the Venice Lagoon. Another paper by Comerlati *et al.* [2006] addresses the option of storing anthropogenic CO_2 underneath the Venice Lagoon, but

the related uplift would be more modest than that obtained by injecting saltwater, and the success of the operation is more uncertain because of the great complexity affecting the overall CO_2 sequestration process.

In view of the precarious lagoon environment and the great artistic heritage of the city of Venice, anthropogenic uplift by seawater injection requires an extremely detailed knowledge and accurate prediction of the actual subsurface response to the designed pumping. In this respect Castelletto *et al.* [2008] advanced the plan of a preliminary pilot project so as to:

- ascertain whether water injection in deep geological formations below the lagoon can indeed help raise Venice, as predicted with the aid of the preliminary modelling analyses [Comerlati *et al.*, 2003, 2004];
- improve the geological and litho-stratigraphical representation of the lagoon subsurface down to the depth of interest;
- calibrate the hydrological and geomechanical models improving their predictive capabilities;
- monitor the land motion in time and space using the most advanced satellite technology, providing a real time control on the ongoing process and allowing for a timely arrest of the injection in case of unexpected unsafe conditions.

4.2.1 Experiment design

The pilot project will affect a limited underground volume that has to be nevertheless representative of the Venice subsurface, raising no concerns among the people living in the experimental site nor jeopardizing the activity that is normally performed there. A preliminary design of the injection wells and observation boreholes is shown in Figure 4.3. Three wells from where saltwater is pumped underground are located at the vertices of a regular triangle with 800-1000 m-long sides and drilled down to a depth of about 800 m. Each single well will inject the minimum pumping rate that is required to produce a measurable yet fully safe uplift at any time of practical interest within the 3-year duration of the experiment. The injection rate will be adjusted accordingly with the aid of numerical analyses to obtain a maximum uplift at the end of the experiment of about 7 cm. The final size and layout of the injection wells and observation boreholes will be based on the actual geology of the subsurface and the logistic constraints dictated by the selected site.

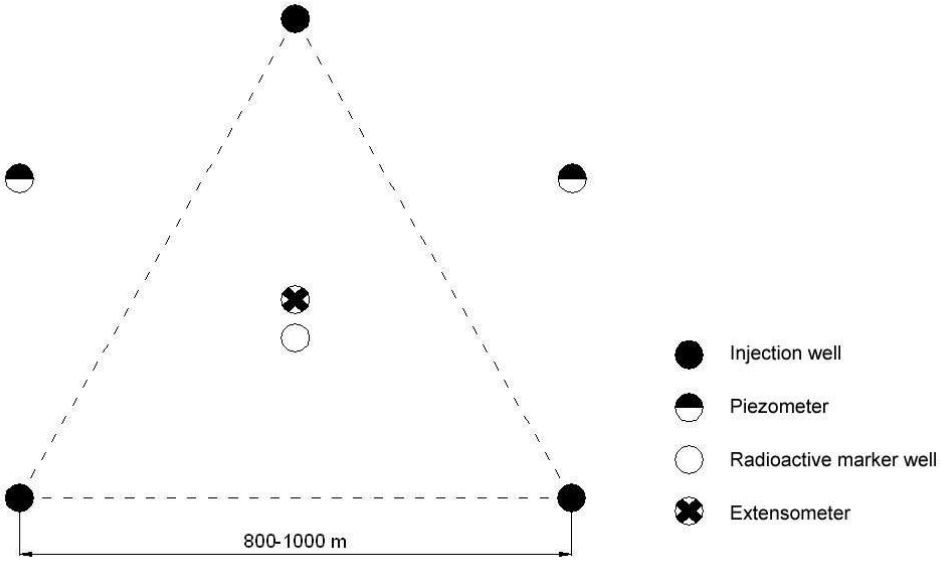

Figure 4.3: Layout of the injection wells and other instrumented boreholes.

During the injection a number of variables are to be continuously monitored, namely:

1. the pore water overpressure in both the injection wells and the piezometric holes;

2. the injection rate from each individual well;

3. the deformation of the injected formation and overlying clay layer as monitored with the aid of the radioactive marker technique;

4. the compaction, if any, of the upper fresh water aquifer system as monitored with the aid of an extensometer;

5. the land surface (horizontal and vertical) motions as monitored by the use of the remote sensing technologies (GPS and InSAR).

The pore water pressure in the injection wells will be directly recorded by an appropriate equipment commonly used in petroleum engineering. The final setup is completed by two additional boreholes instrumented with deep piezometers located by the pilot site (Figure 4.3) monitoring the aquifer pressurization, an extensometer [Heywood, 1995] installed in the center of the experimental area measuring the porous medium deformation in the upper 400-500 m, and a borehole drilled to implement the marker technique and simultaneously measure in situ pore water pressure. The radioactive marker technique

[Mobach and Gussinklo, 1994; Ferronato *et al.*, 2003a,b] in the central borehole will allow for deriving the most updated and representative estimate of rock compressibility in unloading conditions (II cycle) by recording the local in situ expansion.

4.2.2 Site selection

The experimental site selection relies on both geological and logistical considerations. From the geological viewpoint, the aquifer where seawater is injected should be a continuous formation underlying the entire lagoon and should coincide with the formation under consideration for the full-scale project of Venice uplift. Moreover, it is fundamental that the confining unit or caprock have adequate thickness and ideally not be affected by faulting or fractures. From the logistical viewpoint, the selected area must fulfil a number of safety requirements, e.g. its ground elevation should be such to avoid any risk of flooding due to likely events of "acqua alta" during the experiment, and should be far enough from vulnerable sites (e.g. industries, villages or sensitive areas) that could be potentially damaged should the experiment evolve differently than planned. Easy and economic accessibility by trucks to the site in order to both install and remove the experimental equipment, along with the availability of the injected water at a relatively small distance from the lagoon should be ensured. An ad hoc treatment plant for geochemical compatibility must be also planned. According to the above requirements, Castelletto *et al.* [2008] selected four potential sites as indicated in Figure 4.4, namely Le Vignole island, San Giuliano, Fusina and Cascina Giare.

4.2.3 Geoseismic analyses

The geological model by Comerlati *et al.* [2003, 2004] is based on a 3D deep seismic survey performed by ENI-E&P in the Northern Adriatic, the lithology of the exploratory boreholes Venezia 1-CNR, Chioggia Mare 3 and Chioggia Mare 4, and the fresh-water multiaquifer system in the upper 400 m depth as reconstructed in previous studies of anthropogenic land subsidence of Venice [Gambolati *et al.*, 1974]. Improvement of the current knowledge on the geology and litho-stratigraphy underneath the Venice Lagoon is a basic requirement for both the selection of the pilot project location and the proposed full-scale project of anthropogenic Venice uplift. In order to integrate the existing available information, an ad hoc seismic survey is planned in the lagoon focusing the zone between 500 and 1000 m depth. Figure 4.4 shows a preliminary programme of the two-dimensional seismic lines to acquire new geological data. The survey consists of about 90

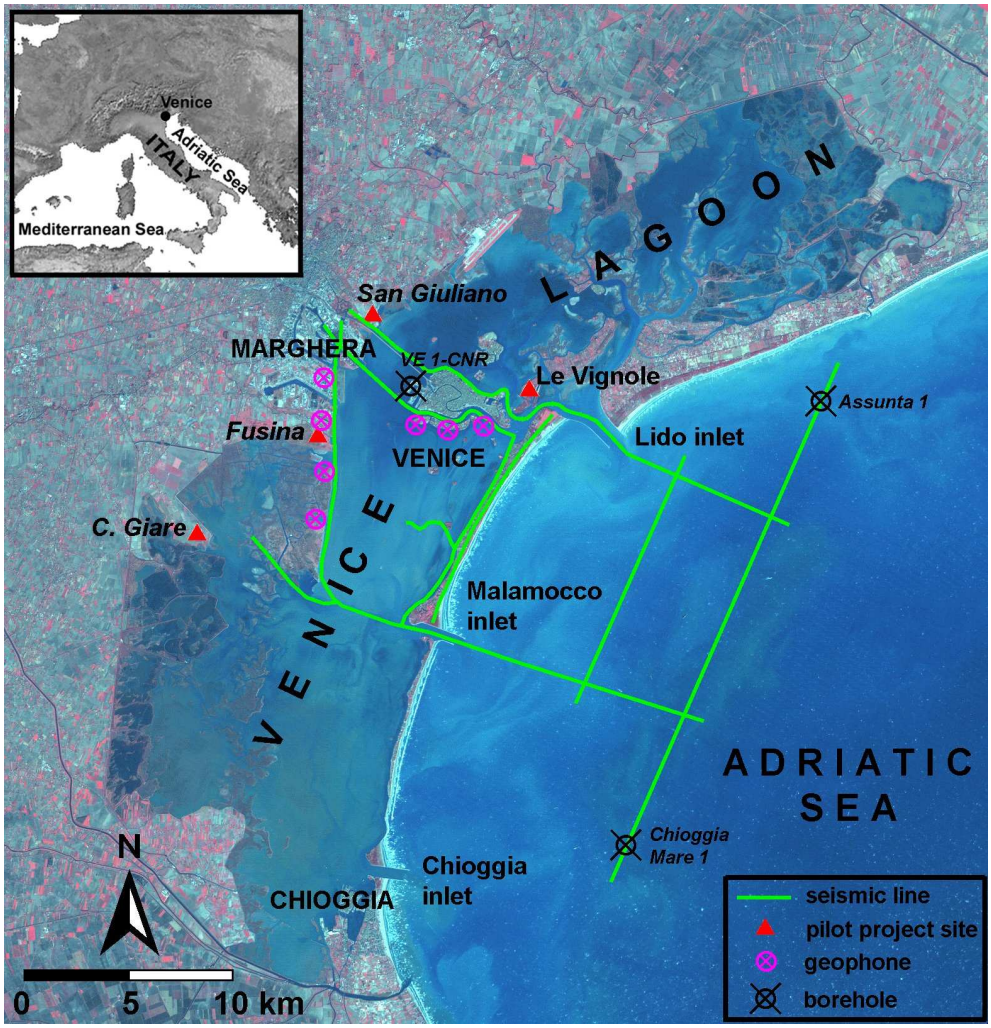

Figure 4.4: Image of the Venice Lagoon showing the possible location of the four sites where to implement the pilot project (Le Vignole, S. Giuliano, Fusina and Cascina Giare) along with the seismic profiles planned to improve the present knowledge of the geology and litho-stratigraphy of the lagoon subsurface.

km-long marine acquisitions and 10 km-long land acquisitions. The seismic survey will be calibrated using the Venezia 1-CNR sequence and a number of lines outside the lagoon crossing the exploratory boreholes Chioggia Mare 1 and Assunta 1 (Figure 4.4).

In areas of particular interest, e.g. in the expected pilot experimental site, the two-dimensional seismic survey should be integrated with in situ geophysical measurements such as well logs, cross-well seismic, laboratory experiments on water and soil samples cored from ad hoc exploratory boreholes.

The outcome of the new seismic investigations will be supplemented with the seismic data acquired by ENI-E&P off-shore in the Adriatic Sea facing the lagoon over the 1990s and on-shore, in the lagoon surroundings, over the 1950s-1980s. The data integration will allow for accurately mapping the depth and thickness of the sandy formations potentially suited for seawater injection and the clayey caprock sealing the aquifer.

4.2.4 Prediction of uplift

The experiment has been simulated numerically using the 3D non-linear FE models of subsurface water flow and land uplift developed by Comerlati *et al.* [2004]. Non-linearity is accounted for by aquifer elastic storage and rock compressibility both of which vary with the in situ effective intergranular stress, hence the pore water overpressure. The lagoon subsurface is known to be normally pressurized and consolidated, at least down to 1000 m depth [Teatini *et al.*, 2000]. The volume of the porous medium has been discretized into linear tetrahedral elements forming a cylinder with a 10-km radius bounded on top by the ground surface and on bottom by a 5 km-deep fixed basement. Because of the limited time interval of the simulation, boundary conditions of zero overpressure and displacement are prescribed everywhere, except at the land surface where a traction-free plane is assumed. A horizontally layered litho-stratigraphy for the injected formation and overlying caprock based on the Tronchetto VE-1 borehole [Gatto & Mozzi, 1971] and the geological reconstruction of Comerlati *et al.* [2004] is used (Figure 4.5), while the upper fresh water aquifer-aquitard system is vertically similar to the one underlying Venice [Gambolati *et al.*, 1974].

To provide an order of magnitude prediction of the expected 3-year time and space distribution of uplift, the parameters of the baseline case as discussed by Comerlati *et al.* [2004] have been implemented into the pilot project model, in particular the hydraulic conductivity and the uniaxial vertical rock compressibility are reported in Table 4.1 and Figure 4.6, respectively. Based on actual field measurements from markers installed in

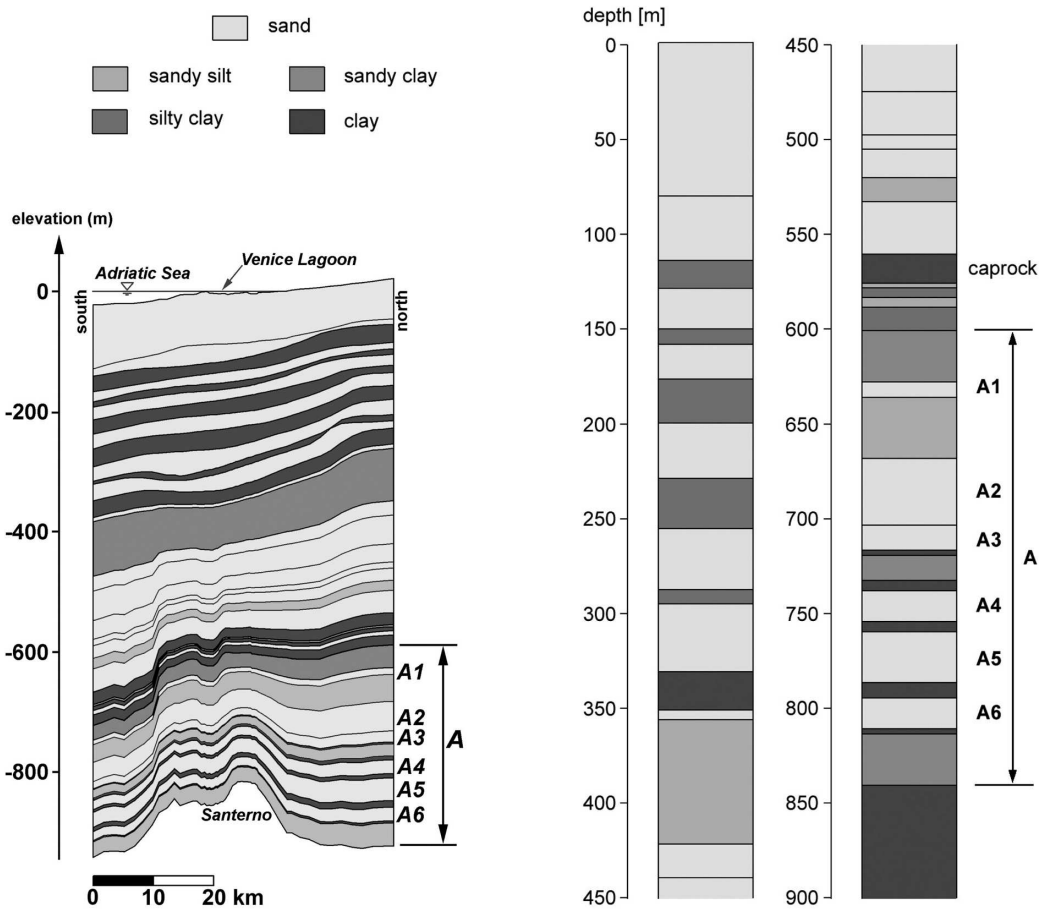

Figure 4.5: Representative litho-stratigraphy of the brackish aquifer unit subdivided into 6 injected subunits and overlying layers as reconstructed below Venice by Comerlati *et al.* [2003, 2004] (left) and horizontally layered litho-stratigraphy used by Castelletto *et al.* [2008] (right).

Symbol	Quantity	Value	Unit
K_{A1}	Hydraulic conductivity of unit $A1$	$2.7{\cdot}10^{-6}$	m s^{-1}
K_{A2}	Hydraulic conductivity of unit $A2$	$2.7{\cdot}10^{-6}$	m s^{-1}
K_{A3}	Hydraulic conductivity of unit $A3$	$1.5{\cdot}10^{-6}$	m s^{-1}
K_{A4}	Hydraulic conductivity of unit $A4$	$2.7{\cdot}10^{-6}$	m s^{-1}
K_{A5}	Hydraulic conductivity of unit $A5$	$2.7{\cdot}10^{-6}$	m s^{-1}
K_{A6}	Hydraulic conductivity of unit $A6$	$2.7{\cdot}10^{-6}$	m s^{-1}
K_{clay}	Hydraulic conductivity of clay	10^{-10}	m s^{-1}

Table 4.1: Summary of the hydraulic conductivity property used by Comerlati *et al.* [2003, 2004] in the baseline case and by Castelletto *et al.* [2008].

deep Northern Adriatic boreholes, compressibility in expansion was assumed to be 3.5 times less than its value in compression [Ferronato *et al.*, 2003a; Comerlati *et al.*, 2004].

A constant rate Q equal to $12{\cdot}10^{-3}$ m^3/s of saltwater was continuously injected into each well and partitioned into the six subunits displayed in Figure 4.5 on the basis of the respective hydraulic transmissivity. The results of the simulation were superposed on each of the four candidate sites. Figures 4.7a and 4.7b show the pore water overpressure and the land uplift, respectively, for the Fusina site predicted at the completion of the experiment, i.e. three years after starting the injection. The largest overpressure and uplift are obtained at the centre of the ideal triangle equating 0.67 MPa and 7.3 cm, respectively. Both the predicted pore overpressure and uplift exhibit a regular distribution in space. Because of the relatively short pilot project duration and the small injected seawater volume, the overpressure does not migrate vertically and remains practically confined within the injected units. Behaviour in time during and after the experimentation is provided in Figure 4.8, including the water pressure rise and decline in one of the piezometers outside the triangle. The injected formation expansion vs. time below the triangle centre is given in Figure 4.8. The maximum expansion has the same order as the largest uplift and should be easily detected and measured quite accurately with the aid of the radioactive marker technique. The largest gradient of the vertical ground displacement is predicted at $2{\cdot}10^{-5}$, i.e. far below the admissible bounds recommended for civil structures [Skempton and McDonald, 1956; Holtz, 1991]. Note that the most severe indications are related to the maximum distortion acceptable for masonry buildings with more than one floor. Based on the presently available knowledge of the subsurface properties, the small strains developed on the ground surface are expected to cause no adverse effects during the experiment. However, should the ground motion be such to

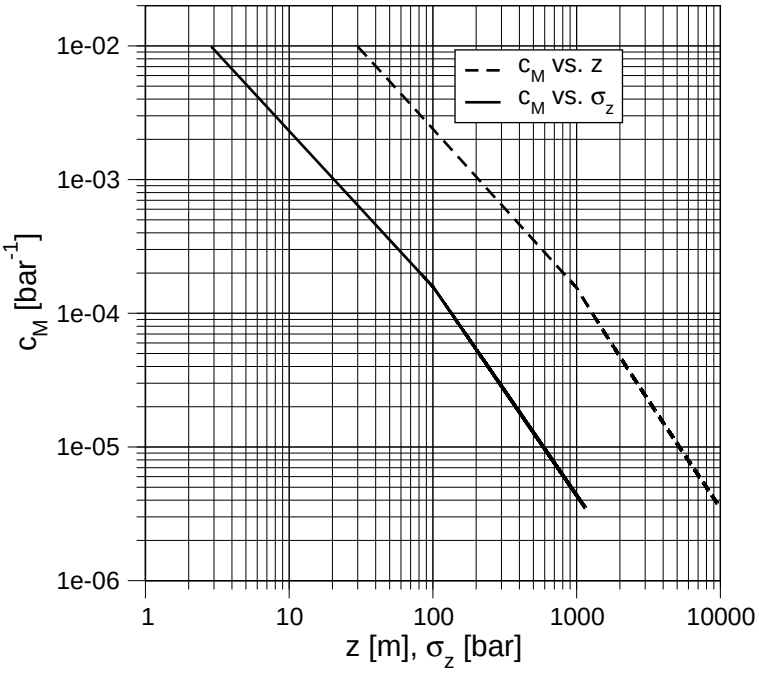

Figure 4.6: Uniaxial vertical compressibility c_M vs. effective stress σ_z and depth z used in the FE model of Venice subsurface by Comerlati *et al.* [2003, 2004] and by Castelletto *et al.* [2008].

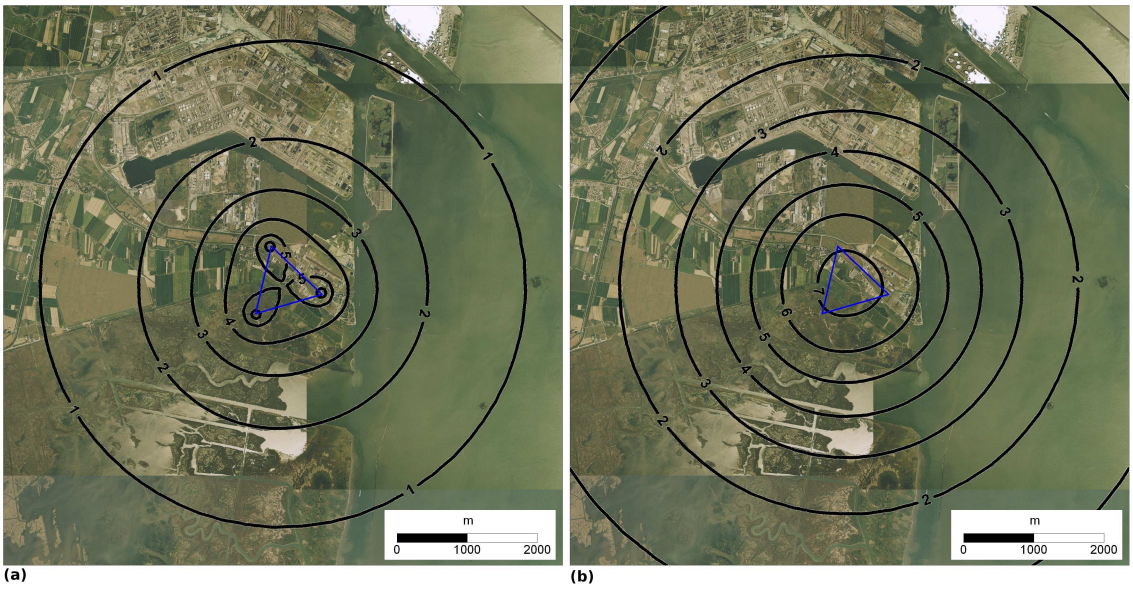

Figure 4.7: (a) Pore water overpressure (bar) averaged over the injected aquifer thickness, and (b) land uplift (cm) at the completion of the pilot project (Fusina site).

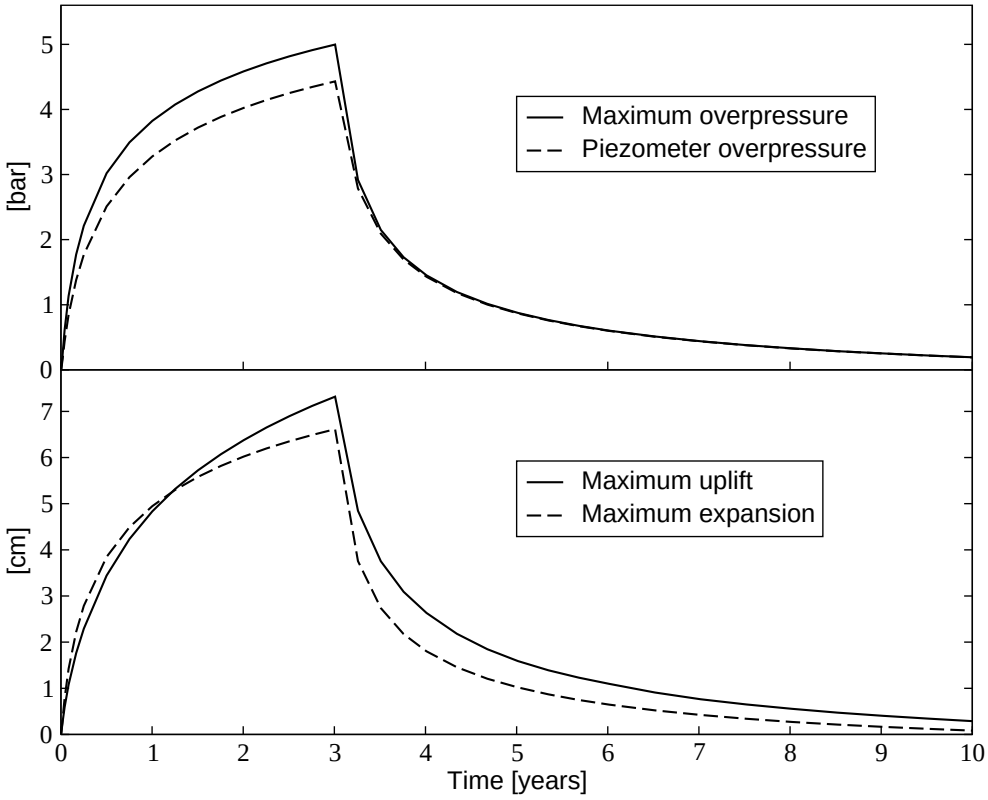

Figure 4.8: Time behavior of pore water overpressure (bar) averaged over the injected aquifer thickness, and land uplift and injected formation expansion (cm) at the center of the ideal injection triangle. The average pore water overpressure in one external piezometer is also shown.

	Clay	Silt	Sand
$K_{xx} = K_{yy}$ [m/s]	10^{-7}	10^{-6}	10^{-4}
K_{zz}/K_{xx}	1	1	0.1
ϕ	0.3	0.3	0.3
β_f [MPa^{-1}]	4.32×10^{-4}	4.32×10^{-4}	4.32×10^{-4}
E [MPa]	2.13	2.13	4.50
ν	0.3	0.3	0.3
b	1.0	1.0	1.0

Table 4.2: Hydro-geological properties of the shallow sediments in the Upper Adriatic basin used in the consolidation examples.

induce a potential risk of earth fissure generation, the real-time deformation monitoring network would help keep such a hazard under a safe control.

4.3 Consolidation examples

The 3-D Mixed FE model has been experimented with in two realistic applications addressing the consolidation of a shallow formation in the geological basin underlying the Venice lagoon, Italy. A cylindrical stratified porous volume made of a sequence of alternating sandy, silty and clayey layers down to 50 m depth is simulated. The hydro-geological properties are summarized in Table 4.2 and are representative of a shallow sedimentary sequence of the upper Adriatic [Teatini *et al.*, 2006; Gambolati *et al.*, 1974, 1991]. The axial symmetry of the model geometry allows for the discretization of one fourth only of the overall porous volume (Figure 4.9) with zero flux and horizontal displacement prescribed on the inner boundaries. The following additional boundary conditions apply: the outer boundary is fixed and drained, the bottom is fixed and impervious, the top is traction-free and drained. As shown in Figure 4.9, a vertically regularly refined grid is used totaling $n_n = 13,356$ nodes, $n_e = 70,080$ elements and $n_f = 143,368$ faces with an overall model size equal to 253,516.

4.3.1 Example 1: consolidation of a trial embankment

A uniform surface load distributed over a circular area centered on the domain top with a 10-m radius is applied. The load is set equal to 8 kN/m^2 and is representative of an artificial embankment similar to that built at the inlets of the Venice lagoon during the MOSE construction. The load is assumed to increase linearly from 0 to 8 kN/m^2 within 3 days and then to remain constant. As the first layer consists of low permeable sediments,

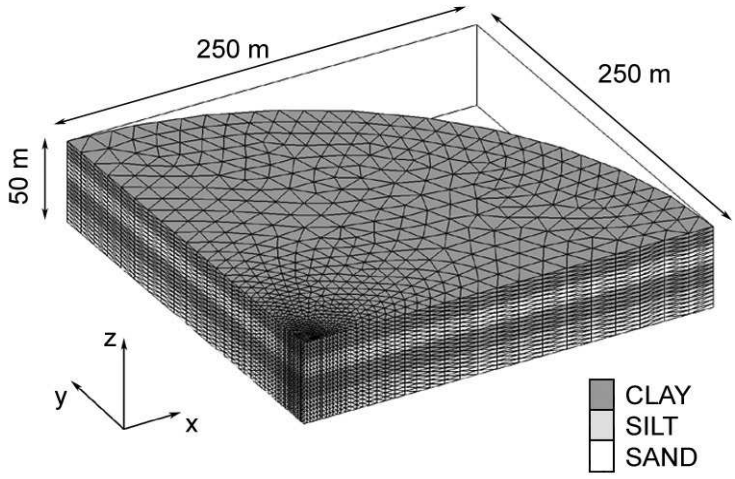

Figure 4.9: Axonometric view of the FE grid used in the consolidation examples.

the pore pressure is expected to initially rise at the load application as a consequence of the almost undrained deformation of the clay. The overpressure gradually dissipates in time, with the dissipation rate depending on sediment thickness and permeability. This is physically related to the zero volume change rate prescribed at the initial time for the porous medium, which represents the main source of instability in the numerical pore pressure solution. Moreover, the induced overpressure is generally pretty small, so reproducing it numerically may be a difficult task.

The overpressure rise and dissipation in time as simulated by the Mixed FE coupled model are shown in Figure 4.10. Despite the small overpressure, no oscillations in the numerical solution are observed. Note the pressure rise simulated in the deepest clay layer as well. As the pore water flows out of the top draining surface the soil consolidates and the ground surface subsides. Figure 4.11 shows the vertical land settlement vs. time in a radial cross-section. After 20 days the overpressure has dissipated almost completely and the displacement approaches the steady state.

4.3.2 Example 2: groundwater withdrawal and the Noordbergum effect

This example allows for testing the ability of the numerical model to simulate one of the most known physical processes accounted for by coupling between fluid flow and soil stress, that is the pressure rise occurring in a low permeable layer confining a pumped formation [Verruijt, 1969]. The phenomenon is called Noordbergum effect by the name of the village

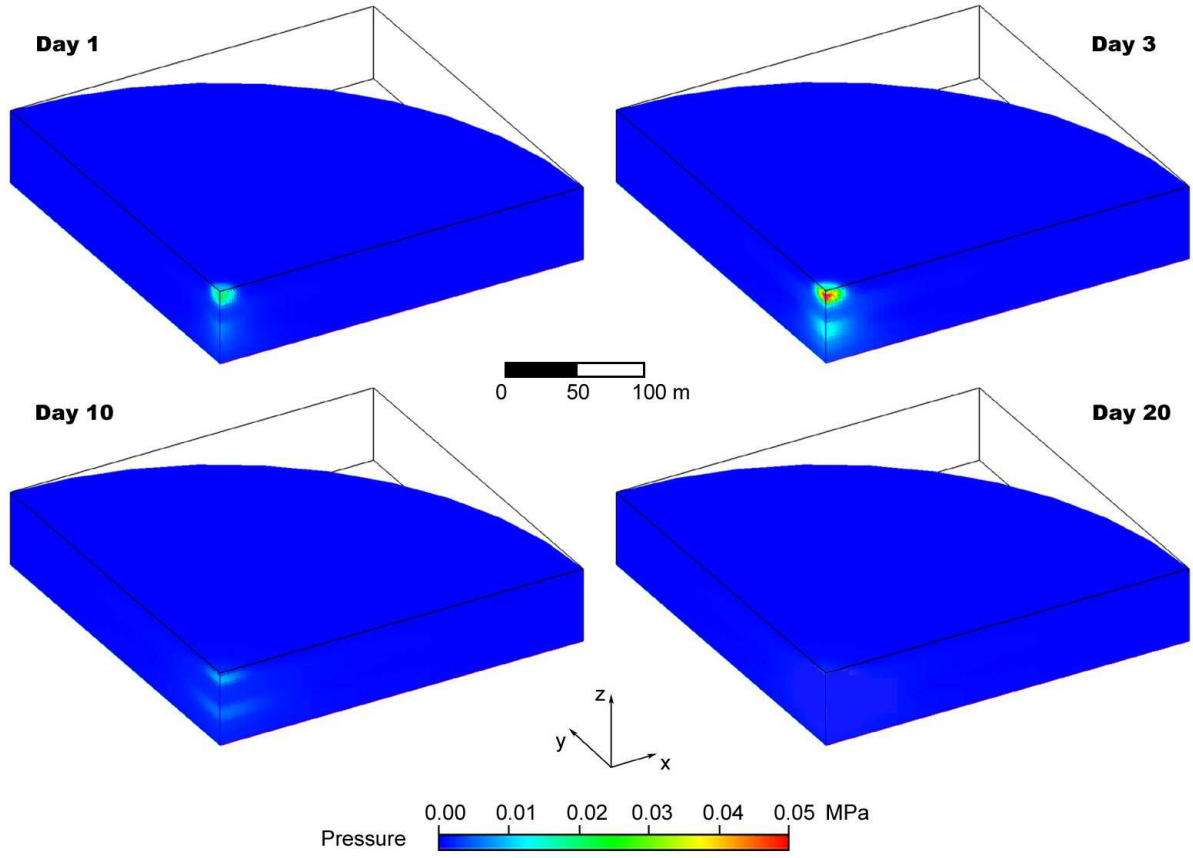

Figure 4.10: Example 1: pore pressure variation vs. time due to the application of a surface load.

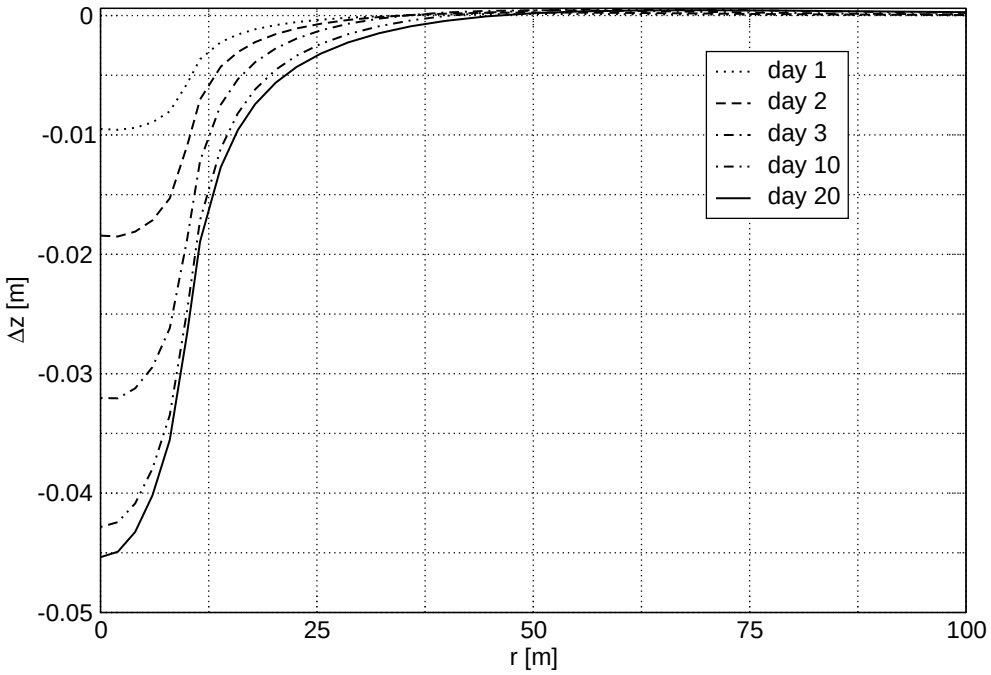

Figure 4.11: Example 1: vertical land displacement vs. time.

in The Netherlands where it was first observed. Because of the small overpressure involved, especially when pumping occurs at a shallow depth, the Noordbergum effect turns out to be quite difficult to simulate numerically in a stable way.

A constant withdrawal rate of 8 l/s is prescribed from the shallowest sandy layer (Figure 4.9) through a vertical well located at the centre of the simulated cylindrical porous volume. The pore pressure in the pumped formation achieves a maximum drawdown of 0.15 MPa 20 days after the beginning of pumping. Figure 4.12 shows the drawdown distribution, while Figure 4.13 provides the related land settlement vs. time along a radial cross-section. To reveal the Noordbergum effect Figure 4.14 provides the numerical pore pressure solution as obtained on a 3-m deep horizontal plane, i.e. in the middle of the upper clay layer. As theoretically expected, the pore pressure increases at the initial stage of pumping with a very small value (about 1 kPa, i.e. more than 100 times smaller than the largest drawdown), then quickly dissipates as the consolidation proceeds. The numerical solution appears to be stable with no oscillations and a good degree of symmetry.

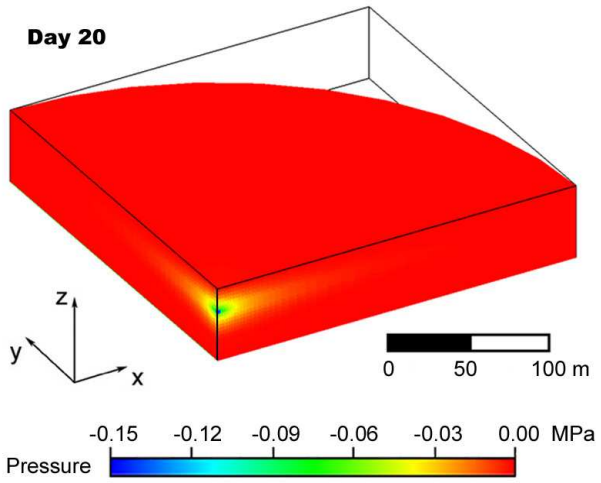

Figure 4.12: Example 2: pore pressure variation 20 days after the start of pumping.

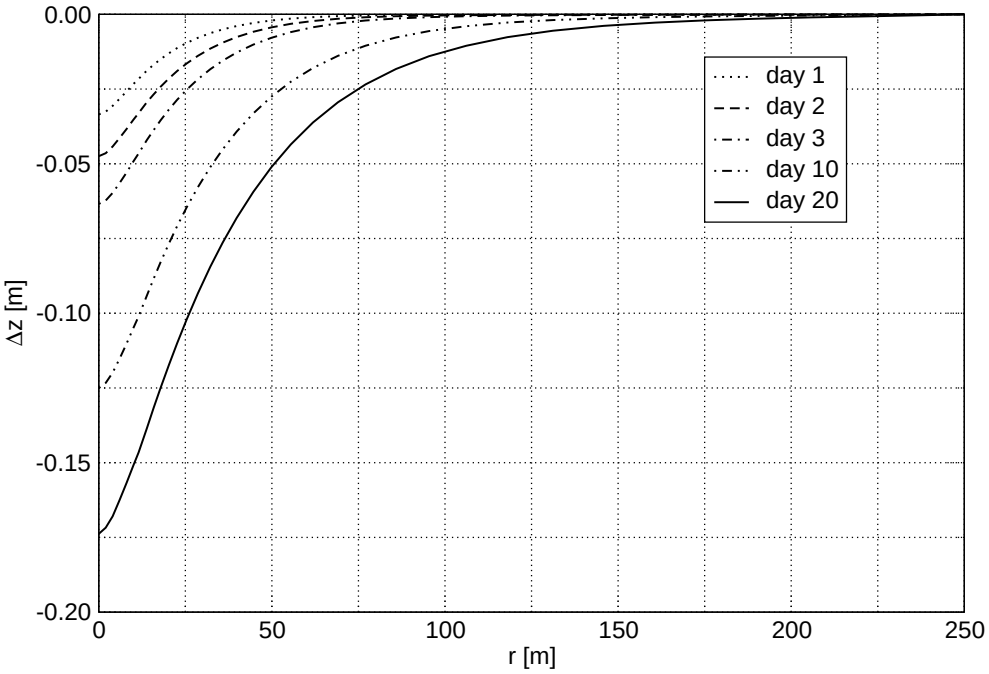

Figure 4.13: Example 2: vertical land displacement vs. time.

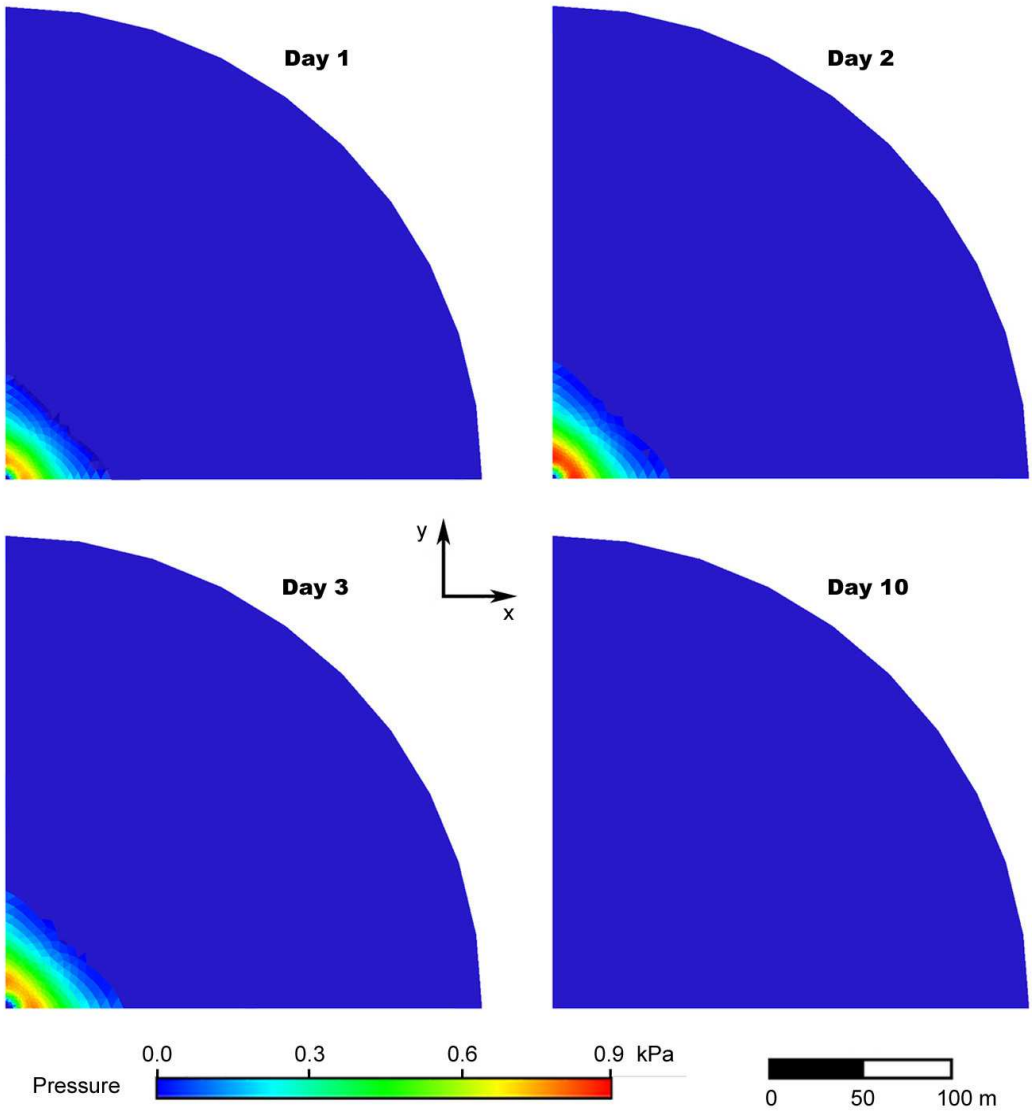

Figure 4.14: Example 2: pore pressure variation vs. time on a horizontal plane located in the middle of the upper clay layer.

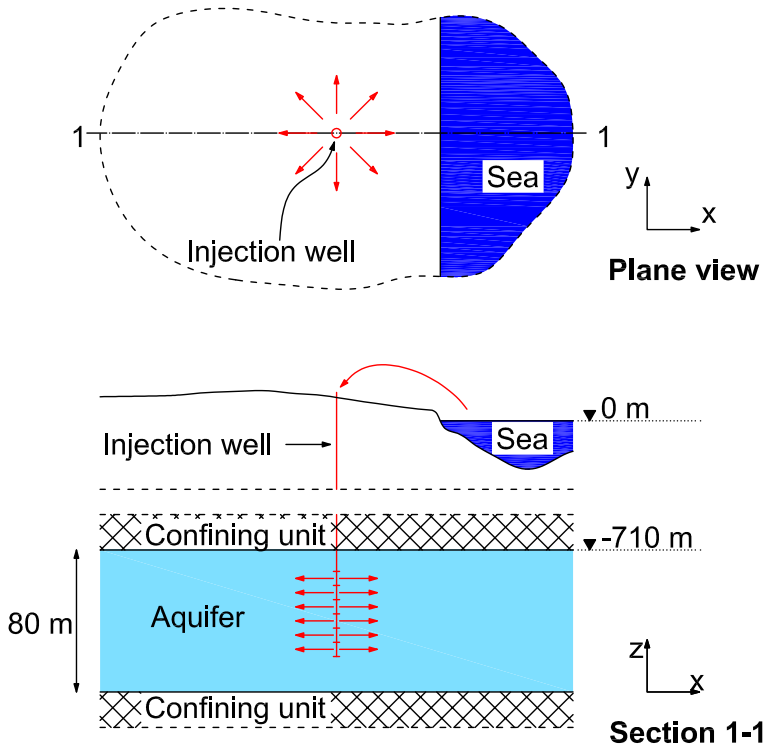

Figure 4.15: Sketch of the integration domain used in the non-isothermal injection simulation. Seawater is injected in a deep formation (*ciano*) confined by clayey units.

4.4 Non-isothermal seawater injection

The thermal effects involved in the pilot project of Venice uplift are investigated by simulating the deformation of a porous volume subject to a pore pressure change induced by deep seawater injection into a brackish aquifer through a single vertical well. The numerical simulations make use of a realistic geological setting representative of the Northern Adriatic basin. The conceptual model consists of a pumped aquifer overlain and underlain by clayey confining beds (Figure 4.15). Because of its axial-symmetry, the problem can be reduced by studying s quarter of the injected porous medium only. The integration domain is discretized by linear tetrahedral elements forming with the well, drawn in red in Figure 4.16, located along a vertical side. The discretized volume covers an area of 10×10 km confined on top by the ground surface and a 10-km deep rigid basement on bottom. The three-dimensional mesh is made of 143,055 nodes and 810,000 tetrahedra. Close to the injection well the average elemental size is equal to 10 m. The boundary conditions are specified far enough from the depleted reservoir in order to avoid any appreciable influence on the results of interest. The ground surface is a traction-free plane

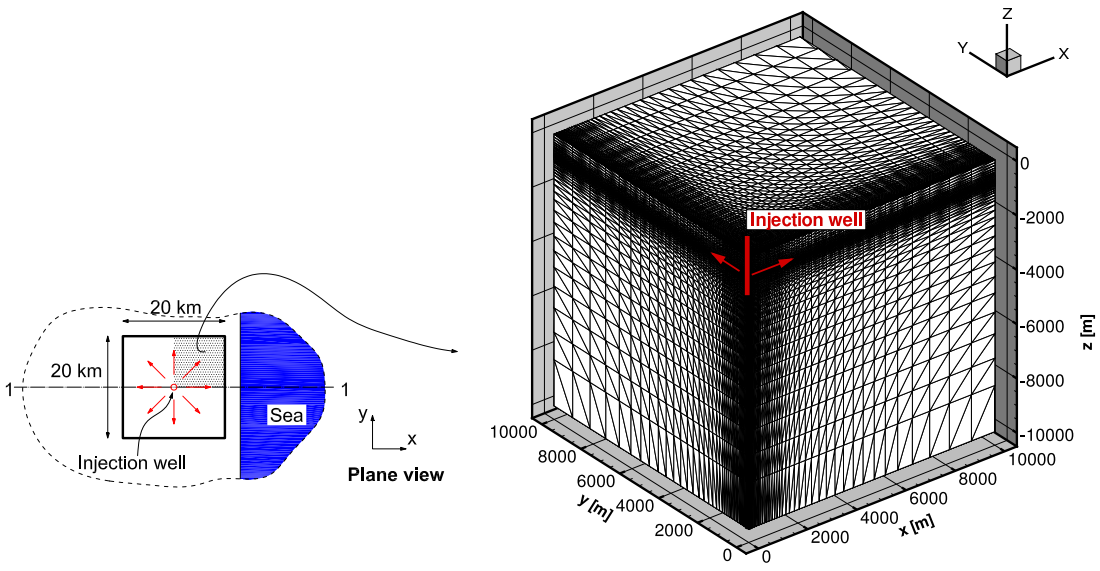

Figure 4.16: Axonometric view of the tetrahedral mesh used to discretize the integration domain.

with zero displacements prescribed on the bottom and outer boundaries. Along the inner boundaries no horizontal displacements are allowed for. The basement and the inner boundaries are impermeable to fluid flow and adiabatic, while the ground surface and the outer boundaries are fixed for both pore pressure and temperature. The injected aquifer has a constant thickness of 80 m and is ideally located between 710 and 790 m below the sea level (Figure 4.15). The initial pressure is hydrostatic, while the initial temperature distribution is given by:

$$\theta_{in} = \theta_{surf} + g_t z \tag{4.1}$$

where g_t is the thermal gradient in [°C/m] and θ_{surf} the surface temperature. The average value of g_t is usually equal to 0.029 °C/m. However, experimental measurements and geological considerations [Mattavelli and Novelli, 1990] suggest using a smaller value, i.e. 0.02 °C/m, for the Northern Adriatic basin. In equation (4.1) the surface temperature is conventionally assumed to be 15 °C [Chierici, 1989], so the injected aquifer is at an initial temperature of 30 °C. Above and below the aquifer confining beds the medium consists of of a sequence of alternating sandy and clayey units. The horizontal hydraulic conductivity of the injected formation and of the confinig units is set to 1×10^{-6} m/s and 10^{-10} m/s, respectively, i.e. the same as unit $A3$ and clay in Table 4.1. The vertical hydraulic conductivity is one tenth of the horizontal value. As to the thermal properties, heat conductivity and volumetric capacity are 0.6 W m^{-1} °C^{-1} and 4.18×10^{6} J m^{-3} °C^{-1},

respectively, for water and 5.0 W m^{-1} $°C^{-1}$ and 2.5×10^6 J m^{-3} $°C^{-1}$ for the formation. The relationship used in Comerlati *et al.* [2004] is selected as the constitutive law for the vertical rock compressibility c_M (Figure 4.6), with c_M in unloading/reloading conditions 3.5 times less than that in virgin loading conditions. Other significant parameters are the water compressibility $\beta_f = 9.0 \times 10^{-4}$ MPa^{-1} and thermal expansion coefficients $\beta'_f = 4.5 \times 10^{-4}$ $°C^{-1}$ [Wagner & Kretzschmar, 2008], respectively, and the formation thermal expansion coefficient $\beta'_s = 35 \times 10^{-6}$ $°C^{-1}$ [Fjaer *et al.*, 2008].

A set of simulations is performed by injecting seawater over a 60-m long inlet (Figure 4.15) with a constant overpressure of 1 MPa. All scenarios span a 10-year period, consisting of 3-year injection operations and a 7-year post-injection stage. Three test cases are addressed depending on the temperature θ_{inj} of the injected seawater (Figure 4.17), namely:

- **Test case 1**: θ_{inj} is constant and equal to 15 °C;
- **Test case 2**: θ_{inj} is constant and equal to 45 °C;
- **Test case 3**: θ_{inj} varies between a minimum of 7.5 °C and a maximum of 22.5 °C according to season [e.g., ARPA-FVG, 2007].

It is worth noting that the constant temperature in Test case 1 can be interpreted as the average of the periodic function describing the temperature profile in Test case 3.

The results of the simulation show that the impact of temperature on the pore-pressure change Δp distribution is quite small with respect to the isothermal case. Figure 4.18 provides the distribution of the Δp difference between Test case 1 and the isothermal case, and Test case 2 and the isothermal case, respectively, at the end of the injection period in a horizontal cross-section at z = -750. Only a slight delay/acceleration of the pressure field propagation can be observed when a colder/warmer injetion temperature occurs, with the largest difference located close to the well on the order of 0.6×10^{-1} MPa. No appreciable difference on Δp is found between Test case 1 and Test case 3. The Δp distributions can thus be practically considered the same in all cases and equal to the isothermal Δp shown in Figures 4.19 and 4.20 at different time steps during injection and post-injection, respectively. It is worth noting that, following cessation of pumping, the overpressure is quickly dissipated, decreasesing by more than 90% in one year.

The elemental temperature change $\Delta\theta$ distribution at several time steps is shown in Figure 4.21 in a radial section through the well for Test case 1. Similar results hold true for Test cases 2 and 3 in terms of affected volume, with a +15 °C and -22.5 °C

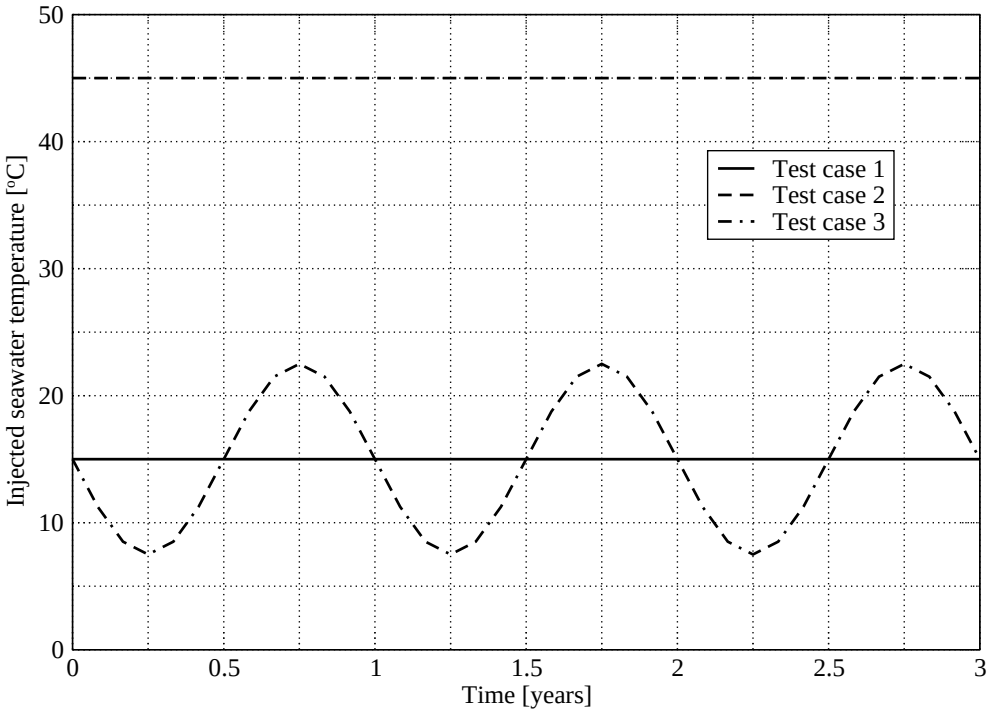

Figure 4.17: Injection temperature profile vs. time in the three simulated test cases.

peak $\Delta\theta$ value, respectively. In all cases, the region subject to a change in temperature keeps expanding for 3 years mainly into the aquifer up to a distance of about 125 m from the well, with some diffusive heat transfer into the sealing layers, too. Once injection is stopped, the convective contribution diminishes because of tha small velocity values , with the heat transfer essentially governed by the thermal diffusivity of the saturated formation. After 10 years the process has not reached a steady state, meaning that the aquifer has a small thermal diffusivity and a longer time is required to attain a new equilibrium condition. The ground surface responses in terms of vertical displacements Δz in Test cases 1 and 2, respectively, are compared to the isothermal model and shown in Figures 4.22 and 4.23, along a radial section through the well, and in Figure 4.24, in which the behaviour in time at the well location is plotted. The largest Δz predicted at end of the injection in isothermal conditions is equal to 1.97×10^{-2} m. The largest deviation due to the thermal deformation is 0.15×10^{-2} m, i.e. about 8%, negative in Test case 1 and positive in Test case 2, respectively. At the end of the injection, the uplift is quickly recovered with no significant residual deformation related to the still non-equilibrated temperature distribution, namely less than 1×10^{-3} m (Figure 4.24). Consistent with the similitude in the pressure and temperature fields, Test case 3 exhibits almost the same

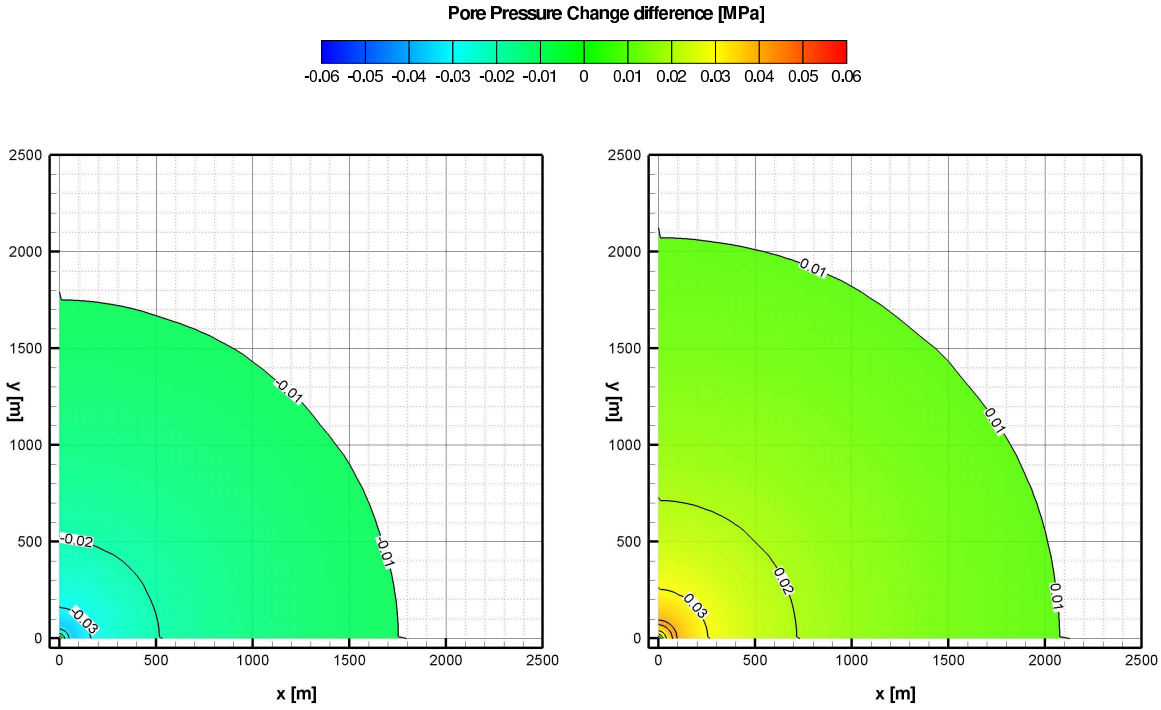

Figure 4.18: Contour plot of the Δp difference [MPa] between Test case 1 (left) and Test case 2 (right) and the isothermal analysis, respectively, at the end of the injection (year 3) in a cross section at z = -750 m.

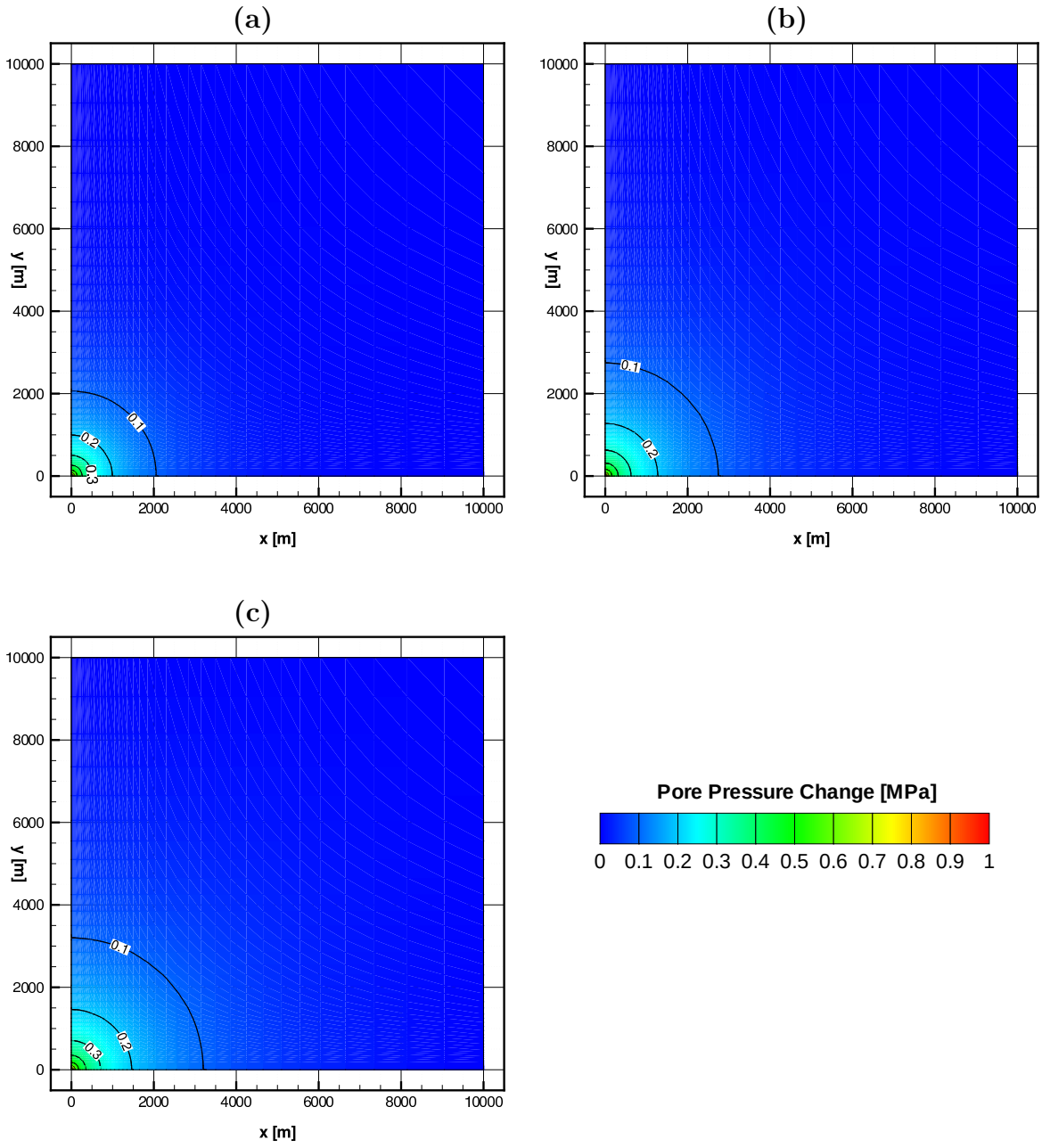

Figure 4.19: Isothermal case: contour plot of the pore-pressure change [MPa] along a horizontal cross-section at z = -750 m after 1-year (a), 2-year (b), and 3-year injection, respectively.

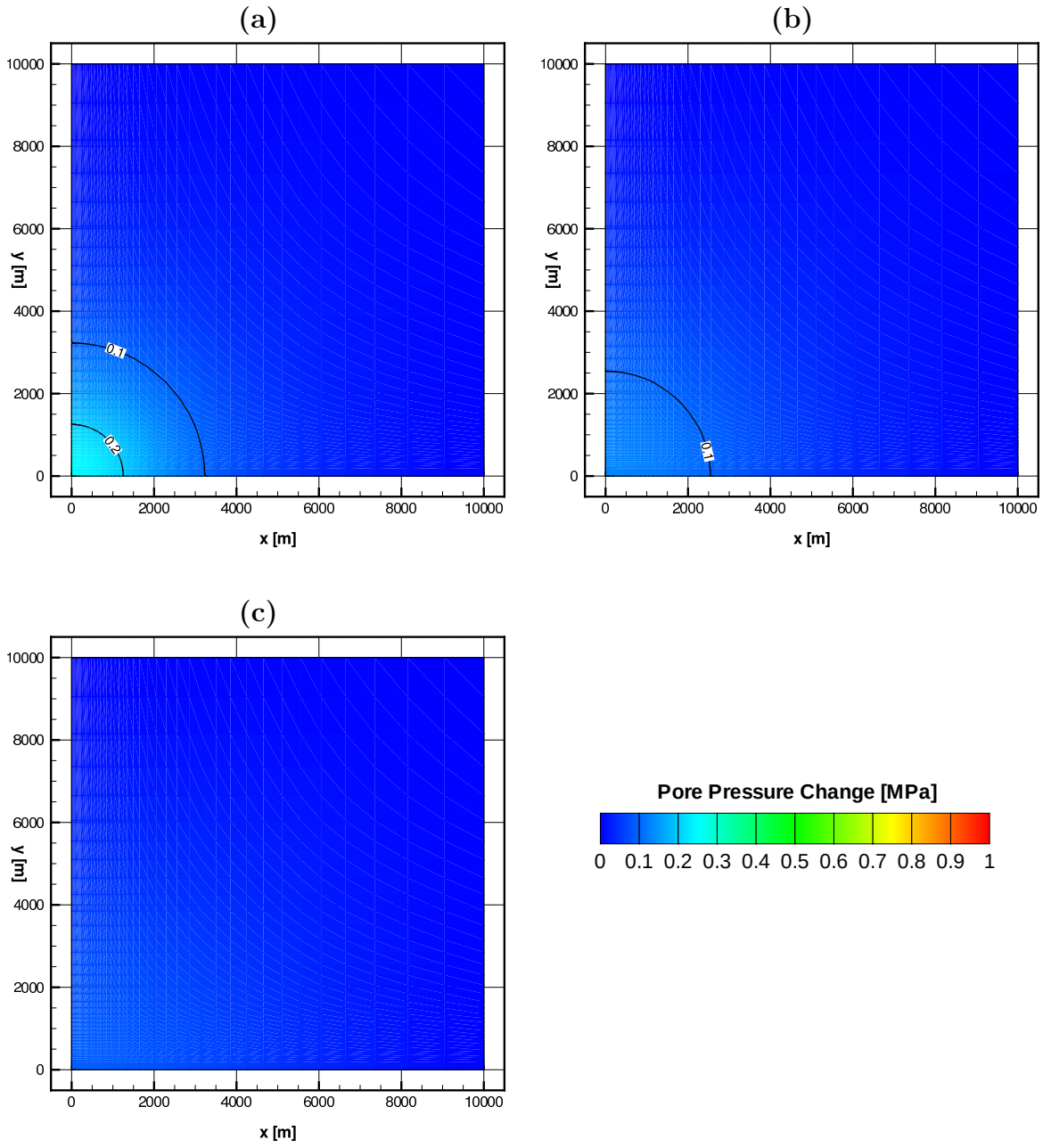

Figure 4.20: Isothermal case: contour plot of the pore-pressure change [MPa] along a horizontal cross-section at z = -750 m after 1 month (a), 6 months (b), and 1 year (c) injection is stopped, respectively.

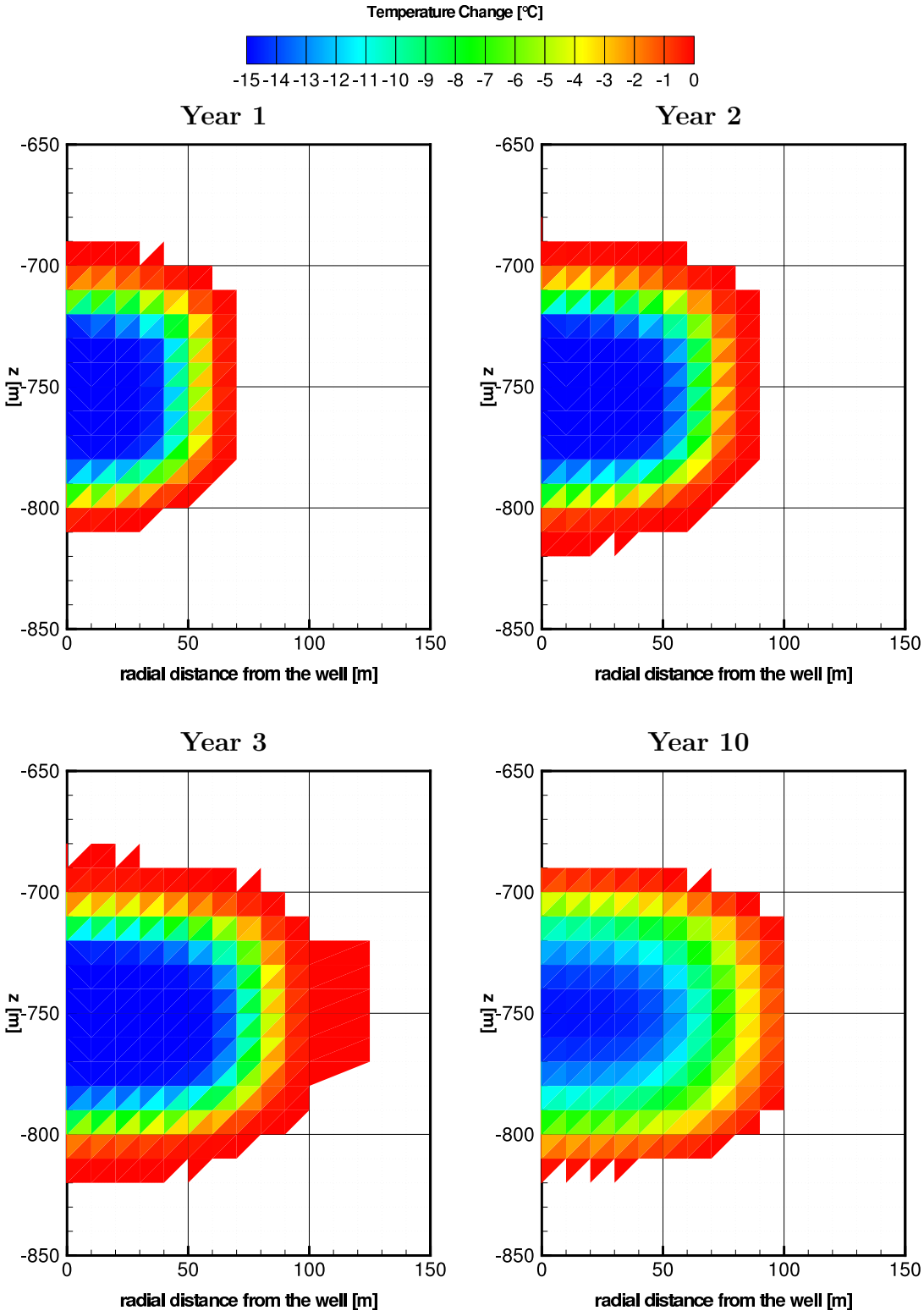

Figure 4.21: Test case 1: elemental temperature change distribution in a radial section through the well at several time steps.

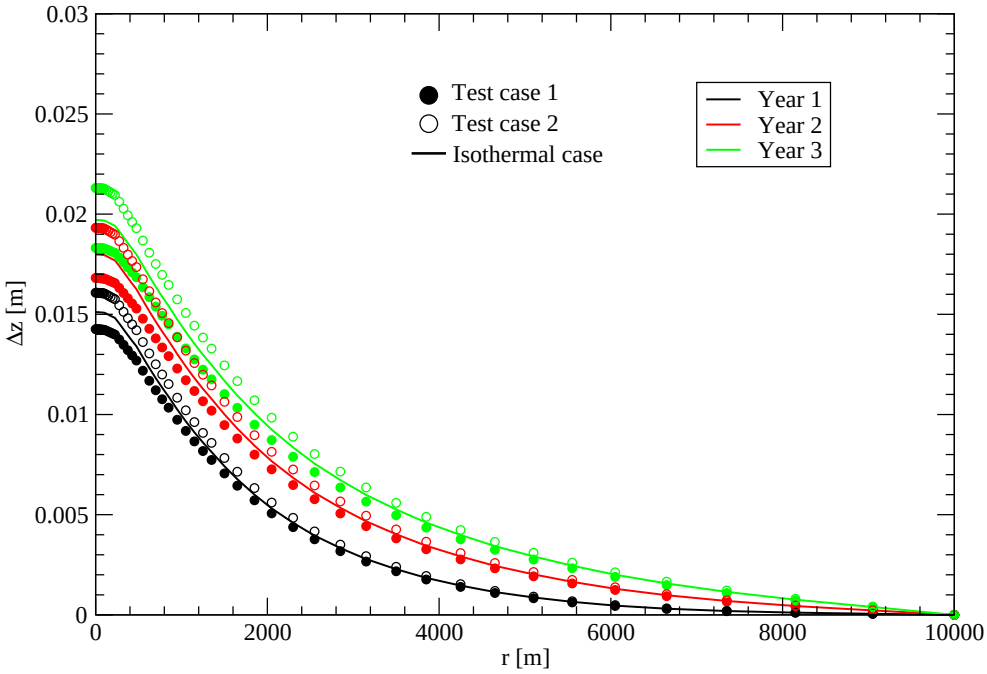

Figure 4.22: Land vertical displacement along a radial section through the well at three time steps during injection. The continuous profile is used for the isothermal case, while filled and empty circles identify Test cases 1 and 2, respectively.

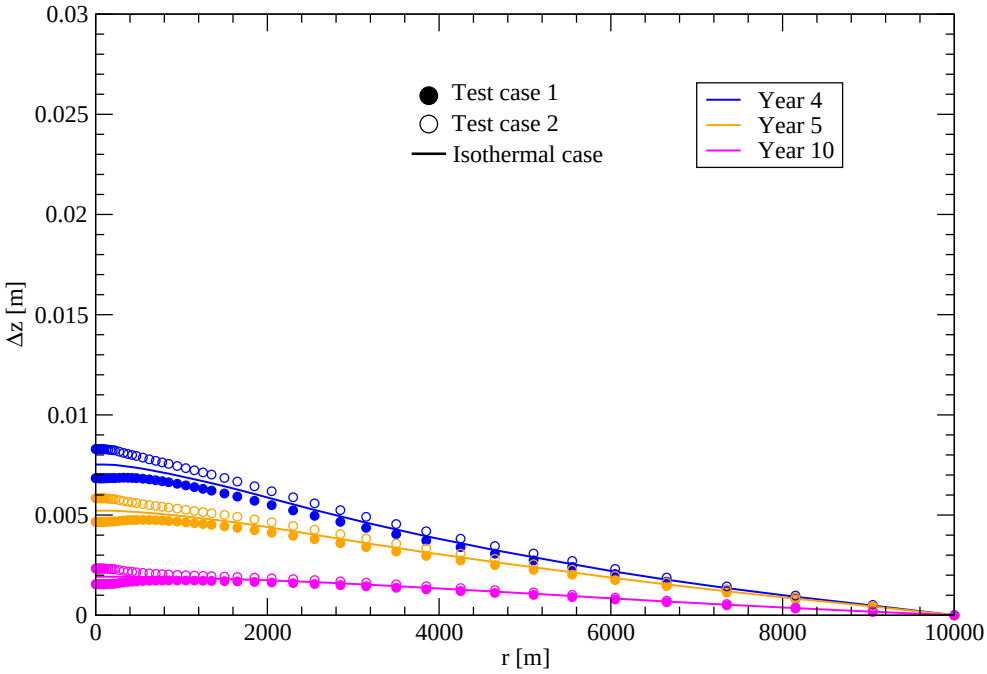

Figure 4.23: The same as Figure 4.22 during post-injection.

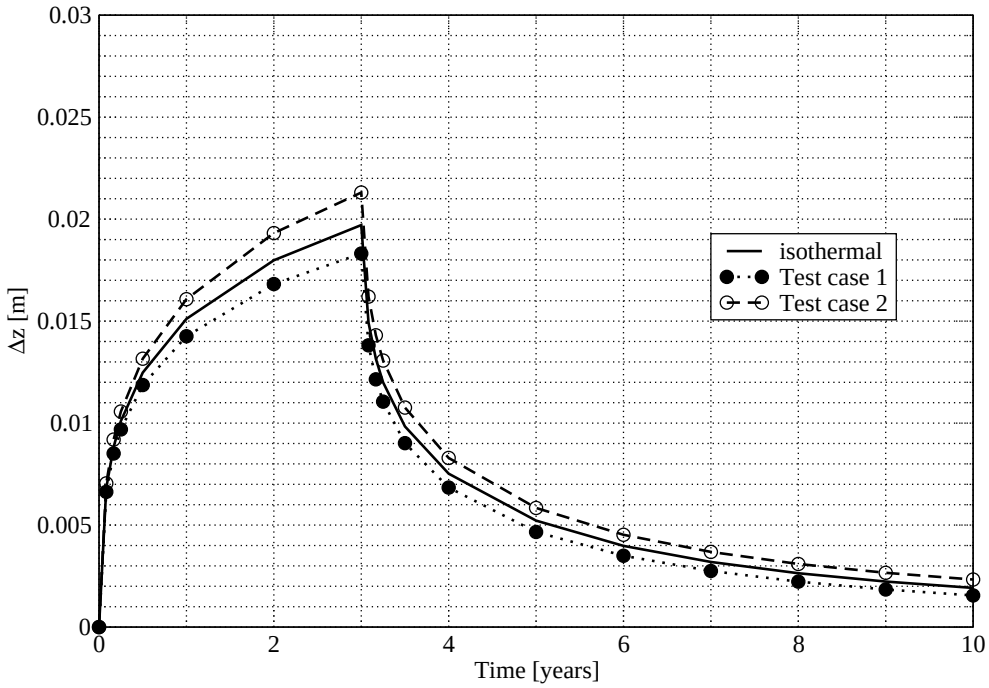

Figure 4.24: Land vertical displacement at the injection point vs time. As in Figure 4.22 the continuous profile is used for the isothermal case, while filled and empty circles identify Test cases 1 and 2, respectively.

displacements as Test case 1 (Figure 4.25), with only small differences related to the oscillatory temperature behaviour.

It may be concluded that in a quite realistic configuration the influence of the temperature on the pressure field appears to be very small relative to the isothermal case. By distinction, some influence is exerted by the thermal gradient on the predicted uplift, which can vary by up to about 8%. Anyway, for the temperature variations assumed herein the overpressure is still the predominant cause of deformation.

4.5 Conclusions

The numerical models presented in Chapter 2 and 3 have been experimented with in some engineering applications, using both realistic geomechanical, hydrological and geothermal data and vertical stratigraphic profiles representative of shallow and deep geological formations underneath the Venice lagoon, Italy.

Two consolidation examples performed with the aid of the 3-D Mixed FE model have confirmed the ability of the method in limiting the oscillations of the pore pressure solution in presence of significant hydraulic conductivity contrasts also in practical complex

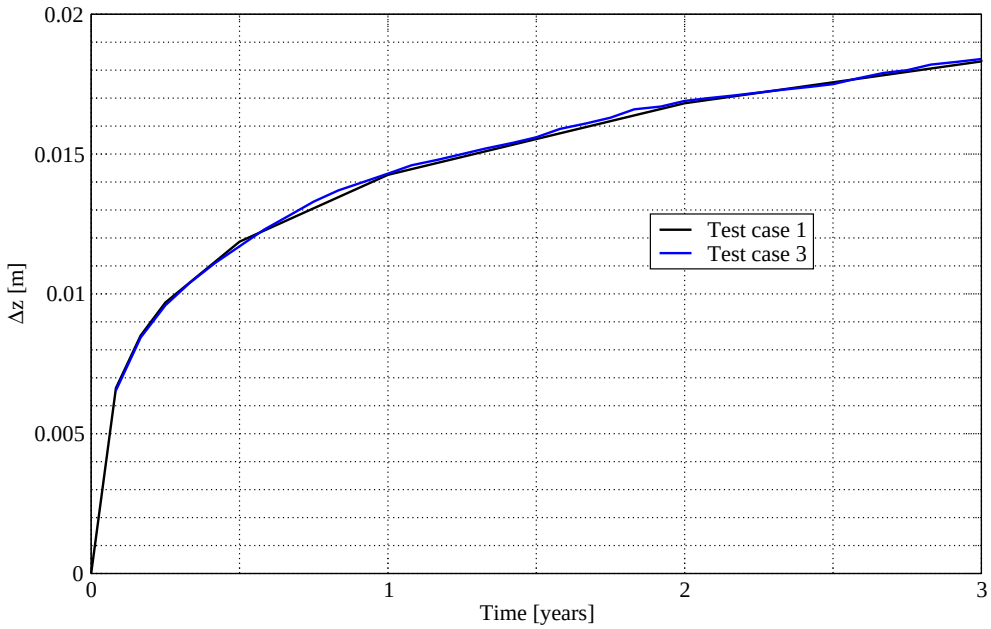

Figure 4.25: Comparison between the vertical displacement profile of Test cases 1 (in black) and 3 (in blue) during injection.

coupled processes. Afterwards, based on the GMMs formulation, a set of simulations addressing the seawater injection into a deep aquifer has excluded an important role of temperature gradient effects in the pilot project of anthropogenic uplift of Venice, recently advanced by Castelletto *et al.* [2008].

The following conclusive remarks can be made:

- in the trial embankment construction test, the small overpressure rise and dissipation in time are efficiently simulated, with no instability in the numerical solution observed;

- the example concerning the groundwater withdrawl from a shallow confined aquifer provides an accurate simulation of the increase in pore pressure in the sealing layers at the early stage of pumping, i.e. the Noordbergum effect, involved by the time-dependent aquifer volumetric contraction, with the overpressure eventually canceled by pore-pressure diffusion;

- in the injection experiments, the numerical results have shown that, relatively to the isothermal case, the temperature difference between formation water and seawater taken from the Adriatic sea negligibly impacts the pressure field, with a little influence on the predicted uplift which can vary by up to about 8%, for the temperature variations assumed;

- the results obtained by the proposed numerical models encourage further developments such as the coupling between the Mixed FE and GMMs models in order to address the coupled thermo-poro-elasticity equations through a sequential solution method, and the extension to inelastic deformations.

Bibliography

Agenzia Regionale per la Protezione dell'Ambiente del Friuli Venezia Giulia ARPA-FVG (2007). Bollettino delle acque marino-costiere del Friuli Venezia Giulia, **9**.

Aziz, K., A. Settari (1979). *Petroleum Reservoir Simulation*. Applied Science Publishers, London, UK.

Bai, M., and Y. Abousleiman (1997). Thermoporoelastic Coupling with Application to Consolidation. *Int. J. Numer. Anal. Meth. Geomech.*, **21**, 121–132.

Barth, T. J., and D. C. Jespersen (1989). The Design and Application of Upwind Schemes on Unstructured Meshes. *AIAA* paper 89-0366, 1–12.

Baù, D., M. Ferronato, G. Gambolati, and P. Teatini (2002). Basin-Scale Compressibility of the Northern Adriatic by the Radioactive Marker Technique. *Geotechnique*, **52**(8), 605–616.

Bear, J. (1988). *Dynamics of Fluids in Porous Media*. Environmental Science Series. American Elsevier Pub. Co., New York, 1972. Reprinted with corrections, Dover Pub., New York.

Bergamaschi, L., and S. Mantica (1996). Efficient Algebraic Solvers for Mixed Finite Element Models of Porous Media Flows. In A. A. Aldama *et al.*, eds., *Proceedings of 11th International Conference on Computational Methods in Water Resources*, pp. 481–488. Computational Mechanics and Elsevier Applied Sciences, Southampton, London (UK).

Bergamaschi, L., M. Ferronato, and G. Gambolati (2008). Mixed Constraint Preconditioners for the Iterative Solution to FE Coupled Consolidation Equations. *J. Comp. Phys.*, **227**, 9885–9897.

Bilak, R. A., L. Rothenburg, and M. B. Dusseault (1991). Use of Surface Displacements to Monitor EOR Projects. In *Proc. of 5th Int. UNITAR Conf. on Heavy Crude and Tar Sands*, pp. 267–277, Caracas (Venezuela).

Biot, M. A. (1941). General Theory of Three-Dimensional Consolidation. *J. Appl. Phys.*, **12**, 155–164.

Biot, M. A. (1956). General Solutions of the Equations of Elasticity and Consolidation for a Porous Material. *J. Appl. Mech.*, **22**, 91–96.

Brutsaert, W., and M. Y. Corapcioglu (1976). Pumping of Aquifer with Visco-Elastic Properties. *ASCE J. Hydraul.*, **102**(11), 1663–1675.

Burghignoli, A., M. Jamiolkowski, and C. Viggiani (2007). Geotechnics for the Preservation of Historic Cities and Monuments: Component of a Multidisciplinary Approach. In *Proceedings of the 14th European Conference on Soil Mechanics and Geotechnical Engineering: Geotechnical Engineering in Urban Environments*, vol. 1, 3–38, Rotterdam, Millpress.

Carbognin, L., P. Teatini, and L. Tosi (2005). Land Subsidence in the Venetian Area: Known and Recent Aspects. *Giornale di Geologia Applicata*, **1**, 5-11, 2005.

Castelletto, N., M. Ferronato, G. Gambolati, M. Putti, and P. Teatini (2008). Can Venice be Raised by Pumping Water Underground? A Pilot Project to Help Decide. *Water Resour. Res.*, **44**, W01408, doi:10.1029/2007WR006177.

Chierici, G. L. (1989). *Principi di Ingegneria dei Giacimenti Petroliferi* (in Italian). Agip S.p.A., Milan.

Collins, P. M. (2005). Geomechanical Effects on the SAGD Process. SPE/PS-CIM/CHOA, paper 97905, 11 pp.. In *Int. Thermal Operations and Heavy Oil Symp.*

Comerlati, A., M. Ferronato, G. Gambolati, M. Putti, and P. Teatini (2003). Can CO_2 Help Save Venice from the Sea? *EOS, Trans. AGU*, **84**(49), 546–553.

Comerlati, A., M. Ferronato, G. Gambolati, M. Putti, and P. Teatini (2004). Saving Venice by Sea Water. *J. Geophys. Res.*, **109**, F03006, doi:10.1029/2004JF000119.

Comerlati, A., M. Ferronato, G. Gambolati, M. Putti, and P. Teatini (2005). A Coupled Model of Anthropogenic Venice Uplift. In Y. N. Abousleiman, A.-D. Cheng, and F.-J. Ulm, editors, *3rd Biot Conference on Poromechanics*, pp. 317–321. A. A. Balkema, London.

Comerlati, A., M. Ferronato, G. Gambolati, M. Putti, and P. Teatini (2006). Fluid-Dynamic and Geomechanical Effetcs of CO2 Sequestration below the Venice Lagoon. *Environ. & Eng. Geoscience*, **12**(3), 211–226.

Consorzio per la Gestione del Centro di Coordinamento delle Attività di Ricerca Inerenti il Sistema Lagunare Veneziano CORILA (1999). *Scenarios of Sea Level Rise for the Venice Lagoon*. Vol. 1. 40 pp.

Coussy, O. (1995). *Mechanics of Porous Continua*. J. Wiley & Sons, New York (NY).

Coussy, O. (2004). *Poromechanics*. J. Wiley & Sons, West Sussex, England, 2004.

Darcy, H., (1956). *Le Fontaines Publique de la Vile Dijon*. Victor Dalmont, Paris, France.

Davari, S. (2007). *Surface Heave in Thermal Processes*. Ph.D. thesis, Dept. of Chemical and Petroleum Engineering, The University of Calgary, Canada.

Dawson, C. N. (1990). Godunov Mixed Methods for Immiscible Displacement. *Int. J. Numer. Meth. Fluid.*, **11**, 835–847.

Dawson, C. N. (1991). Godunov-Mixed Methods for Advective Flow Problems in one Space Dimension. *SIAM Journal on Numerical Analysis*, **28**, 1282–1309.

Dawson, C. N. (1993). Godunov-Mixed Methods for Advection-Diffusion Equations in Multidimensions. *SIAM Journal on Numerical Analysis*, **30**, 1315–1332.

Detournay, E., and A. H. Cheng (1993). Fundamentals of Poroelasticity. In C. Fairhurst, editor, *Comprehensive Rock Engineering: Principles, Practice & Projects, Vol. II, Analysis and Design Method*, chapter 5, pp. 113–170. Pergamon Press.

Diersch, H.-J. G., and O. Kolditz (1998). Coupled Groundwater Flow and Transport: 2. Thermohaline and 3D Convection Systems. *Adv. Water Resources*, **21**, 401–425.

Dixon, T. H., F. Amelung, A. Ferretti, F. Novali, F. Rocca, R. Dokka, G. Sella, S.-W. Kim, S. Wdowinski, and D. Whitman (2006). Subsidence and Flooding in New Orleans. *Nature*, **441**, 587–588.

Doornhof, D. (1992). Surface Subsidence in The Netherlands: the Groningen Gas Field. *Geologie en Mijnbouw*, **71**, 119–130.

Durlofsky, L. J., B. Engquist, and S. Osher (1992). Triangle Based Adaptive Stencils for the Solution of Hyperbolic Conservation Laws. *J. Comp. Phys.*, **98**, 64–73.

Dusseault, M. B., and L. Rothenburg (2002). Analysis of Deformation Measurements for Reservoir Management. *Oil & Gas Science and Technology - Rev. IFP*, **57**(5), 539–554.

D'Haese, C. M. F., M. Putti, C. Paniconi, and N. E. C. Verhoest (2007). Assessment of Adaptive and Heuristic Time Stepping for Variably Saturated Flow. *Int. J. Numer. Meth. Fluid.*, **53**(7), 1173–1193.

de Marsily, G. (1986). *Quantitative Hydrogeology: Groundwater Hydrology for Engineers*. Academic Press.

De Smedt, F. (2007). Two- and Three-Dimensional Flow of Groundwater. In *The Handbook of Groundwater Engineering*, Jacques Delleur (ed.), 4.1–4.36., CRC Press.

Elder, J. W (1967a). Steady Free Convection in a Porous Medium Heated from Below. *J. Fluid Mech.*, **27**, 29–48.

Elder, J. W (1967b). Transient Convection in a Porous Medium. *J. Fluid Mech.*, **27**, 609–623.

Fernandez, R. T. (1972). *Natural Convection from Cylinders Buried in Porous Media*. Ph.D. dissertation, Univ. of Calif., Berkeley.

Ferronato, M., G. Gambolati, and P. Teatini (2001). Ill-Conditioning of Finite Element Poroelasticity Equations. *Int. J. Solids Struct.*, **38**, 5995–6014.

Ferronato, M., G. Gambolati, and P. Teatini (2003a). Unloading-Reloading Uniaxial Compressibility of Deep Reservoirs by Marker Measurements. In S. Stiros and S. Pytharouli, editors, *Proc. of 11th Int. Symp. on Deformation Measurements*, pp. 341–346, Geodesy and Geodetic Applications Laboratory, Patras University.

Ferronato, M., G. Gambolati, P. Teatini, and D. Baù (2003b). Interpretation of Radioactive Marker Measurements to Evaluate Compaction in the Northern Adriatic Gas Fields. *SPE Reservoir Evaluation Engeneering*, **6**(6), 401–411.

Ferronato, M., G. Gambolati, P. Teatini, and D. Baù (2004). Radioactive Marker Measurements in Heterogeneous Reservoirs: Numerical Study. *Int. J. Geomech.*, **4**, 79–92.

Ferronato, M., C. Janna, G. Gambolati, and P. Teatini (2008). Numerical Modelling of Regional Faults in Land Subsidence Prediction Above Gas/Oil Reservoirs. *Int. J. Numer. Anal. Meth. Geomech.*, **32**, 633-657.

Ferronato, M., G. Pini, and G. Gambolati (2009). The Role of Preconditioning in the Solution to FE Coupled Consolidation Equations by Krylov Subspace Methods. *Int. J. Numer. Anal. Meth. Geomech.*, **33**, 405–423.

Ferronato, M., L. Bergamaschi, and G. Gambolati (2009). Performance and Robustness of Block Constraint Preconditioners in Finite Element Coupled Consolidation Models. *Int. J. Numer. Meth. Eng.*, doi: 10.1002/nme.2702. To appear.

Fjaer, E., R.M. Holt, P. Horsrud, A.M. Raaen, and R. Risnes (2008). *Petroleum Related Rock Mechanics*. Elsevier, Amsterdam and Oxford, 2^{nd} edition.

Freund, R. W., and N. M. Nachtingal (1994). A New Krylov-Subspace Method for Symmetric Indefinite Linear Systems. In *Proceedings of the 14th IMACS World Congress on Computational and Applied Mathematics*, 1253–1256.

Gambolati, G. (1973). Equation for One-Dimensional Vertical Flow of Groundwater, 1, The Rigorous Theory. *Water Resour. Res.*, **9**(4), 1022–1028.

Gambolati, G., P. Gatto, and R. A. Freeze (1994). Mathematical Simulation of the Subsidence of Venice: 2. Results. *Water Resour. Res.*, **10**, 563–577.

Gambolati, G., G. Ricceri, W. Bertoni, G. Brighenti, and E. Vuillermin (1991). Mathematical Simulation of the Subsidence of Ravenna. *Water Resour. Res.*, **27**, 2899–2918.

Gambolati, G. (1992). Comment on "Coupling Versus Uncoupling in Soil Consolidation". *Int. J. for Numer. and Analytic. Methods in Geomech.*, **16**, 833–837.

Gambolati, G., P. Teatini, D. Baú, and M. Ferronato (2000). The Importance of Poro-Elastic Coupling in Dynamically Active Aquifers of the Po River Basin, Italy. *Water Resour. Res.*, **36**(9), 2443–2459.

Gatto, P., and G. Mozzi (1971). Relazione sul pozzo Venezia 1-CNR: Esame delle carote Tech. Rep. 20, Laboratorio per la Dinamica delle Grandi Masse-CNR, 23 pp., Venice. (in Italian).

Geertsma, J. (1966). Problems of Rock Mechanics in Petroleum Production Engineering. In *Proc. 1st Cong. Int. Soc. of Rock Mechanics*, Lisbon, 585–594.

Godunov, S. K. (1959). A Difference Method for the Numerical Calculation of Discontinuous Solutions of Hydrodynamic Equations. *Mathematics of the USSR-SBORNIK*, **47**, 271–306.

Heywood, C. (1995). Investigation of Aquifer-System Compaction in the Hueco Basin, El Paso, Texas, USA. In F. B. J. Barends, F. J. J. Brouwer, and F. H. Schroeder, editors, *Land Subsidence (Proceedings of the V International Symposium on Land Subsidence, The Hague, October 1995)*, pp. 35–45, Wallingford, UK. IAHS Publ. No.234.

Hoffman, J.,H. A. Zebker, D. L. Galloway, and F. Amelung (2001). Seasonal Subsidence and Rebound in Las Vegas Valley, Nevada, Observed by Synthetic Aperture Radar Interferometry. *Water Resour. Res.*, **37**(6), 1551–1566.

Holtz, R. D. (1991). Stress Distribution and Settlement of Shallow Foundations. In H.-Y. Fang, editor, *Foundation Engineering Handbook*, chapter 5, pp. 166–216, van Nostrand Reinhold, New York.

Hudson, J., O. Stephansson, J. Andersson, C. F. Tsang, and L. Ling (2001). Coupled T-H-M Issues Related to Radioactive Waste Repository Design and Performance. *Int. J. Rock Mech. Mining Sci.*, **38**, 143–161.

Idelson, S. R., J. C. Heinrich, and E. Onate (1996). Petrov-Galerkin Methods for the Transient Advective-Diffusive Equation with Sharp Gradients. *Int. J. Numer. Meth. Eng.*, **39**, 1455–1473.

Jha, B., and R. Juanes (2007). A Locally Conservative Finite Element Framework for the Simulation of Coupled Flow and Reservoir Geomechanics. *Acta Geotechnica*, **2**, 139–153.

Ketelaar, G., F. van Leijen, P. Marinkovic, and R. Hassen (2007). Multi-Track PS-InSAR Data Fusion. In *ENVISAT 2007 (Proc. ENVISAT Symposium, Montreux, Switzerland, 23-27 April 2007)*. CD-ROM.

King, F. H. (1892). Fluctations in the Level and Rate of Movement of Ground-Water on the Wisconsin Agricultural Experiment Station Farm at Whitewater, Wisconsin. *US Dept. of Agriculture Weather Bureau Bulletin*, **5**, 75 pp.

Kipp, K. L., Jr. (1997). Guide to the Revised Heat and Solute Transport Simulator: HST3D – Version 2 U.S. Geological Survey, Water-Resources Investigations Report 97-4157.

Kosloff, D., R. F. Scott, and J. Scranton (1980). Finite Element Simulation of Wilmington Oil Field Subsidence: II. Nonlinear Modelling. *Tectonophsysics*, **70**, 159–183.

Kurashige, M. (1989). A Thermoelastic Theory of Fluid-Filled Porous Materials. *Int. J. Solids Struct.*, **25**(9), 1039–1052.

Lewis, R. W., and B. A. Schrefler (1998). *The Finite Element Method in the Deformation and Consolidation of Porous Media*. J. Wiley, New York, 2^{nd} edition.

Liu, X.D. (1993). A maximum Principle Satisfying Modification of Triangle Based Adaptive Stencils for the Solution of Scalar Hyperbolic Conservation-Laws. *Siam Journal on Numerical Analysis*, **30**, 701–716.

Martin, J. C., and S. Serdengecti (1984). Subsidence Over oil and Gas Fields. In T. Holzer, editor, *Man-Induced Land Subsidence, Rev. Eng. Geol.*, volume 6, pages 23–34, Boulder(CO). Geol. Soc. of Am.

Mattavelli, L., and Novelli, L. (1990). Geochemistry and Habitat of the Oils in Italy. *Am. Assoc. Petr. Geol. B.*,**74**, 1623–1639.

Mazzia, A., L. Bergamaschi, and M. Putti (2000). A Time-Splitting Technique for Advection-Dispersion Equation in Groundwater. *J. Comp. Phys.*, **157**(1), 181–198.

Mazzia, A., and M. Putti (2005). High order Godunov Mixed Methods on Tetrahedral Meshes for Density Driven Flow Simulations in Porous Media. *J. Comp. Phys.*, **208**(1), 154–174.

McTigue, D. F. (1986). Thermoelastic Response of Fluid-Saturated Porous Rock. *J. Geophys. Res.*, **91**(B9), 9533–9542.

Means, W. D. (1976). *Stress and Strain: Basic Concepts of Continuum Mechanics for Geologists*. Springer-Verlag, New York.

Mercer, J. W., and G. F Pinder (1974). Finite Element Analysis of Hydrothermal Systems. *Finite Element Methods in Flow Problems*, University of Alabama Press.

Mobach, E., H. J. and Gussinklo (1994). In-Situ Reservoir Compaction Monitoring in the Gröningen Field. In *EUROCK'94, Rock Mechanics for Petroleum Engineering*, pp. 535–547, A. A. Balkema, Rotterdam.

Murad, M. A., and A. F. D. Loula (1992). Improved Accuracy in Finite Element Analysis of Biot's Consolidation Problem. *Comput. Meth. Appl. Mech. Eng.*, **95**, 359–382.

Murad, M. A., and A. F. D. Loula (1994). On the Stability and Convergence of Finite Element Approximations of Biot's Consolidation Problem. *Int. J. Numer. Meth. Eng.*, **37**, 645–667.

Necati Özisik, M. (1994). *Finite Difference Methods in Heat Transfer*. CRC Press.

Nguyen, T. S., and A. P. S. Selvadurai (1995). Coupled Thermal-Mechanical-Hydrological Behaviour of Sparsely Fractured Rock: Implications for Nuclear Fuel Waste Disposal. *Int. J. Rock Mech. Sci. & Geomech. Abstr.*, **32**(5), 465–479.

Nutting, P. G. (1930). Physical Analysis of Oil Sands. *Bull. Am. Ass. petrol. Geol.* **14**, 1337–1349.

Pao, W. K. S., R. W. Lewis, and I. Masters (2001). A fully Coupled Hydro-Thermo-Poro-Mechanical Model for Black Oil Reservoir Simulation. *Int. J. Numer. Anal. Meth. Geomech.*, **25**, 1229–1256.

Phillips, P. J., and M. F. Wheeler (2007a). A Coupling of Mixed and Continuous Galerkin Finite Element Methods for Poroelasticity I: the Continuous-In-Time Case. *Comp. Geosci.*, **11**, 131–144.

Phillips, P. J., and M. F. Wheeler (2007b). A Coupling of Mixed and Continuous Galerkin Finite Element Methods for Poroelasticity II: the Discret-in-Time Case. *Comp. Geosci.*, **11**, 145–158.

Phillips, P. J., and M. F. Wheeler (2008). A Coupling of Mixed and Discontinuous Galerkin Finite-Element Methods for Poroelasticity. *Comp. Geosci.*, **12**, 417–435.

Poland, J. F., and G. H. Davis (1969). Land Subsidence Due to Withdrawal of Fluids. In D. J. Varnes and G. A. Kiersch, editors, *Reviews in Engineering Society*, volume 2, pp. 187–269, Geological Society of America (GSA), Boulder, CO.

Quarteroni, A., and A. Valli (1994). *Numerical Approximation of Partial Differential Equations*, volume 23 of *Springer Series in Computational Mathematics*. Springer-Verlag, Berlin, 1994.

Raviart, P. A., and J. M. Thomas (1977). A Mixed Finite Element Method for Second Order Elliptic Problems. In I. Galligani and E. Magenes, editors, *Mathematical Aspects of the Finite Elements Method*, number 606 in Lecture Notes in Mathematics, New York. Springer-Verlag.

Reed, M. B. (1984). An Investigation of Numerical Errors in the Analysis of Consolidation by Finite Elements. *Int. J. Numer. Anal. Meth. Geomech.*, **8**, 243–257.

Reynolds, O. (1886). Experiments Showing Dilatancy, a Property of Granular Material, Possibly Connected with Gravitation. *Proc. R. Inst. of G. B.*, **11**, 354–363.

Rice, J. R., and M. P. Cleary (1976). Some Basic Stress Diffusion Solutions for Fluid-Saturated Elastic Porous Media with Compressible Constituents. *Rev. Geophys.*, **14**(2), 227–241.

Richtmyer, R. D., and K. W. Morton (1967). *Difference Methods for Initial-Value Problems*. Interscience Publishers, New York, 2^{nd} edition.

Rintoul, W. (1981). *Drilling Ahead: Tapping California's Richest Oil Fields*, chapter 6: The Case of the Disappearing Land, pp. 116–137, Valley Publishers, Santa Cruz (CA).

Rivera, A., E. Ledoux, and G. de Marsily (1991). Nonlinear Modeling of Groundwater Flow and Total Subsidence of the Mexico City Aquifer-Aquitard System. In A. I. Johnson, editor, *Land Subsidence (Proc. IV Int. Symposium on Land Subsidence)*, pages 44–58, IAHS Publ. no. 200.

Roberts, J. E., and J. M. Thomas (1991). Mixed and Hybrid Methods. In P. G. Ciarlet and J. L. Lions, eds., *Handbook of Numerical Analysis*, Vol. 2, 1991. North-Holland, Amsterdam.

Roose, T., P. Netti, L. Munn, Y. Boucher, and R. Jain (2003). Solid Stress Generated by Spheroid Growth Estimated Using a Linear Poroelastic Model. *Microvasc. Res.*, **66**, 204–212.

Sandhu, R. S., H. Liu, and K. J. Singh (1977). Numerical Performance of Some Finite Element Schemes for Analysis of Seepage in Porous Elastic Media. *Int. J. Numer. Anal. Meth. Geomech.*, **1**, 177–194.

Simonini, P., G. Ricceri, and S. Cola (2006). Geotechnical Characterization and Properties of the Venice Lagoon Heterogeneous Silts. In *Proceedings of the 2nd International Workshop: Characterisation and Engineering Properties of Natural Soils*, vol. 4, 2289–2328, London, Taylor & Francis.

Skempton, A. W. and D. H. McDonald (1956). Allowable Settlement of Buildings. In *Proc. Inst. Civil Eng., Part 3*, volume 5, pp. 727–768.

Stancliffe, R. P. W. S., and M. W. A. van der Kooij (2001). The Use of Satellite-Based Radar Interferometry to Monitor Production Activity at the Cold Lake Heavy Oil Field, Alberta, Canada. *Am. Assoc. Pet. Geol. Bull.*, **85**(5), 781–793.

Swan, C., R. Lakes, R. Brand, and K. Stewart (2003). Micromechanically Based Poroelastic Modeling of Fluid Flow in Haversian Bone. *J. Biomech. Eng.*, **125**, 25–37.

Tchonkova, M., J. Peters, and S. Sture (2008). A New Mixed Finite Element Method for Poro-Elasticity. *Int. J. Numer. Anal. Meth. Geomech.*, **32**, 579–606.

Teatini, P., D. Baù, and G. Gambolati (2000). Water-Gas Dynamics and Coastal Land Subsidence over Chioggia Mare Field, Northern Adriatic Sea. *Hydrogeol. J.*, **8**, 462–479.

Teatini, P., L. Tosi, T. Strozzi, L. Carbognin, U. Wegmuller, and F. Rizzetto (2005). Mapping Regional Land Displacements in the Venice Coastland by an Integrated Monitoring System. *Remote Sens. Environ.*, **98**(4), 403–413.

Teatini, P., M. Ferronato, G. Gambolati, and M. Gonella (2006). Groundwater Pumping and Land Subsidence in the Emilia-Romagna Coastland, Italy: Modeling the Past Occurrence and the Future Trend. *Water Resour. Res.*, **42**, doi:10.1029/2005WR004242.

Teatini, P., T. Strozzi, L. Tosi, U. Wegmüller, C. Werner, and L. Carbognin (2007). Assessing Short- and Long-Time Displacements in the Venice Coastland by Synthetic Aperture Radar Interferometric Point Target Analysis. *J. Geophys. Res.*, **112**, F01012, doi:10.1029/2006JF000656.

Terzaghi, K. (1925). *Erdbaumechanik auf Bodenphysikalischer Grundlage*. F. Deuticke, Wien.

Toh, K. C., and K. K. Phoon (2008). Comparison Between Iterative Solution of Symmetric and Non-Symmetric Forms of Biot's FEM Equations Using the Generalized Jacobi Preconditioner. *Int. J. Numer. Anal. Meth. Geomech.*, **32**, 1131–1146.

Toro, E.F. (1999). *Riemann Solvers and Numerical Methods for Fluid Dynamics*. Springer-Verlag, Berlin, 2^{nd} edition.

Tosi, L., L. Carbognin, P. Teatini, R. Rosselli, and G. Gasparetto Stori (2000). The ISES Project Subsidence Monitoring of the Catchment Basin South of the Venice Lagoon, Italy. In L. Carbognin, G. Gambolati, and A. I. Johnson, editors, *Land Subsidence (Proceedings of the VI International Symposium on Land Subsidence, Ravenna, Italy, September 2000)*, volume II, pp. 113–126. La Garangola, Padova, Italy.

USEPA (2002). Technical Program Overview: Underground Injection Control Regulation. Technical Report EPA 816-R-02-025, 81 pp., U.S. Environmental Protection Agency, Washington, D.C.

van der Knaap, W. (1959). Nonlinear Behavior of Elastic Porous Media. *Petroleum Transactions of the AIME*, **216**, 179–187.

van Leer, B. (1979). Towards the Ultimate Conservative Difference Scheme: A Second-Order Sequel to Godunov's Method. *Journal of Computational Physics*, **32**, 101–136.

Vermeer, P. A., and A. Verruijt (1981). An Accuracy Condition for Consolidation by Finite Elements. *Int. J. Numer. Anal. Meth. Geomech.*, **5**, 1–14.

Verruijt, A. (1969). Elastic Storage of Aquifers. In R. J. M. De Wiest, editor, *Flow Through Porous Media*, pages 331–376, New York, Academic Press.

Yanenko, N. N. (1971). *The Method of Fractional Steps: Solution of Problems of Mathematical Physics in Several Variables*. Springer.

Yin, S., M. B. Dusseault, and L. Rothenburg (2009). Thermal Reservoir Modeling in Petroleum Geomechanics. *Int. J. Numer. Anal. Meth. Geomech.*, **33**, 449–485.

Wagner, W., and H.-J. Kretzschmar (2008). *International Steam Tables - Properties of Water and Steam Based on the Industrial Formulation IAPWS-IF97*. Springer-Verlag, Berlin, 2^{nd} edition.

Wang, H. F. (2001). *Theory of Linear Poroelasticity*. Princeton University Press, Princeton, New Jersey, 2001.

Wang, G., and P. R. Kry (1997). Surface Heave Due to Fluid and Steam Injection. In *48th Annual Technical Meeting of the Petroleum Society of CIM*, number 97-10, 5 pp., Calgary, Canada.

Wang, S. J., and K. C. Hsu (2009). The Application of the First-Order Second-Moment Method to Analyze Poroelastic Problems in Heterogeneous Porous Media. *J. Hydrol.*, **369**, 209–221.

Wang, Y., and E. Papamichos (1994). Conductive Heat Flow and Thermally Induced Fluid Flow Around a Well Bore in a Poroelastic Medium. *Water Resour. Res.*, **30**(12), 3375–3384.

Wheeler, M. F., and X. Gai (2007). Iteratively Coupled Mixed and Galerkin Finite Element Methods for Poro-Elasticity. *Numer. Meth. Part. D. E.*, **23**, 785–797.

Wright, T. J., B. E. Parsons, and Z. Lu (2004). Towards Mapping Surface Deformation in Three Dimensions Using InSAR. *Geophys. Res. Lett.*, **31**(1), L01607, doi:10.1029/2003GL018827.

Zienkiewicz O. C., A. H. C. Chan, M. Pastor, B. A. Schrefler, and T. Shiomi (1999). *Computational Geomechanics with Special Reference to Earthquake Engineering*. John Wiley & Sons, Chichester.

Ringraziamenti

In queste poche righe, voglio esprimere la mia gratitudine a tutte le persone che mi hanno aiutato a portare a compimento il percorso di dottorato di ricerca.
Ringrazio di cuore il Prof. Giuseppe Gambolati per avere avuto fiducia in me e per il sostegno che mi ha sempre dimostrato, l'Ing. Massimiliano Ferronato per avermi guidato da vicino e dato preziosi consigli in tutti questi anni passati a lavorare insieme, tutto il gruppo di Analisi Numerica del Dipartimento di Metodi e Modelli Matematici per le Scienze Applicate dell'Università di Padova, in particolare l'Ing. Carlo Janna, il Sig. Andrea Pellizzon, il Prof. Mario Putti, l'Ing. Pietro Teatini e l'Ing. Francesca Zanello, e il Prof. Ruben Juanes per avermi accolto presso il suo Department of Civil and Environmental Engineering del Massachusetts Institute of Technology e tutti i suoi collaboratori. Un pensiero va a tutte le persone con cui ho vissuto gli anni del dottorato.
Un grazie particolare va al mio amico Michele Zantedeschi. Ad Alessandra un ringraziamento speciale. Infine, il ringraziamento più importante va ai miei genitori, ai miei nonni e a mia sorella Claudia, per tutto. A loro dedico questo lavoro.